eman ta zabal zazu
Universidad del País Vasco
Euskal Herriko Unibertsitatea

BCMATERIALS
BASQUE CENTER FOR MATERIALS, APPLICATIONS & NANOSTRUCTURES

Patterned magnetic nanostructures for biomedical applications

Beatriz Mora Cuadrado

PhD Thesis

Supervisors:

Dr. Rafael Morales Arboleya

Dra. Carolina Redondo Esteban

2018

Agradecimientos

En primer lugar me gustaría dar las gracias a mis tutores por haber confiado en mí y dado la oportunidad de trabajar en un tema que me apasionó desde el principio, por haberme apoyado y aportado conocimiento en cada fase del proceso.

Muchas gracias Rafa por tu manera de afrontar las situaciones más complicadas con decisión, optimismo y buen humor. En especial por habernos animado siempre a salir de la zona de confort y dado la oportunidad de viajar y realizar estancias en el extranjero además de transmitirnos toda esa ilusión por participar en congresos internacionales.

Gracias Carol por todo el ánimo que me has dado cuando nos encontrábamos con algún bache en el camino, por tu confianza y seguridad en que todo iba a salir bien. Te agradezco todas esas largas horas de SEM y tu conversación y dinamismo para hacer el rato más llevadero.

También quería dar las gracias a los que fueron mis tutores durante las estancias en el extranjero, tanto a Ivan Schuller de la universidad de California, San Diego como a Hernán Pastoriza del centro atómico Bariloche por haberme acogido en sus respectivos grupos de investigación como una más, facilitándome todos los medios posibles y haciéndome partícipe de todas las actividades que se realizaron en el tiempo en que colaboré con ellos.

Particular agradecimiento a Lola Boyano por creer en nosotros y hacer posible la parte bio de la tesis. Gracias Arantza Pérez por todos los ensayos, tu tiempo y paciencia.

Quiero agradecerle a Iñaki todo lo que me ha enseñado de magnetismo y caracterización magnética. Gracias por tu tiempo y tu genialidad para encontrar la manera de hacer la medida deseada.

En especial quiero dar las gracias a mis compañeros Nastassia e Isaac por alegrarme los días en el despacho, por vuestra amistad fuera y dentro del laboratorio y por los bailes. Nastassia, gracias por acogerme tan bien cuando llegué a la universidad, por entrenarme en el laboratorio con paciencia y haciéndome sentir feliz y tranquila, sin miedo a equivocarme. Isaac, gracias por ser tan atento y saber escuchar cuando se necesita, pero sobre todo gracias por ser mi compi de baile de los miércoles aun cuando casi todo el mundo se descolgó de repente.

Edu y Pablo, gracias por hacerme sentir como en casa nuestro pequeño hogar bilbaíno. Gracias por las excursiones, las cenas multitudinarias e internacionales que tanto estrés nos generaban en la cocina. Gracias por los zuritos en el kasko y por nuestras noches de cena y serie en el salón, aunque Pablo siempre se quejara de que ocupaba todo el espacio del sofá. Gracias también a ti Sofi, que aunque por poco tiempo compartimos grandes momentos en el pisito.

También quiero dar las gracias a nuestros compañeros internacionales que vinieron de estancia a nuestro laboratorio. Koldo, Karole, Lizardi, Murilo, Peterson, Maria Eugenia, Gabriel, Claudio y Manuel, no os podéis hacer una idea de todo lo que nos habéis aportado. Gracias por vuestra amistad, risas y vivencias compartidas.

Para terminar quiero dar las gracias a mi grande y maravillosa familia. Gracias por creer en mí y por apoyarme en este y en todos los proyectos de mi vida. Y gracias a ti Carmen, por saber sacar lo mejor de mí en los mejores y peores momentos.

Resumen

Las nanopartículas magnéticas poseen propiedades excepcionales que han dado lugar a resultados muy prometedores en distintas áreas de la investigación biomédica, como son la entrega dirigida de fármacos, la hipertermia magnética o los agentes de contraste en imagen por resonancia magnética.

Las nanopartículas superparamagnéticas sintetizadas mediante procedimientos químicos han sido las más utilizadas para estos propósitos. Estas nanopartículas presentan remanencia nula, crucial para las aplicaciones biomédicas, ya que evitan la aglomeración de las mismas cuando están dispersas en un líquido. Sin embargo, uno de los mayores inconvenientes de estas nanopartículas, que son típicamente óxidos de hierro, es que presentan momentos magnéticos bajos, lo que disminuye enormemente su eficiencia. Se pueden conseguir momentos magnéticos más elevados incrementando el tamaño pero nanopartículas superparamagnéticas de mayor tamaño podrían superar el límite superparamagnético dando lugar a una remanencia no nula que podría traducirse en una agregación nada deseada de las nanopartículas.

En esta tesis se ha apostado por una estrategia alternativa para la fabricación de nanoestructuras dentro de la categoría de rutas de fabricación "top-down" que combina litografía y técnicas de deposición física de vapor, permitiendo la producción de nanoestructuras con momentos magnéticos por unidad de volumen más altos dada la posibilidad de depositar elementos magnéticos puros y aleaciones. Además, se pueden obtener nanoestructuras magnéticas con mayores dimensiones preservando la remanencia nula. Cabe notar que este tipo de rutas proporcionan una mayor versatilidad en el diseño de configuraciones magnéticas jugando con distintos tamaños y geometrías y gracias a la gran ventaja de depositar multicapas de distintos materiales. Otro factor de gran interés es que las técnicas de fabricación top-down dan lugar a

nanoestructuras planas con una fuerte anisotropía de forma, a diferencia de la mayoría de las nanopartículas magnéticas esféricas sintetizadas por procedimientos químicos. De esta manera, cuando se aplica un campo magnético alterno, las nanoestructuras rotan para alinear su momento magnético con la dirección del campo externo, dando lugar a un torque y consecuentemente a una fuerza magnética que puede utilizarse, como se ha demostrado en la literatura, para manipular mecánicamente la materia adyacente. En concreto, hay un interés creciente en la aplicación de estímulos mecánicos en las células biológicas. Es bien sabido que las células convierten ciertos estímulos mecánicos en señales bioquímicas mediante un mecanismo llamado mecanotransducción. El uso de nanoestructuras magnéticas podría proporcionar un avance significativo respecto a las utilizadas nanopartículas superparamagnéticas debido a su propiedad distintiva de anisotropía.

En este contexto, una de las principales motivaciones de esta tesis es el trabajo de Kim et al.[1] en el que investigaron el uso de discos magnéticos en estado vórtice de NiFe de 1 μm de diámetro fabricados mediante fotolitografía para la destrucción de células cancerígenas en ensayos in-vitro. Aunque este estudio tenía unas expectativas muy prometedoras para el traslado del tratamiento magnético dirigido a aplicaciones clínicas, había dos cuestiones esenciales que tenían que abordarse previamente: primero, la limitación del tamaño de elemento de la fotolitografía en el rango micrométrico, siendo crucial para las aplicaciones biomédicas la reducción de las dimensiones a la escala submicrométrica; segundo, la necesidad de desarrollar discos con una mayor biocompatiblidad eliminando la presencia de Níquel. Entre las técnicas litográficas para la obtención de nanoestructuras submicrométricas, la litografía de interferencia es una excelente candidata. Esta técnica permite realizar patrones sin el uso de máscaras permitiendo la nanofabricación a un coste significativamente más bajo. Además, es una técnica muy versátil ya que se pueden obtener patrones de diferentes tamaños –desde unos cientos de nm de diámetro- y geometrías –discos, elipses y líneas- simplemente cambiando el ángulo del haz láser incidente y la dosis de exposición.

En este escenario los objetivos de la tesis son los siguientes:

1. Diseño de una estrategia de fabricación económica basada en litografía de interferencia para producir nanoestructuras con altos momentos magnéticos aptas para aplicaciones biomédicas.
2. Fabricación de nanoestructuras magnéticas con configuraciones de espín particulares manteniendo la remanencia nula requerida en biomedicina: nanoestructuras en estado vórtice e imanes antiferromagnéticos de diferentes composiciones y tamaños.
3. Estudio del comportamiento dinámico de las nanoestructuas magnéticas en solución: respuesta a los campos magnéticos externos y procesos de relajación.
4. Ensayos de citotoxicidad para el estudio de la viabilidad de las nanoestructuras diseñadas en cultivos celulares.

A continuación se muestra cómo se han ido alcanzando cada uno de los objetivos en los distintos capítulos de la tesis.

Objetivo 1: Diseño de una estrategia de fabricación económica basada en litografía de interferencia para producir nanoestructuras con altos momentos magnéticos aptas para aplicaciones biomédicas.

Los métodos de fabricación top-down originalmente utilizados para la realización de patrones en microelectrónica se han convertido en una estrategia muy atractiva para la fabricación de nanoestructuras magnéticas debido a tres motivos principales: por un lado, la combinación de litografía con técnicas de deposición física de vapor han permitido la producción de nanoestructuras con un buen control de la forma y las dimensiones; por otro lado, se permite el crecimiento de materiales magnéticos puros y aleaciones haciendo posible el desarrollo de nanoestructuras con altos momentos magnéticos preservando la remanencia nula, como es el caso de los discos en estado vórtice; además, se pueden depositar capas no magnéticas para proteger a las nanoestructuras del poder oxidativo de las suspensiones acuosas. El capítulo 2 consiste en la descripción de los fundamentos teóricos y principios operacionales de las técnicas experimentales utilizadas en esta

tesis tanto para fabricación como para caracterización de las nanoestructuras magnéticas, con especial énfasis en la descripción del sistema de litografía por interferencia (LI). Esta técnica de fabricación permite realizar patrones en áreas grandes (cm^2), dando lugar a una alta producción de nanoestructuras para ensayos biomédicos. La configuración del equipo hace posible seleccionar la forma y tamaño de los nanoelementos, desde 50 nm hasta algunas micras permitiendo el diseño de nanosestructuras con propiedades magnéticas específicas.

En el capítulos 3, se presentan dos rutas alternativas para la fabricación de nanoestructuras magnéticas en suspensión aprovechando que se pueden utilizar tanto resinas positivas como negativas en nuestro sistema LI, lo que permite fabricar plantillas de dots y antidots de resina. Un paso crucial después de depositar las capas magnéticas y eliminar la resina en un proceso de "lift-off, es el de la liberación de las nanoestructuras del sustrato, para el cual cada ruta plantea una solución distinta. Este proceso basado en un ataque químico puede modificar o incluso dañar las propiedades magnéticas de los nanoelementos, el cual fue optimizado mediante el uso de dos capas de sacrificio diferentes: Ge y Al. A lo largo del capítulo se discutieron las ventajas y desventajas de las rutas de fabricación propuestas.

Objetivo 2: Fabricación de nanoestructuras magnéticas con configuraciones de espín particulares manteniendo la remanencia nula requerida en biomedicina: nanoestructuras en estado vórtice e imanes antiferromagnéticos de diferentes composiciones y tamaños.

El segundo objetivo fue abordado a lo largo de los capítulos 4 y 5, en los cuales se llevó a cabo un estudio completo de las propiedades magnéticas de tres tipos distintos de nanoestructuras con forma de disco: nanoestructuras de Permalloy en estado vórtice en el capítulo 4, nanoestructuras en estado vórtice de Fe e imanes sintéticos aniferromagnéticos en el capítulo 5.

El capítulo 4 se centra en la caracterización de discos de Permalloy (NiFe) en estado vórtice fabricados mediante LI mediante las rutas de fabricación

descritas en el capítulo 3. Las nanoestructuras con forma de disco en estado vórtice se caracterizan por un flujo cerrado de espines en el plano del disco dando lugar a una magnetización nula en ausencia de campo magnético externo. Estos discos son interesantes para aplicaciones biomédicas ya que presentan remanencia nula (requerida para evitar la agregación de los mismos) y rotan cuando se aplica un campo magnético alterno, mostrando un gran potencial como actuadores magneto-mecánicos para la destrucción de células cancerígenas y como estimulantes de mangetotransducción. El estado vórtice puede ser el estado fundamental en un amplio rango de diámetros del disco desde la escala nanométrica hasta el rango sub-100 nm. En este capítulo se investigan las propiedades magnéticas de discos de Permalloy de diferentes dimensiones tanto cuando están pegados al sustrato como cuando son posteriormente liberados.

Como hemos mencionado más arriba, hay un interés especial en desarrollar nanoestructuras que muestren una mayor biocompatibilidad que no contengan Níquel, manteniendo sin embargo, una alta magnetización de saturación y remanencia nula. A tal fin, hemos investigado la fabricación de nanoestructuras compuestas de Fe para aplicaciones biomédicas debido a su alta saturación de magnetización y menor toxicidad comparado con otros elementos magnéticos como Co y Ni o aleaciones como el NiFe. En el capítulo 5 se han investigado dos tipos de nanoestructuras de Fe con distintas configuraciones magnéticas: estado vórtice e imanes aniferromagnéticos sintéticos. Por un lado, hemos evidenciado la existencia de estado vórtice en nanoestructuras de Fe en el rango submicrométrico e investigado sus propiedades dependientes de la relación de aspecto (espesor/diámetro). Por otro, además de las nanoestructuras de Fe en estado vórtice, hemos estudiado una configuración magnética más compleja basada en estructuras multicapa: los imanes antiferromagnéticos sintéticos. Estas nanoestructuras consisten básicamente en dos capas ferromagnéticas del mismo espesor separadas por una capa no magnética. Variando el espesor de la capa separadora se puede conseguir un acoplamiento antiparalelo entre las capas ferromagnéticas dando lugar a una magnetizacion nula en ausencia de campo magnético externo. En este

capítulo hemos explicado cómo hemos logrado el alineamiento antiparalelo de estructuras patronadas de Fe/Ti/Fe por medio de interacciones magnetostáticas. También hemos llevado a cabo un estudio comparativo de los dos tipos de nanoestructuras estudiadas en el capítulo y dada la simplicidad de la fabricación y las excelentes propiedades magnéticas comparadas con los imanes antiferromagnéticos, las nanoestructuras en estado vórtice fueron las seleccionadas para los posteriores ensayos en los siguientes capítulos.

Objetivo 3: Estudio del comportamiento dinámico de las nanoestructuas magnéticas en solución: respuesta a los campos magnéticos externos y procesos de relajación.

Cuando se aplica un campo magnético externo, los nanodiscos magnéticos experimentan un torque que les hace rotar para alinear su plano con la dirección del campo. Se puede sacar partido de este torque para ejercer fuerzas mecánicas sobre células y manipular sus señales celulares o incluso desencadenar la apoptosis, entre otras aplicaciones.

Dado que fuerzas de distintas intensidades y condiciones dinámicas pueden regular distintas respuestas celulares, es de gran interés el estudio de la respuesta dinámica de las nanoestructuras cuando están sujetas a campos magneticos alternos. En el capítulo 6 estudiamos la dinamica de los discos tanto de Fe como de Permalloy mediante la modulación de la luz que atraviesa los discos en suspension, que se origina de la variación de la sección transversal de scattering debido a la orientación/relajación de los discos cuando se aplica un campo magnético alterno en la dirección del haz de luz incidente.

Objetivo 4. Ensayos de citotoxicidad para el estudio de la viabilidad de las nanoestructuras diseñadas en cultivos celulares.

En el capítulo 7 se estudió la viabilidad de los discos en estado vórtice de Permalloy y de Fe en cultivos celulares de melanoma primario. Todos los discos usados en los ensayos de citotoxicidad se cubrieron de Ti por ambas caras en el proceso de fabricación para evitar la oxidación del material

magnético. Llevamos a cabo un estudio de los efectos de citotoxicidad para discos de distintos tamaños y composiciones (Py vs Fe).

[1] D.-H. Kim, E. A. Rozhkova, I. V Ulasov, S. D. Bader, T. Rajh, M. S. Lesniak, and V. Novosad, "Biofunctionalized magnetic-vortex microdiscs for targeted cancer-cell destruction," *Nat. Mater.*, vol. 9, no. 2, pp. 165–171, 2010.

Table of Contents

Chapter 1

General introduction

Magnetic nanoparticles present unique properties that make them highly advantageous for biomedical applications. Firstly, they have tunable sizes in the nanometric scale comparable to those of biological entities. Moreover, due to their magnetic nature, they can be manipulated by means of external magnetic fields offering a number of functionalities including the external guidance towards targeted sites. In addition to this and very importantly, magnetic nanoparticles can respond to alternating magnetic fields with an associated energy transfer, which can be exploited to develop targeted diagnosis and treatment approaches. Taking advantage of these properties, magnetic nanoparticles have yielded highly promising results in several areas of biomedical research such as drug delivery[1]–[3], magnetic hyperthermia[4]–[6], and contrast agents in magnetic resonance imaging, MRI[7]–[10].

Superparamagnetic nanoparticles synthesized by chemical procedures have been widely used for this purpose. These nanoparticles exhibit zero remanence, which is crucial for biomedical applications as it prevents

particles from agglomeration when dispersed in solution. However, one of the biggest drawbacks for such nanoparticles, which are typically iron oxides, is their low magnetic moments. This represents a serious limitation of its efficiency[11]. Higher magnetic moments could be achieved by increasing the size of the nanoparticles but superparamagnetic nanoparticles of higher dimensions would overcome the superparamagnetic limit giving rise to non-zero remanence, which can be translated into non-desirable particle aggregation. By contrast, top-down fabrication routes combining lithography and physical vapor deposition techniques allow the production of nanostructures of higher magnetization -magnetic moments per unit volume- since pure elements and alloys can be deposited[12]. Moreover, magnetic nanostructures with large dimensions can be obtained while preserving zero remanence. Hence, these routes provide high versatility for the design of magnetic configurations, playing with different sizes and geometries, and the significant advantage to grow multilayers of dissimilar materials with designed magnetic properties[13]–[15].

Top-down fabrication routes yield flat magnetic nanostructures (hereinafter referred to as MNS) with strong shape anisotropy, in contrast to most synthesized spherical magnetic nanoparticles (hereinafter referred to as MNP). When an alternating field is applied, MNS rotate to align the magnetic moment along the field direction. Consequently, the torque or the mechanic force they exert can be exploited to manipulate soft matter[16] and are highly promising for a wide range of applications including biomedicine, rheology and optics[17]–[19]. Specifically, there is increasing interest in the mechanical stimulation of biological cells. It is well known that cells convert mechanical stimulus into biochemical signals through a mechanism called mechanotransduction. The ability of manipulating cell signal in a remote manner by means of external magnetic fields opens up a wide variety of possibilities for the development of new clinical treatments. By now, only MNP have been used for this purpose in areas including regenerative medicine[20] and neurostimulation[21], [22]. The use of MNS

might provide a significant advance due to their distinctive feature of non-isotropic elements.

An innovative application of MNS based on this mechanical stimulus was proposed as a promising cancer therapy by Kim et al. They investigated the use of vortex state disks with 1 μm of diameter fabricated by photolithography for cancer cell destruction in-vitro assays[23]. The photolithographic technique has a limitation of the element size in the micrometer range. Although this study held great promise for the translation of the magnetic targeting to clinical applications, two main issues were claimed to be addressed[24]. Firstly, the limitation of photolithography in the element size in the micrometer range, being crucial for clinical applications to scale down into the submicrometer scale. Secondly, the need of developing more biocompatible disks not containing Nickel. Submicrometric MNS can be achieved by means of alternative lithographic techniques[25]–[28]. Among them, interference lithography (IL) is an excellent candidate. This technique enables to pattern large areas without the use of a mask or costly solid stamps allowing nanofabrication at significant lower-cost. Moreover, it is a versatile technique. Patterns of different sizes –few hundreds of nm in diameter- and geometries –disks, ellipses, and lines- can be simply obtained by changing the incident angle of the laser beam and the exposure dose. For this reason, this technique embraces many uses in a variety of subjects, as energy conversion[29], biotemplating[30], electronics[31]–[33], photonics[34], [35], and nanomedicine[36], [37].

In this scenario, the objectives of the thesis are the following:

1. Design of a cost-effective strategy based on IL to fabricate high-magnetic moment nanostructures suitable for biomedical applications.
2. Fabrication of magnetic nanostructures with unique spin configurations maintaining zero remanence as required in

biomedicine: vortex-state and in-plane synthetic antiferromagnets of different compositions, and sizes.

3. Study of the dynamic behavior of the magnetic nanostructures in solution, response to external fields and relaxation processes.
4. Citotoxicity assays to study the viability of the engineered nanostructures in cell cultures.

The distribution of the thesis into different chapters to address each of the objectives is presented as follows.

Objective 1: Design of a cost-effective strategy based on IL to fabricate high-magnetic moment nanostructures suitable for biomedical applications.

The top-down fabrication methods originally used for patterning surfaces for microelectronics have become an attractive fabrication approach of magnetic nanostructures for biomedical applications[38], [39] due to three main reasons: firstly, the combination of lithography with physical vapor deposition techniques has allowed the fabrication of nanostructures with good control of shape and dimensions; secondly, pure magnetic materials and alloys can be deposited making it possible to develop nanostructures with high magnetic moments while preserving the zero remanence (i.e. vortex-state disks) can be fabricated with this approach; thirdly, non magnetic layers can be deposited to protect the nanostructures against the oxidizing power of aqueous suspensions. Chapter 2 consists on the description of the main principles of the experimental techniques and the basic operation of the equipment used in this thesis either for fabrication or characterization of magnetic nanostructures, with particular emphasis on the description of the Interference Lithography system. The cost effective IL technique enables to pattern large areas (cm^2), leading to high mass production of MNS for biomedical assays. The set up of the equipment makes easy to tailor the shape and the size of the nanoelements, from about 50 nm to a few microns, which enables to engineer MNS with specific magnetic properties.

In chapter 3, we present two alternative routes for the fabrication of magnetic nanostructures in suspension taking advantage of the possibility of using positive and negative resist tones in our IL system, which enable to fabricate templates of resist pillars and resist antidots, respectively. After the deposition of the magnetic stack and the removal of the resist in a lift-off process, a crucial step is the release of the MNS from the substrate into aqueous solution, for which each route provides a different approach. This chemical etching can modify, and even spoil, the magnetic properties of the nanoelements. This procedure was optimized for two distinctive sacrificial layers, Ge and Al. Advantages and disadvantages of the proposed fabrication routes were discussed.

Objective 2: Fabrication of magnetic nanostructures with unique spin configurations maintaining zero remanence as required in biomedicine: vortex-state and in-plane synthetic antiferromagnets of different compositions, and sizes.

The second objective was addressed along chapters 4 and 5, in which we performed a comprehensive study of the magnetic properties of three types of disk-shaped nanostructures: vortex-state Permalloy MNS in chapter 4, vortex-state Fe MNS and Synthetic Antiferromagnets (SAF's) in chapter 5.

Chapter 4 focuses on the characterization of vortex-state Permalloy (NiFe) disks fabricated by interference lithography (IL) through the two alternative strategies described in chapter 3. Disk-shaped nanostructures with vortex-state configuration are characterized by an in-plane flux-closure spin distribution resulting in a net zero magnetization in the absence of external magnetic field[40], [41]. These nanostructures are interesting for biological applications as they exhibit zero remanence (required to prevent from particle aggregation) and rotate when an alternating magnetic field is applied, showing great potential as magneto-mechanical actuators for cancer cell destruction and mechano-transduction stimulants. The vortex state can be a ground state in a wide range of disk diameters from the submicrometric scale down to the sub-100nm range[42], [43]. The magnetic

properties of the disks attached to the substrate and then released into solution were investigated in this chapter for Permalloy disks of different dimensions.

As we mentioned above, there is special interest in developing more biocompatible magnetic nanostructures not containing Nickel while maintaining the high saturation magnetization and zero remanence. For this purpose we investigated the development of MNS composed of metallic Fe for biomedical applications due to its higher saturation magnetization and reduced toxicity compared to other magnetic elements such as Co, Ni and alloys like NiFe. Two magnetic configurations were investigated in chapter 5 for metallic Fe nanostructures: spin vortex-state and synthetic antiferromagnets (SAF).

The magnetization reversal of vortex-state nanostructures has been reported over a wide range of dimensions (from a few tens of nanometers to one micron) in Permalloy[44]–[47], Superpermalloy[48], and Co[49]–[54]. Although spin vortex state has also been found experimentally and theoretically in sub-100nm Fe dots[55]–[58], little investigation has been carried out by now on Fe disks in the submicrometric range. In chapter 5 we revealed the existence of vortex state in Fe MNS in the submicrometric range and investigated their size dependent magnetic properties. Besides the vortex state Fe MNS, a different class of disk-shaped MNS with a more complex magnetic configuration based on multilayer structures was studied, the synthetic antiferromagnetic nanostructures (SAF). These MNS consist basically on two ferromagnetic layers of the same thickness separated by a thin non-magnetic spacer layer. By tuning the thickness of the spacer, an antiparallel alignment of the magnetizations of the ferromagnetic layers can be obtained leading to a zero net magnetization in absence of external field[59]–[61]. Depending on the thickness of the spacer, the coupling between the ferromagnetic layers can be mainly mediated by magnetostatic or interlayer exchange interactions. We achieved antiparallel alignment on patterned Fe/Ti/Fe structures by means of magnetostatic interactions. We carried out a comparative study between the obtained Fe

vortex-state disks and the SAF's. Due to the simplicity of the fabrication and the excellent magnetic properties compared to SAF's, single layer disks with spin vortex configuration were chosen for their fabrication in solution for further assays in the following chapters.

Objective 3: Study of the dynamic behavior of the magnetic nanostructures in solution.

When an external magnetic field is applied to disk-shape MNS, they experience a driving torque that rotates the disk to align the plane of the disk along the field direction. This torque can be exploited to exert mechanical forces on biological cells to manipulate their cell signal or even trigger cell apoptosis, among other applications.

Since forces of different strengths and dynamic conditions can regulate several cell responses[62], it is of great importance to study the dynamic response of MNS when subjected to alternating magnetic fields. In Chapter 6 we studied the dynamic properties of vortex-state disks of Fe and Permalloy through the modulation of the light across disk suspensions, which arises from the variation of the scattering cross-section due to the disks orientation/relaxation when an alternating field is applied along the incident beam direction.

Objective 4: Citotoxicity assays to study the viability of the engineered nanostructures in cell cultures.

In chapter 7 the viability of submicrometric disks of Permalloy (NiFe) and also of pure Fe with vortex-state configuration was assessed in primary melanoma cell cultures. All disks used in the citotoxicity assays were coated by Ti in the fabrication strategy to prevent from oxidation. We studied the citotoxicity effects at different disk sizes and compositions (Py vs Fe).

References

[1] S. Mura, J. Nicolas, and P. Couvreur, "Stimuli-responsive nanocarriers for drug delivery," *Nat. Mater.*, vol. 12, no. 11, pp. 991–1003, 2013.

[2] S. Noh, S. H. Moon, T.-H. Shin, Y. Lim, and J. Cheon, "Recent advances of magneto-thermal capabilities of nanoparticles: from design principles to biomedical applications," *Nano Today*, vol. 13, pp. 61–76, 2017.

[3] D. V Voronin, O. A. Sindeeva, M. A. Kurochkin, O. Mayorova, I. V Fedosov, O. Semyachkina-Glushkovskaya, D. A. Gorin, V. V Tuchin, and G. B. Sukhorukov, "In vitro and in vivo visualization and trapping of fluorescent magnetic microcapsules in a bloodstream," *ACS Appl. Mater. Interfaces*, vol. 9, no. 8, pp. 6885–6893, 2017.

[4] R. A. Revia and M. Zhang, "Magnetite nanoparticles for cancer diagnosis, treatment, and treatment monitoring: recent advances," *Mater. Today*, vol. 19, no. 3, pp. 157–168, 2016.

[5] A. C. Silva, T. R. Oliveira, J. B. Mamani, S. M. F. Malheiros, L. Malavolta, L. F. Pavon, T. T. Sibov, E. Amaro Junior, A. Tannus, and E. L. G. Vidoto, "Application of hyperthermia induced by superparamagnetic iron oxide nanoparticles in glioma treatment," *Int. J. Nanomedicine*, vol. 6, pp. 591–603, 2011.

[6] R. Grillo, J. Gallo, D. G. Stroppa, E. Carbó-Argibay, R. Lima, L. F. Fraceto, and M. Bañobre-López, "Sub-Micrometer Magnetic Nanocomposites: Insights into the Effect of Magnetic Nanoparticles Interactions on the Optimization of SAR and MRI Performance," *ACS Appl. Mater. Interfaces*, vol. 8, no. 39, pp. 25777–25787, 2016.

[7] J. E. Rosen, L. Chan, D.-B. Shieh, and F. X. Gu, "Iron oxide nanoparticles for targeted cancer imaging and diagnostics," *Nanomedicine Nanotechnology, Biol. Med.*, vol. 8, no. 3, pp. 275–290, 2012.

[8] G. Zabow, S. Dodd, J. Moreland, and A. Koretsky, "Micro-engineered local field control for high-sensitivity multispectral MRI," *Nature*, vol. 453, no. 7198, p. 1058, 2008.

[9] V. Nandwana, S.-R. Ryoo, S. Kanthala, M. De, S. S. Chou, P. V Prasad, and V. P. Dravid, "Engineered Theranostic Magnetic Nanostructures: Role of Composition and Surface Coating on Magnetic Resonance Imaging Contrast and Thermal Activation," *ACS Appl. Mater. Interfaces*, vol. 8, no. 11, pp. 6953–6961, 2016.

[10] D. H. Ortgies, L. de la Cueva, B. del Rosal, F. Sanz-Rodríguez, N. Fernández, M. C. Iglesias-de la Cruz, G. Salas, D. Cabrera, F. J. Teran, and D. Jaque, "In vivo deep tissue fluorescence and magnetic imaging employing hybrid nanostructures," *ACS Appl. Mater. Interfaces*, vol. 8, no. 2, pp. 1406–1414, 2016.

[11] S. Dutz and R. Hergt, "Magnetic particle hyperthermia—a promising tumour therapy?," *Nanotechnology*, vol. 25, no. 45, p. 452001, 2014.

[12] W. Hu, R. J. Wilson, A. Koh, A. Fu, A. Z. Faranesh, C. M. Earhart, S. J. Osterfeld, S.-J. Han, L. Xu, S. Guccione, R. Sinclair, and S. X. Wang, "High-moment antiferromagnetic nanoparticles with tunable magnetic properties," *Adv. Mater.*, vol. 20, no. 8, p. 1479, 2008.

[13] R. Van Roosbroeck, W. Van Roy, T. Stakenborg, J. Trekker, A. D'Hollander, T. Dresselaers, U. Himmelreich, J. Lammertyn, and L. Lagae, "Synthetic antiferromagnetic nanoparticles as potential contrast agents in MRI," *ACS Nano*, vol. 8, no. 3, pp. 2269–2278, 2014.

[14] T. Vemulkar, R. Mansell, D. Petit, R. P. Cowburn, and M. S. Lesniak, "Highly tunable perpendicularly magnetized synthetic antiferromagnets for biotechnology applications," *Appl. Phys. Lett.*, vol. 107, no. 1, p. 12403, 2015.

[15] J. I. Martın, J. Nogues, K. Liu, J. L. Vicent, and I. K. Schuller, "Ordered magnetic nanostructures: fabrication and properties," *J. Magn. Magn. Mater.*, vol. 256, no. 1–3, pp. 449–501, 2003.

[16] R. M. Erb, J. J. Martin, R. Soheilian, C. Pan, and J. R. Barber,

"Actuating Soft Matter with Magnetic Torque," *Adv. Funct. Mater.*, vol. 26, pp. 3859–3880, 2016.

[17] R. M. Fratila, S. Rivera-Fernández, and M. Jesús, "Shape matters: synthesis and biomedical applications of high aspect ratio magnetic nanomaterials," *Nanoscale*, vol. 7, no. 18, pp. 8233–8260, 2015.

[18] W. Liu, Y. Bao, M. L. Lam, T. Xu, K. Xie, H. S. Man, E. Y. Chan, N. Zhu, R. H. W. Lam, and T.-H. Chen, "Nanowire Magnetoscope Reveals a Cellular Torque with Left–Right Bias," *ACS Nano*, vol. 10, no. 8, pp. 7409–7417, 2016.

[19] F. Li, J. Lu, X. Kong, T. Hyeon, and D. Ling, "Dynamic nanoparticle assemblies for biomedical applications," *Adv. Mater.*, 2017.

[20] L. J. Santos, R. L. Reis, and M. E. Gomes, "Harnessing magnetic-mechano actuation in regenerative medicine and tissue engineering," *Trends Biotechnol.*, vol. 33, no. 8, pp. 471–479, 2015.

[21] E. Colombo, P. Feyen, M. R. Antognazza, G. Lanzani, and F. Benfenati, "Nanoparticles: a challenging vehicle for neural stimulation," *Front. Neurosci.*, vol. 10, pp. 1–7, 2016.

[22] A. Kunze, P. Tseng, C. Godzich, C. Murray, A. Caputo, F. E. Schweizer, and D. Di Carlo, "Engineering cortical neuron polarity with nanomagnets on a chip," *ACS Nano*, vol. 9, no. 4, pp. 3664–3676, 2015.

[23] D.-H. Kim, E. A. Rozhkova, I. V Ulasov, S. D. Bader, T. Rajh, M. S. Lesniak, and V. Novosad, "Biofunctionalized magnetic-vortex microdiscs for targeted cancer-cell destruction," *Nat. Mater.*, vol. 9, no. 2, pp. 165–171, 2010.

[24] J. Dobson, "A twist on tumour targeting," *Nat Mater*, vol. 9, pp. 95–96, 2010.

[25] Y. Luo and V. Misra, "Large-area long-range ordered anisotropic magnetic nanostructure fabrication by photolithography," *Nanotechnology*, vol. 17, no. 19, p. 4909, 2006.

[26] L. J. Guo, "Nanoimprint lithography: methods and material requirements," *Adv. Mater.*, vol. 19, no. 4, pp. 495–513, 2007.

[27] C. L. Cheung, R. J. Nikolić, C. E. Reinhardt, and T. F. Wang, "Fabrication of nanopillars by nanosphere lithography," *Nanotechnology*, vol. 17, no. 5, p. 1339, 2006.

[28] C. A. Ross, M. Hwang, M. Shima, J. Y. Cheng, M. Farhoud, T. A. Savas, H. I. Smith, W. Schwarzacher, F. M. Ross, and M. Redjdal, "Micromagnetic behavior of electrodeposited cylinder arrays," *Phys. Rev. B*, vol. 65, no. 14, p. 144417, 2002.

[29] H.-J. Ahn, S.-I. Kim, J.-C. Yoon, J.-S. Lee, and J.-H. Jang, "Power conversion efficiency enhancement based on the bio-inspired hierarchical antireflection layer in dye sensitized solar cells," *Nanoscale*, vol. 4, no. 15, p. 4464, 2012.

[30] J. M. Galloway, S. M. Bird, J. E. Talbot, P. M. Shepley, R. C. Bradley, O. El-Zubir, D. A. Allwood, G. J. Leggett, J. J. Miles, S. S. Staniland, and K. Critchley, "Nano- and micro-patterning biotemplated magnetic CoPt arrays," *Nanoscale*, vol. 8, no. 22, p. 11738, 2016.

[31] J. A. Liddle and G. M. Gallatin, "Lithography, metrology and nanomanufacturing," *Nanoscale*, vol. 3, no. 7, p. 2679, 2011.

[32] J.-H. Min, A. Bagal, J. Z. Mundy, C. J. Oldham, B.-I. Wu, G. N. Parsons, and C.-H. Chang, "Fabrication and design of metal nano-accordion structures using atomic layer deposition and interference lithography," *Nanoscale*, vol. 8, no. 9, p. 4984, 2016.

[33] Z. Ma, C. Jiang, W. Yuan, and Y. He, "Large-scale Patterning of Hydrophobic Silicon Nanostructure Arrays Fabricated by Dual Lithography and Deep Reactive Ion Etching," *Nano-Micro Lett.*, vol. 5, no. 1, p. 7, 2013.

[34] M. Jin, H. van Wolferen, H. Wormeester, A. van den Berg, and E. T. Carlen, "Large-area nanogap plasmon resonator arrays for plasmonics applications," *Nanoscale*, vol. 4, no. 15, p. 4712, 2012.

[35] Q. Zhu, S. Zheng, S. Lin, T.-R. Liu, and C. Jin, "Polarization-dependent enhanced photoluminescence and polarization-independent emission rate of quantum dots on gold elliptical nanodisc arrays," *Nanoscale*, vol. 6, p. 7237, 2014.

[36] E. Lamers, X. F. Walboomers, M. Domanski, L. Prodanov, J. Melis, R. Luttge, L. Winnubst, J. M. Anderson, H. J. G. E. Gardeniers, and J. A. Jansen, "In vitro and in vivo evaluation of the inflammatory response to nanoscale grooved substrates," *Nanomed.-Nanotechnol. Biol. Med.*, vol. 8, no. 3, p. 308, 2012.

[37] M. Zhu, L. Zhou, B. Li, M. K. Dawood, G. Wan, C. Q. Lai, H. Cheng, K. C. Leong, R. Rajagopalan, H. P. Too, and W. K. Choi, "Creation of nanostructures by interference lithography for modulation of cell behavior," *Nanoscale*, vol. 3, no. 7, p. 2723, 2011.

[38] S. Leulmi, X. Chauchet, M. Morcrette, G. Ortiz, H. Joisten, P. Sabon, T. Livache, Y. Hou, M. Carrière, and S. Lequien, "Triggering the apoptosis of targeted human renal cancer cells by the vibration of anisotropic magnetic particles attached to the cell membrane," *Nanoscale*, vol. 7, no. 38, pp. 15904–15914, 2015.

[39] E. A. Vitol, V. Novosad, and E. A. Rozhkova, "Multifunctional ferromagnetic disks for modulating cell function," *IEEE Trans. Magn.*, vol. 48, no. 11, pp. 3269–3274, 2012.

[40] R. P. Cowburn, D. K. Koltsov, A. O. Adeyeye, M. E. Welland, and D. M. Tricker, "Single-domain circular nanomagnets," *Phys. Rev. Lett.*, vol. 83, no. 5, p. 1042, 1999.

[41] K. Y. Guslienko, V. Novosad, Y. Otani, H. Shima, and K. Fukamichi, "Magnetization reversal due to vortex nucleation, displacement, and annihilation in submicron ferromagnetic dot arrays," *Phys. Rev. B*, vol. 65, no. 2, p. 24414, 2001.

[42] K. Y. Guslienko, "Magnetic vortex state stability, reversal and dynamics in restricted geometries," *J. Nanosci. Nanotechnol.*, vol. 8, no. 6, pp. 2745–2760, 2008.

[43] S.-H. Chung, R. D. McMichael, D. T. Pierce, and J. Unguris, "Phase diagram of magnetic nanodisks measured by scanning electron microscopy with polarization analysis," *Phys. Rev. B*, vol. 81, no. 2, p. 24410, 2010.

[44] K. Y. Guslienko, V. Novosad, Y. Otani, H. Shima, and K. Fukamichi, "Field evolution of magnetic vortex state in ferromagnetic disks," *Appl. Phys. Lett.*, vol. 78, no. 24, pp. 3848–3850, 2001.

[45] V. Novosad, K. Y. Guslienko, H. Shima, Y. Otani, K. Fukamichi, N. Kikuchi, O. Kitakami, and Y. Shimada, "Nucleation and annihilation of magnetic vortices in sub-micron permalloy dots," *IEEE Trans. Magn.*, vol. 37, no. 4, pp. 2088–2090, 2001.

[46] T. Pokhil, D. Song, and J. Nowak, "Spin vortex states and hysteretic properties of submicron size NiFe elements," *J. Appl. Phys.*, vol. 87, no. 9, pp. 6319–6321, 2000.

[47] J. K. Ha, R. Hertel, and J. Kirschner, "Micromagnetic study of magnetic configurations in submicron permalloy disks," *Phys. Rev. B*, vol. 67, no. 22, p. 224432, 2003.

[48] R. P. Cowburn, "Property variation with shape in magnetic nanoelements," *J. Phys. D. Appl. Phys.*, vol. 33, no. 1, p. R1, 2000.

[49] A. Fernandez and C. J. Cerjan, "Nucleation and annihilation of magnetic vortices in submicron-scale Co dots," *J. Appl. Phys.*, vol. 87, no. 3, pp. 1395–1401, 2000.

[50] E. Girgis, J. Schelten, J. Shi, J. Janesky, S. Tehrani, and H. Goronkin, "Switching characteristics and magnetization vortices of thin-film cobalt in nanometer-scale patterned arrays," *Appl. Phys. Lett.*, vol. 76, no. 25, pp. 3780–3782, 2000.

[51] L. D. Buda, I. L. Prejbeanu, U. Ebels, and K. Ounadjela, "Micromagnetic simulations of magnetisation in circular cobalt dots," *Comput. Mater. Sci.*, vol. 24, no. 1–2, pp. 181–185, 2002.

[52] A. Lebib, S. P. Li, M. Natali, and Y. Chen, "Size and thickness

dependencies of magnetization reversal in Co dot arrays," *J. Appl. Phys.*, vol. 89, no. 7, pp. 3892–3896, 2001.

[53] M. Natali, A. Lebib, Y. Chen, I. L. Prejbeanu, and K. Ounadjela, "Configurational anisotropy in square lattices of interacting cobalt dots," *J. Appl. Phys.*, vol. 91, no. 10, pp. 7041–7043, 2002.

[54] M. Natali, I. L. Prejbeanu, A. Lebib, L. D. Buda, K. Ounadjela, and Y. Chen, "Correlated magnetic vortex chains in mesoscopic cobalt dot arrays," *Phys. Rev. Lett.*, vol. 88, no. 15, p. 157203, 2002.

[55] R. K. Dumas, C.-P. Li, I. V Roshchin, I. K. Schuller, and K. Liu, "Magnetic fingerprints of sub-100 nm Fe dots," *Phys. Rev. B*, vol. 75, no. 13, p. 134405, 2007.

[56] J. Mejía-López, D. Altbir, A. H. Romero, X. Batlle, I. V Roshchin, C.-P. Li, and I. K. Schuller, "Vortex state and effect of anisotropy in sub-100-nm magnetic nanodots," *J. Appl. Phys.*, vol. 100, no. 10, p. 104319, 2006.

[57] I. V Roshchin, C.-P. Li, H. Suhl, X. Batlle, S. Roy, S. K. Sinha, S. Park, R. Pynn, M. R. Fitzsimmons, and J. Mejía-López, "Measurement of the vortex core in sub-100 nm Fe dots using polarized neutron scattering," *EPL (Europhysics Lett.*, vol. 86, no. 6, p. 67008, 2009.

[58] J. Mejía-López, D. Altbir, P. Landeros, J. Escrig, A. H. Romero, I. V Roshchin, C.-P. Li, M. R. Fitzsimmons, X. Batlle, and I. K. Schuller, "Development of vortex state in circular magnetic nanodots: Theory and experiment," *Phys. Rev. B*, vol. 81, no. 18, p. 184417, 2010.

[59] W. Hu, R. J. Wilson, C. M. Earhart, A. L. Koh, R. Sinclair, and S. X. Wang, "Synthetic antiferromagnetic nanoparticles with tunable susceptibilities," *J. Appl. Phys.*, vol. 105, no. 7, p. 07B508, 2009.

[60] W. Zhang and K. M. Krishnan, "Direct release of synthetic antiferromagnetic nanoparticles fabricated by defect-free thermal imprinting," *J. Appl. Phys.*, vol. 111, no. 7, p. 07B509, 2012.

[61] A. L. Koh, W. Hu, R. J. Wilson, C. M. Earhart, S. X. Wang, and R.

Sinclair, “Structural and magnetic characterizations of high moment synthetic antiferromagnetic nanoparticles fabricated using self-assembled stamps,” *J. Appl. Phys.*, vol. 107, no. 9, p. 09B522, 2010.

[62] B. D. Hoffman, C. Grashoff, and M. A. Schwartz, “Dynamic molecular processes mediate cellular mechanotransduction,” *Nature*, vol. 475, no. 7356, pp. 316–323, 2011.

Chapter 2

Experimental techniques

2.1. Introduction

In this chapter we describe the main principles of the experimental techniques and the basic operation of the equipment used in this thesis either for fabrication or characterization of magnetic nanostructures. An important part of the chapter is dedicated to interference lithography (IL), which is the technique employed for the fabrication of resist templates that confer the dimensions and morphological properties to the nanostructures. We explained the operation of the Lloyd's mirror interferometer, which is the equipment used for the IL exposures, including its functionalities for tailoring the geometry, order and dimensions of the nanoelements. Moreover, we explained the difference between the positive and negative resist-tones, which will be important players in the two fabrication routes that we engineered for the fabrication of nanostructures in solution. The techniques used for the deposition of the magnetic material on the resist templates; thermal and electron beam evaporation were subsequently

described. The last sections of the chapter were dedicated to the characterization techniques used for determining either the morphological properties of the nanostructures; scanning electron microscopy (SEM) and atomic force microscopy (AFM) or their magnetic behavior; superconducting quantum interference device (SQUID) and magneto-optical kerr effect (MOKE).

2.2. Interference Lithography

Interference Lithography (IL) is an effective method for the fabrication of periodic nanostructures over large substrate areas (cm^2) at short exposure times by means of simple equipment. The principle of IL is easy two mutually coherent beams of light interfere to create a periodic intensity pattern, which is recorded on a photosensitive material[63].

One of the main advantages of this technique is that large areas can be patterned without the use of a photomask allowing nanofabrication at significant lower-cost[64]. Moreover, patterns of different sizes, geometries and periodicities can be obtained simply by changing the configuration of the system.

In this thesis, a Lloyd's mirror interferometer system was used for the lithographic exposures[65]. This system provides high-contrast interference patterns and enables to easily adjust the periodicity of the patterns as it is explained below.

In our Lloyd's mirror set-up a mirror is placed orthogonal to the sample holder, as shown in the schematic in figure 2.1 [65], [66]. The light coming from a Helium Cadmium laser emitting at 325 nm illuminates both the mirror and the sample. The part of the light that is reflected on the mirror surface interferes with the part of the beam that is directly illuminating the sample[67].

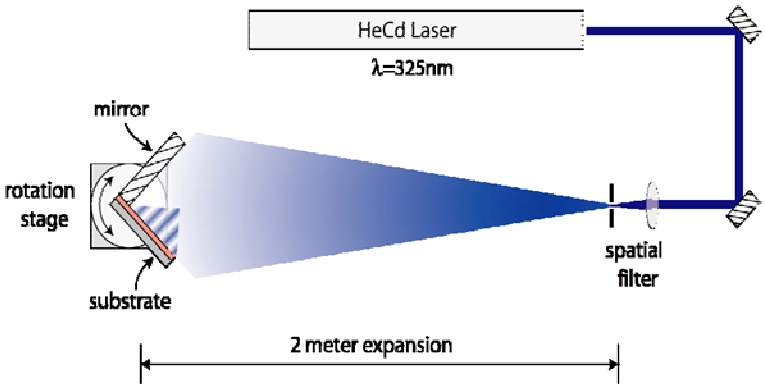

Figure 2.1. Schematic of the Lloyd's Mirror Interferometer.

This interference is recorded on a photoresist as a line pattern with the periodicity given by (2.1), where λ is the wavelength, (325 nm for this system), and θ is half the angle of the two interfering beams (Figure 2.2 (a)).

$$p = \lambda/2 \sin(\theta) \tag{2.1}$$

The mirror and the sample holder are mounted on a rotation stage. Thus, the period of the line pattern can be easily adjusted by rotating the stage (changing the angle θ) without the need to realign the optical path.

2.2.1. Transference of the intensity pattern

In a Lloyd's mirror setup the periodic intensity pattern created by the interference of the incident beam and the beam reflected by the mirror is transferred to a photoresist coated onto a substrate (Figure 2.2(a)). Generally, a bottom anti-reflective coating (BARC) is needed to avoid a second interference pattern on the vertical axis created by the interference of the incident light and the light reflected by the substrate (Figure 2.2(b)). The combination of the two interference patterns would give rise to the intensity

distribution showed in figure 2.2(c). This undesired vertical pattern can degrade the sidewall resist profiles in the developed resist.

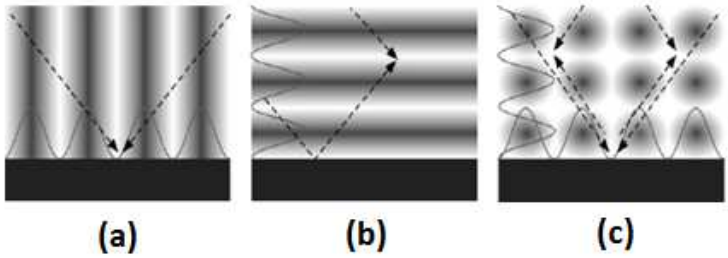

Figure. 2.2. a) The fringe pattern through the thickness of the resist formed by the interference of the incident beam and the beam reflected by the mirror. b) A second interference pattern caused by the substrate reflection. c) The overlapping of the two interference patterns.

The period of the vertical waves is given by (2.2), where λ is the wavelength of the laser, n is the refractive index of the resist and θ is the angle of interference.

$$p_{vertical} = \frac{\lambda}{2n\cos\theta} \tag{2.2}$$

The ARC's are used to remove the vertical standing waves and enable a good profile of the photoresist. However, a well defined profile of the resist pattern also requires an adequate exposure dose. The dose is often calculated by multiplying the intensity of the incident light by the time of the exposure. Figure 2.3 shows the effects of underexposure (a) and overexposure (b) on resist patterns obtained by our IL system and the satisfactory resist profile on a resist pattern that received the correct dose (c).

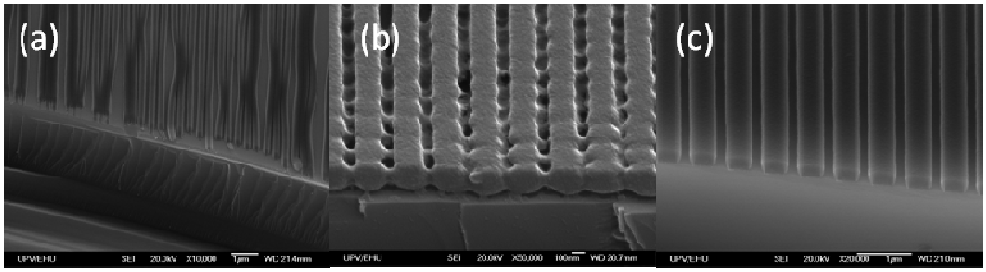

Figure 2.3. SEM images of arrays of lines obtained by Interference Lithography at different exposure times: a) Underexposed resist pattern, b) Overexposed resist pattern c) Resist pattern with a favorable line profile obtained by a correct exposure dose.

2.2.2. Tailoring the order and geometry

Besides line patterns, which are obtained with a single exposure, dot patterns and more complex geometries can be written by multiple exposures[68][69]. The shape and the order of the pattern can be adjusted by setting the angle between exposures. For example, a double exposure performed with the sample rotated 90º with respect to the first exposure leads to a square array of nanoelements, while a doble exposure with the sample rotated 60º in the second exposure gives rise to a hexagonal array. The dose also plays a crucial role in determining the size and geometry of the nanoelements. Regarding geometry, a double exposure with the same dose for each exposure leads to a circular dot pattern. However, different doses for the double exposures gives rise to elliptical dots with eccentricities depending on how different are the doses. Figure 2.4 shows a set of arrays obtained by IL with different order, element sizes and geometries.

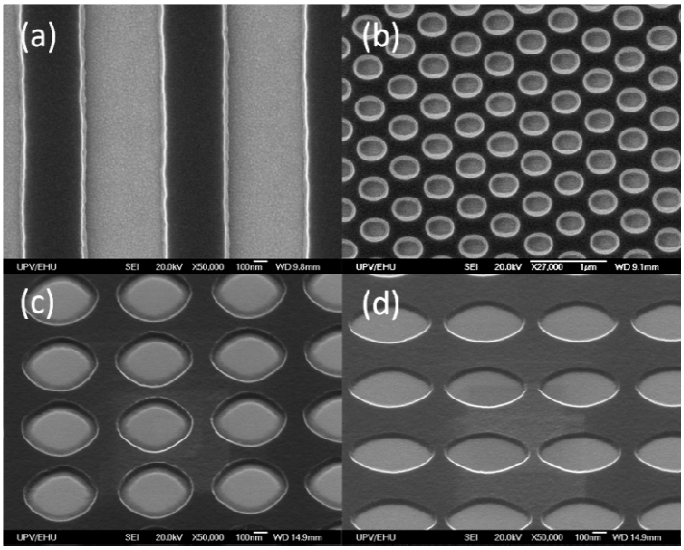

Figure 2.4. Scanning electron microscopy (SEM) images of arrays of nanoelements of different order, size and geometry obtained by IL: (a) Array of lines from a single exposure, (b) hexagonal array of ellipses from a double exposure (60º rotation) with different dose, (c) and (d) square array of ellipses of different aspect ratio from a double exposure (90ºrotation) with different dose.

The resolution of the Lloyd's mirror Interferometer is determined by the wavelength of the laser beam. The period of the pattern can be as low as half of the wavelength so the system enables to fabricate patterns with periodicities between ~170 nm and a few microns[65]. Moreover, by adjusting the dose, nanoelements as small as 30 nm can be obtained[28].

2.2.3. Positive and negative tone resists

According to how photoresists interact with light, they can be divided in two groups: the so-called positive and negative resist-tones. In positive resists, the regions exposed to light change its chemical structure and become soluble to the developer, while unexposed regions remain insoluble. Negative resists behave in the opposite manner. The regions

exposed to light crosslink and become insoluble to the developer so only the exposed areas are removed in the development [70].

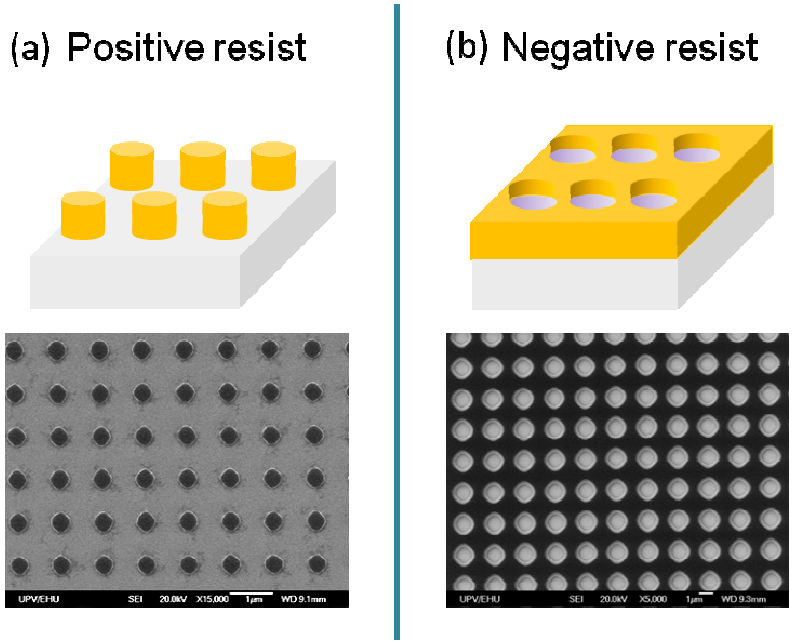

Figure 2.5. Scheme and SEM image of dot and antidot arrays obtained by IL using a) positive resist, b) negative resist.

If we perform a single exposure with a Lloyd's mirror Interferometer using either the positive or the negative resist, we obtain resist line patterns after development. However, if we are interested in the fabrication of grids and we perform a double exposure, we can produce different resist structures by using the two types of resists. In fact, a second exposure with the sample rotated 90º between exposures yield square arrays of dots or resist pillars (Figure 2.5(a)) for positive resists and arrays of antidots or holes (Figure 2.5(b)) for negative resists. Indeed, the resist template for the negative resist corresponds to the "photographic negative" of the resist pattern fabricated with the positive resist.

This possibility of fabricating arrays of dots and antidots gave rise to two fabrication routes for disk-shaped magnetic nanostructures in solution as we will see in the next chapter.

2.3. Material deposition techniques: Thermal and electron beam evaporation

Evaporation is a simple method for the deposition of thin films. Basically, a vapor is originated by evaporating or subliming a target material, which is subsequently condensed on a substrate[71]. We used two different evaporation techniques: the thermal and electron beam evaporation.

2.3.1. Thermal evaporation technique

In this technique, the target material is heated in a vacuum chamber using an electric resistance heater. A pair of feedthroughs is employed to flow a significant current through the heater made of a refractory material such as tungsten or molybdenum. The most common heaters in thermal evaporation are called "boats" and consist of a refractory ribbon with dimple on the top side, into which the target material is placed (i.e. in the form of pellets). The current that passes through the boat is increased progressively until the target material starts to evaporate. At this point, the rate of the evaporation can be increased by increasing the current, and vice versa. The scheme of the thermal evaporation equipment is shown in figure 2.6.

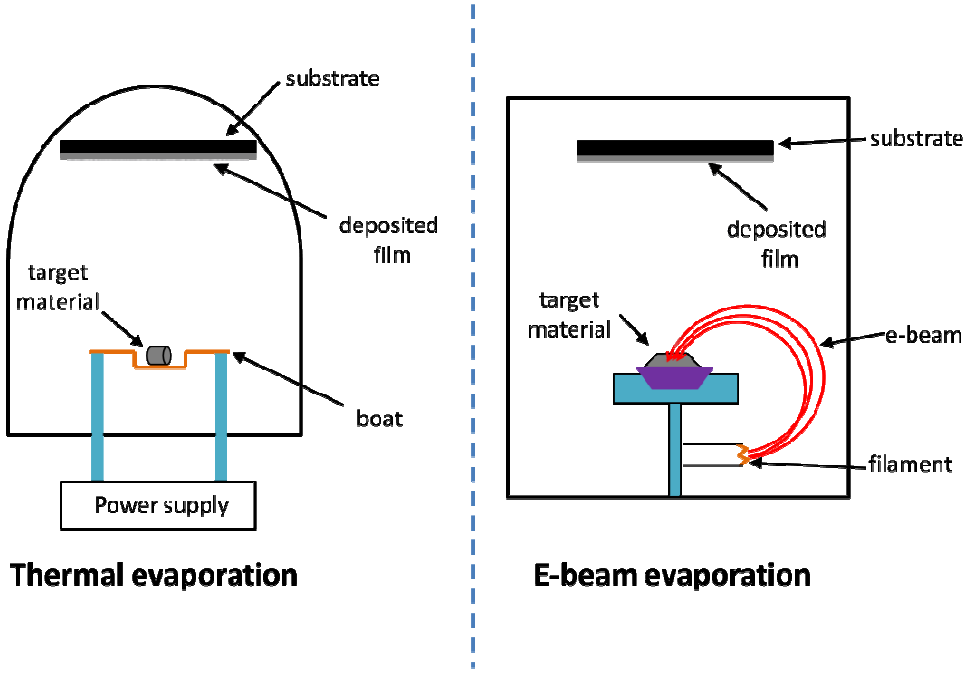

Figure 2.6. Scheme of the thermal and e-beam evaporation equipment used in this thesis.

The thermal evaporation was carried out in a high vacuum chamber equipped with two thermal evaporation sources and a quartz micro-balance for the control of the film thickness.

We use this technique for the material deposition step of the fabrication process of Pemalloy vortex-state disks.

Despite this technique enables successful evaporation of plenty of materials, several inconveniencies arise when using alloys as target materials. A common characteristic when evaporating alloys is that the ratio of the components of is not reproduced in the deposited film resulting in a compositional gradient across the thickness[72]. Moreover, when depositing Permalloy we had to use alternative heaters to the common refractive boats (made of tungsten or molybdenum) since we found that Permalloy alloyed with them before or during evaporation.

Among the different heaters made of different materials that we tried, we found that the heaters including Alumina enabled the evaporation of Py without an apparent interaction between the Py and the heater material. We used Alumina crucibles inserted into crucible box heaters (that concentrate the heat source toward the crucible) and tungsten boats coated with Alumina.

2.3.2. Electron beam evaporation

This evaporation technique consists on an electron beam generated by a filament that is guided via electric and magnetic fields to strike a target material and vaporize it in a vacuum chamber. The electron beam collides with the surface of the target material causing it to heat up and vaporize, as the electrons transfer their kinetic energy of motion. The evaporated material will traverse the vacuum chamber and coat the surface of a substrate placed above the target material. The set up of the equipment is shown in figure 2.6.

In this process, heating can be very localized leading to a very low container contamination, which represents a great advantage over the thermal evaporation. Moreover, evaporation is not limited by the melting point of a target material, so even the highest temperature materials can be evaporated.

We used e-beam evaporation equipment for the fabrication of synthetic antiferromagnets (SAF) composed of sequences of layers of Fe and Ti deposited at a base pressure of 10^{-8} Torr with deposition rates of 0.5 Å/s and 0.3 Å/s, respectively. The system was equipped with a rotary pocket electron beam source that enables to evaporate a number of materials sequentially in a single process. In addition to this, the equipment includes a linear motion shutter that allows to grow wedges and also, several samples at the same time with layers of different thicknesses. This made it possible to study the interactions across the Ti spacer by varying either the

Ti thickness or the thickness of the magnetic layers deposited at the same conditions.

2.4. Scanning electron microscopy (SEM)

Scanning electron microscopy is a method for high-resolution imaging of surfaces, in which an incident electron beam is scanned in a raster pattern across the sample's surface. The electrons, typically produced by a thermal emission source, interact with the atoms in the sample producing various signals that contain information about the sample's topography and composition. These signals arise from the energy exchange between the electron beam and the sample resulting in electrons and electromagnetic radiation emerging from the sample[73]. The detection of the secondary electrons emitted by the atoms excited by the electron beam generates the SEM image with high resolution. The main advantages of SEM over light microscopy include much higher magnification (> 100.000X) with an ultimate resolution of 1nm and greater depth of field (up to 100 times that of light microscopy)[74].

Scanning electron microscopy was used in this thesis mainly to verify the homogeneity of the arrays of nanostructures and characterize the geometry and lateral dimensions of the nanoelements in the fabrication process (Figure 2.7(a)). When the nanostructures are released from the substrate into solution, we also use SEM to characterize them. In this case, the preparation of the sample for the SEM measurements consists of drying a droplet of an aqueous solution of nanostructures on a Si wafer. The nanostructures have to be dried because SEM requires vacuum for optimal operation and do not permit high-quality imaging in either ambient air or in a liquid environment. A SEM image of dried Permalloy disks is shown in figure 2.7(b). As we can observe in the image, at an acceleration voltage of 20 kV the disks appear translucent to the electrons making it possible to distinguish the disks located at different layers.

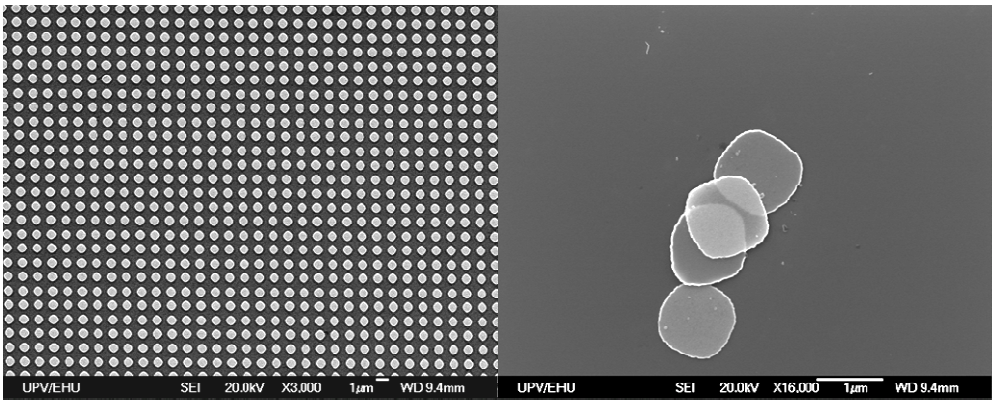

Figure 2.7. SEM images of: (a) array of Permalloy disks attached to the substrate, (b) released disks and subsequently dried on a silicon wafer.

2.5. Atomic Force Microscopy (AFM)

Atomic Force Microscopy is a scanning probe technique, in which a small probe scans the sample to obtain information about the surface of the sample. The information obtained from the interaction between the probe and the sample ranges from topography to more complex measurements such as physical and magnetic properties of the sample. Regarding topographic measurements, the main advantage of AFM is that it provides height information.

The standard AFM probes consist of a tip mounted on a cantilever (Figure 2.8). The interatomic forces between the tip and the surface of the sample provoke the deflection of the cantilever. A laser beam is reflected by a cantilever and collected by a photodiode, which register the changes in the position of the reflected beam due the deflection of the cantilever as the topography of the sample surface changes[75]. The photodiode converts those changes into electric signals that are processed by a computer and transformed into topographic image of a small area of the sample.

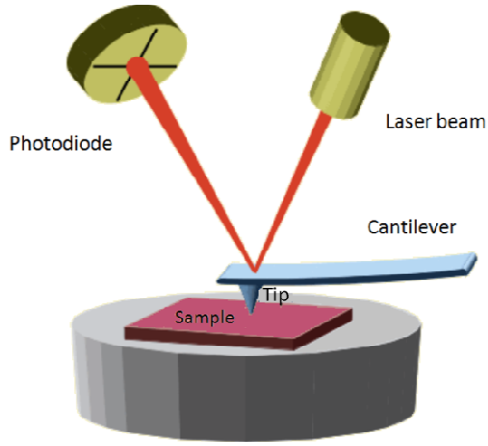

Figure 2.8. Scheme of the probe and scanning process of an AFM.

Atomic Force Microscopy was mainly used in this thesis for a topographic characterization of the arrays of nanostructures, from which we obtained their vertical and lateral dimensions in the sub-micrometric and nanometric scale. The software enables to obtain the thickness profile of the sample along any in-plane direction. Figure 2.9(a) shows an AFM image of an array of Permalloy dots and (b) shows the AFM profile of the array of dots along the blue line in (a). The y-axis in the graph corresponds to the out-of plane direction and represents the thickness of the sample. The x-axis corresponds to the in-plane direction selected by the blue line in figure 2.9(a).

Since AFM provides height information, this technique was also used in this thesis to calibrate the tooling factor of the different target materials in the thermal evaporation system. The tooling factor is a correction for the difference in material deposited on the quartz balance versus the material deposited on the substrate. The corresponding tooling factor was obtained by measuring the real thickness of the evaporated film on the substrate by AFM and related it to the thickness registered by the quartz sensor.

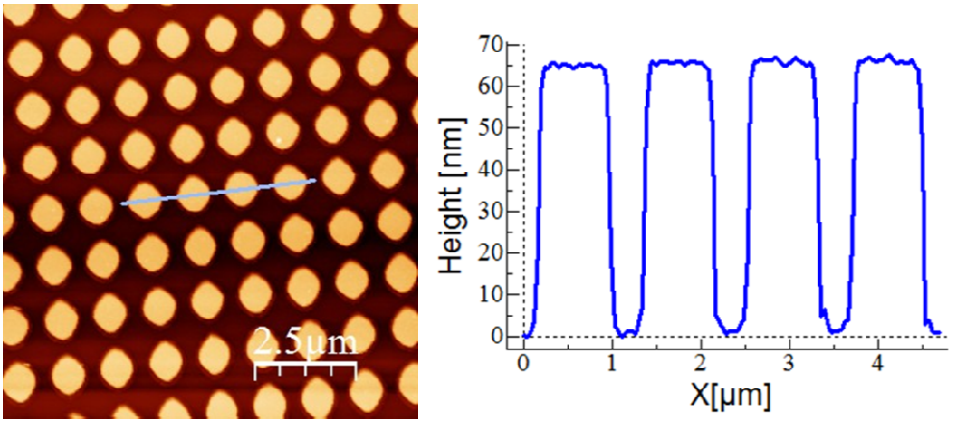

Figure 2.9. (a) AFM image of an array of Permalloy dots, (b) thickness profile along the blue line in (a).

2.6. Superconducting quantum interference device (SQUID)

Superconducting quantum interference device is one of the most sensitive techniques to magnetically characterize samples with great precision[76]. Moreover, it allows to directly determine the overall magnetic moment of a sample in absolute units.

The measurements consist basically of moving a sample through the superconducting detection coils, which are located at the center of a magnet. As the sample moves through the coils, the magnetic moment of the sample induces an electric current in the detection coils. The variations in the current in the detection coils produce corresponding variations in the SQUID output voltage, which are proportional to the magnetic moment of the sample.

The SQUID that was used in this thesis is the commercial device MPMS 3 from Quantum Design, which has a 7 T magnet, temperature control between 5 and 400 K, and a sensitivity of 10^{-8} emu.

We used SQUID magnetometry to obtain the hysteresis loops for the different types of nanostructures that we developed in this thesis. It allowed to study the different magnetic behavior when tuning the diameter and material thickness of arrays of Py and Fe disks as well as the multilayer structure of arrays of SAF's. Consequently, it enabled to adjust those morphological and structural parameters to the desired magnetic response for biological applications.

The magnetic behavior of the disks released from the wafer was also obtained by SQUID. For these measurements, a droplet of an aqueous solution of disks was dried on a Si wafer. The high sensitivity of the SQUID enabled to measure samples with a low number of dried nanostructures so that we saved and employed them for other purposes such as cell assays.

Since SQUID determines the magnetic moment of the samples with high accuracy, it was also used to study the magnetic stability of the disks after using certain chemical etchants in the fabrication process that could undesirably affect the magnetic layers. For that purpose, the magnetic moment of a sample was measured by SQUID prior and after immersing it in the chemical etchant. The magnetic stability was tested by measuring reduction in the magnetic moment, which might indicate a loss of magnetic material (e.g. due to oxidation).

2.7. Magneto-optical Kerr effect magnetometer (MOKE)

The magneto-optical Kerr effect consists of the rotation of the plane of polarization of a linearly polarized light beam after being reflected by a magnetic sample. This effect has its origin in the optical anisotropy of materials and is proportional to the magnetization of the sample.

According to the direction of the magnetization vector with respect to the reflection surface and the plane of incidence, the MOKE can be categorized

into different geometries[77]. For the characterization of the samples in this thesis, we used the longitudinal geometry (L-MOKE), in which the magnetization vector is parallel to both the reflection surface and the plane of incidence of light. In this geometry, an additional polarization component perpendicular to incoming polarization is found in the reflected beam, leading to a change in the ellipticity and a rotation of the plane of polarization, which is proportional to the in-plane magnetization component parallel to the plane of incidence.

The basic operation of MOKE magnetometers with longitudinal geometry is illustrated in the figure 2.10. An incident beam coming from a laser source is polarized and focused on a sample's surface. The sample is under an external magnetic field oriented parallel to the plane of incidence and generated by an electromagnet. The reflected beam passes through a quarter-wave plate, which removes the ellipticity of the signal, subsequently filtered by an analyzer and finally collected by a photodiode, which detects the L-MOKE component.

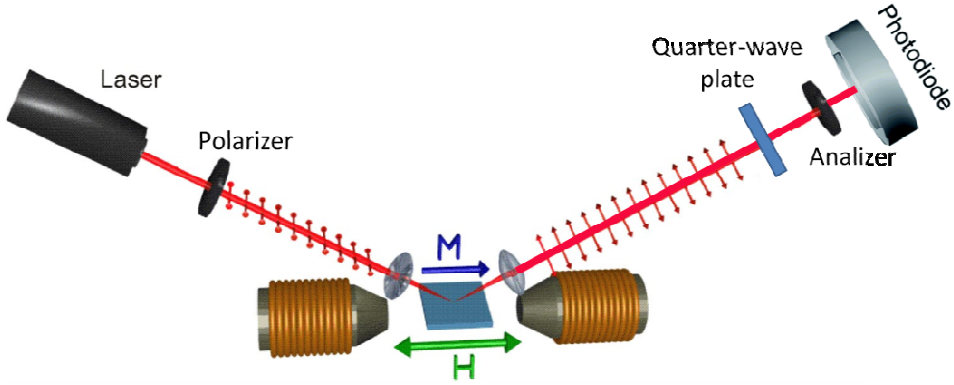

Figure 2.10. Scheme of the set-up of the longitudinal Kerr effect.

The equipment used in this thesis was the NanoMOKE2 from Oriel Group Europe. In this system, the sample is mounted on a motion stage, which enables to move the laser spot over the sample to magnetically characterize it at the desired location. The small size of the laser spot (over 3 μm) allows

to obtain the hysteresis loops from very localized sample areas. Moreover, the sample can also be rotated by the motion stage to obtain the magnetic behavior across different magnetic field directions in the plane of the sample. In this thesis, we took advantage of this versatility in the configuration of the magnetic measurements, which made it possible to check the homogeneity of the magnetic behavior of the samples at different sample locations and at different magnetic field directions.

References

[1] M. E. Walsh, "Nanostructuring magnetic thin films using interference lithography." Massachusetts Institute of Technology, 2000.

[2] I. Byun and J. Kim, "Cost-effective laser interference lithography using a 405 nm AlInGaN semiconductor laser," *J. Micromechanics Microengineering*, vol. 20, no. 5, p. 55024, 2010.

[3] M. E. Walsh, "On the design of lithographic interferometers and their application," Massachusetts Institute of Technology, 2004.

[4] H. Wolferen and L. Abelmann, "Laser interference lithography," in *Laser Interference Lithography. In Lithography: Principles, Processes and Materials*, T. H. C., Ed. Nova Science Publishers, 2011, pp. 133–148.

[5] R. Ji, "Templated Fabrication of Periodic Nanostructures Based on Laser Interference Lithography," Martin-Luther-Universität Halle-Wittenberg, 2008.

[6] S. Moralejo, F. J. Castano, C. Redondo, R. Ji, K. Nielsch, C. A. Ross, and F. Castano, "Fabrication and magnetic properties of hexagonal arrays of NiFe elongated nanomagnets," *J. Magn. Magn. Mater.*, vol. 316, no. 2, pp. e44–e47, 2007.

[7] M. Pardavi-Horvath, P. E. Si, C. A. Ross, F. J. Castaño, B. G. Ng, and S. Moralejo, "Configurational stability of patterned magnetic nanosystems," *J. Appl. Phys.*, vol. 103, no. 7, p. 07D516, 2008.

[8] C. A. Ross, M. Hwang, M. Shima, J. Y. Cheng, M. Farhoud, T. A. Savas, H. I. Smith, W. Schwarzacher, F. M. Ross, and M. Redjdal, "Micromagnetic behavior of electrodeposited cylinder arrays," *Phys. Rev. B*, vol. 65, no. 14, p. 144417, 2002.

[9] J. Jang, C. K. Ullal, M. Maldovan, T. Gorishnyy, S. Kooi, C. Koh, and E. L. Thomas, "3D Micro-and Nanostructures via Interference Lithography," *Adv. Funct. Mater.*, vol. 17, no. 16, pp. 3027–3041, 2007.

[10] "Nano Fabrication and Patterning Techniques," in *Nanotechnology-Enabled Sensors*, Boston, MA: Springer US, 2008, pp. 135–210.

[11] G. A. Condas and R. B. Yarbrough, "Permalloy Film Deposition by Flash Evaporation," *Rev. Sci. Instrum.*, vol. 42, no. 8, pp. 1168–1171, Aug. 1971.

[12] K. D. Vernon-Parry, "Scanning electron microscopy: an introduction," *III-Vs Rev.*, vol. 13, no. 4, pp. 40–44, 2000.

[13] "http://www.mee-inc.com/hamm/scanning-electron-microscopy-sem/." .

[14] "No Title." [Online]. Available: http://www3.physik.uni-greifswald.de/method/afm/eafm.htm.

[15] M. McElfresh, "Fundamentals of magnetism and magnetic measurements featuring quantum design's magnetic property measurement system," 1994.

[16] E. V Dirote, *New developments in nanotechnology research*. Nova Publishers, 2007.

Chapter 3

Fabrication of magnetic nanostructures in solution via Interference Lithography

3.1. Introduction

The fabrication processes of nanomaterials can by divided into two different approaches: "bottom-up" and "top-down". In the "bottom-up" approach all begins from small building blocks such as atoms and molecules that get assembled to form nanostructures; examples of this approach are the chemical synthesis and colloidal aggregation. By contrast, the "top down" starts from a bulk material, which is then step-by-step removed to form objects in the nanometer scale, (e.g. lithography).

Most of the nanoparticles used in biomedicine –superparamagnetic nanoparticles- have been obtained by chemical synthesis[78], [79], in which

chemical reactions form stable nuclei in solution with subsequent particle growth[80]. Although chemical routes are low-cost synthesis methods that allow high production of nanoparticles, they have important difficulties for precisely control of size, shape and composition. The polidispersity of nanoparticles can lead to different magnetic behavior and, in some cases, to the coexistence of the superparamagnetic nanoparticles with a small proportion of larger ferromagnetic nanoparticles, which can generate undesirable particle aggregation. Secondly, the superparamagnetic nanoparticles are typically iron oxides presenting low magnetic moments, which limits their efficiency.

The top-down fabrication methods, which had been originally used for patterning surfaces for microelectronics, have recently become an attractive fabrication approach of magnetic nanostructures for biomedical applications[23], [38]. The combination of lithography with physical deposition techniques has allowed the fabrication of nanostructures with good control of shape and dimensions. In addition to this, since pure magnetic materials and alloys can be deposited, nanostructures with high magnetic moments while preserving the zero remanence (i.e. vortex-state disks) can be fabricated with this approach. Besides, Ti or Au layers can be deposited to protect the nanostructures against the oxidizing power of aqueous suspensions.

Among the number of lithography techniques that have been developed, electron beam lithography is the most widely used for the fabrication of micro and submicrometric structures due to its unique advantages of high resolution in feature size and high reliability in processing[81]. However, e-beam lithography is expensive, slow, and inefficient for the patterning of large areas, which makes this technique not suited for mass production of nanostructures. By contrast, conventional photolithography has succeeded in the fabrication of magnetic microstructures with tunable properties over large areas. However, the photolithographic technique has a limitation in the element size in the micrometer range and it is crucial for biomedical

applications to scale down into the submicrometer scale. Submicrometric magnetic nanostructures can be achieved by means of alternative lithographic techniques[25], [28], [82], [83] including nanoimprint[26], [84], nanosphere[27], [85] and sparse colloidal lithography[86]. Among them, interference lithography (IL) is an excellent candidate as it enables to pattern large areas without the use of a mask or costly solid stamps allowing fabrication at a significant lower cost. Moreover, it is a versatile technique. Patterns of different sizes –few hundreds of nm in diameter and geometries –disks[87], [88], ellipses[89] and lines[90] –can be simply obtained by changing the incident angle of the laser beam and the exposure dose.

We propose a fabrication process of disk-shaped magnetic nanostructures based on IL, a cost effective technique that enables to pattern large areas (cm^2), leading to high mass production of magnetic nanostructures for biomedical assays. The set up of the equipment makes easy to tailor the shape and size of the nanoelements, from about 50 nm to a few microns, which enables to engineer nanostructures with specific magnetic properties.

Two fabrication routes were explored taking advantage of the possibility of using positive and negative resists for Interference Lithography leading to resist templates of pillars and holes, respectively. A crucial step is the subsequent release of the nanostructures into aqueous solution. In the positive resist route the nanostructures grow on top of resist pillars, so that can be released into solution directly by removing the resist in the lift-off process. However, in the negative resist route the nanostructures grow through resist holes and are in direct contact with the substrate. In this case, an additional sacrificial layer is needed between the substrate and the nanostructures that can be subsequently removed by appropriate solvents enabling the release of the nanostructures. We explored the use of two different sacrificial layers of Ge and Al. The comparison of the fabrication processes and the morphological properties of the nanostructures obtained from each route will be discussed below.

3.2. Positive resist fabrication route

The fabrication strategies based on lithography that we carried out comprise a series of additive steps including exposure and development of resist templates, thin film deposition and the lift-off process, in which the resist is removed in a solvent lifting off the material deposited on top[91]. We designed a fabrication procedure of magnetic nanostructures in solution by IL using a positive resist, which enables to release the patterned disks grown on top of the resist pillars directly from the lift-off process. The series of additive steps are explained below.

Dilution of the resist

The positive photoresist AZ MIR 701 (from Michrochemicals) was used for this fabrication strategy. According to the specifications of the manufacturer, if this resist is spin-coated on a Si wafer at 6000 rpm and baked at 90 ºC during 60 s, the final resist thickness is about 0.8 μm, which is too thick for our purpose since the aspect-ratio of the resist mask becomes too high for the fabrication of submicrometric structures. To reduce the thickness, we diluted the AZ MIR 701 with a resist solvent (AZ EBR)[92], then spin-coated the resist on a Si wafer at 6000 rpm and baked at 90 ºC. The effect of varying the volumetric dilution ratio on the final resist thickness was investigated. The thickness measurements were performed by Atomic Force Microscopy (AFM) on resist line patterns obtained by IL for various volumetric dilution ratios of solvent to resist (1- 6) (Figure 3.1). As expected, the resist thickness decreases with increasing the dilution ratio reaching 26 nm at the highest dilution ratio used in this study (6).

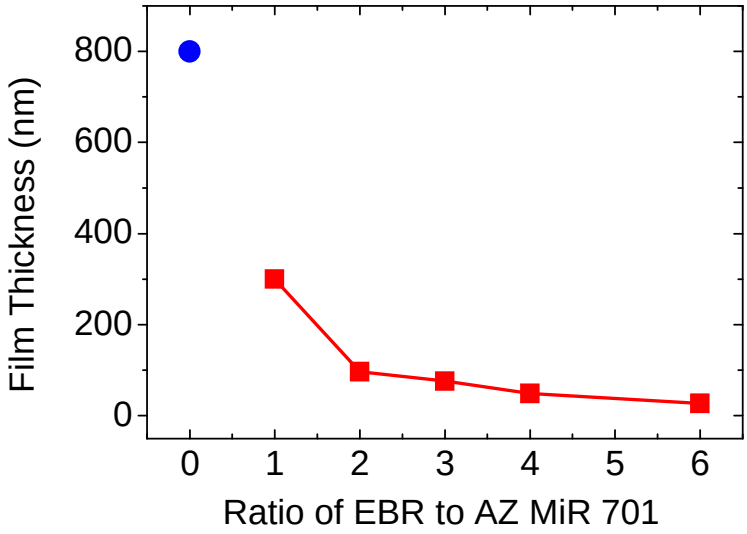

Figure 3.1. The red squares correspond to the resist thickness dependence with the volumetric ratio of the solvent EBR to the positive resist AZ MiR 701. The blue circle corresponds to the non-diluted resist film thickness provided by the manufacturer.

When choosing the volumetric dilution ratio that yielded an appropriate resist thickness for our purposes we had to consider the problem of the vertical waves, which is generally avoided by the use of a Bottom Anti-reflective Coating (BARC). However, the BARC (AZ Barli II) compatible with our positive resist AZ MIR 701 was not suitable for our process as it was not removed in the development of the resist. As an alternative, the effects of the vertical waves can be minimized by choosing a resist layer thickness quite below the period of the vertical pattern. According to equation 2 in the previous chapter, the period of the vertical pattern can be calculated as 97 nm for a 1000 nm period resist line pattern using AZ MIR 701 (n = 1.7).

We chose the resist volumetric dilution (2) yielding a resist layer thickness of 95 nm (~ 90% thinner than layer obtained from the non diluted resist),

which is slightly below the vertical pattern period but thick enough for good transference of the pattern to the magnetic material.

For such thin resist layers, the intensity of the light reflected by the substrate and the light reflected by the resist are comparable. The phase shift between both beams depends on the thickness of the material, which often varies a little over different locations on a wafer. Therefore, the dose over the sample would be not uniform. Fortunately, this problem is overcome by the application of a TARC (Top Anti-reflective Coating), which reduces the intensity reflected by the resist. We used AZ Aquatar, a compatible TARC with our resist that is easily removed in the development of the resist.

Ti buffer layer

The absence of a BARC placed between the resist and the wafer revealed poor adhesion between the resist layer and the silicon wafer (Si(100) substrate 360 μm thick covered by a SiO layer 15nm thick). To prevent from this, a titanium thin film 15 nm thick was deposited onto the Si wafer promoting the resist adhesion. (Figure 3.2. (a))

Resits spin coating

Positive photoresist AZ MIR 701 (diluted 1:2 with the resist solvent AZ EBR) was spin coated at 6000 rpm for 1 minute onto a Si/Ti wafer and baked on a hotplate at 90 °C for 60 seconds. After that, a top antireflective layer AZ Aquatar was spin coated on top of the resist layer at 3000 rpm for 60 seconds, which leads to a 70 nm TARC film. (Figure 3.2. (b))

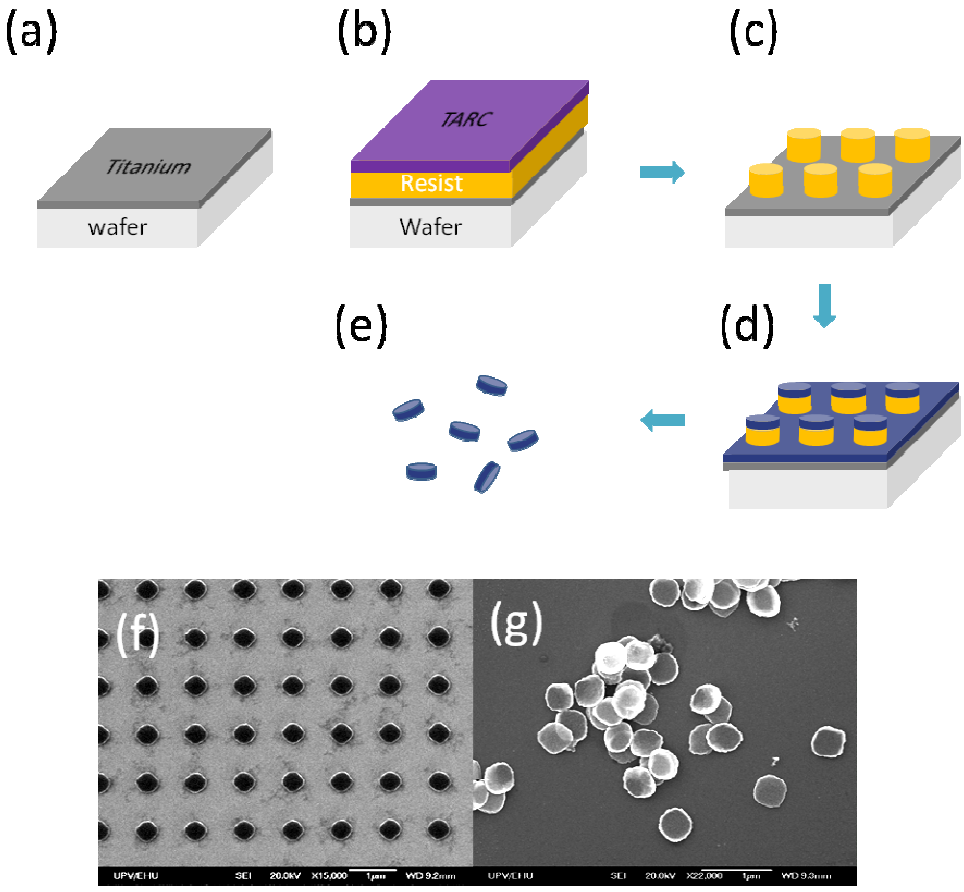

Figure 3.2. Nanodisk fabrication strategy using positive resist. (a) Deposition of a Ti layer to enhance resist adherence to the substrate, (b) Spin coating of a positive resist-tone and antireflective coating (TARC) onto a wafer, (c) Exposure and development positive resist, (d) Thermal evaporation of Py, (e) Lift-off process using NMP and detachment of the disks. SEM images of (f) array of resist pillars (black dots), (g) Released disks of 450 nm in diameter and 25 nm in thickness.

Resist exposure and development

A double exposure was carried out using the Interference Lithography system described above. The second exposure was performed with the sample rotated 90 ° with respect to the first exposure. After that, the resist was post-baked at 180 ºC for 60 seconds and developed in AZ 726 MIF for

60 seconds, then rinsed in deionized water to remove the remaining developer. We obtained arrays of resist pillars from this process (Figure 3.2. (c), (f)).

Scanning Electron Microscopy images showed the state of developed resist pillars at different exposure doses. At low doses, SEM images revealed the presence of a thin resist veil on the substrate surrounding the resist pillars (Figure 3.3. (a)), which can be reduced by increasing the exposure dose (Figure 3.3. (b)). Therefore, high doses were applied to obtain an acceptable resist pattern after development [93].

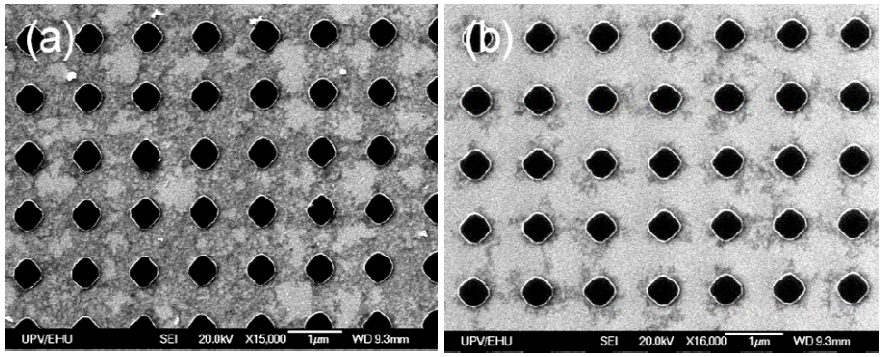

Figure 3.3. Array of resist pillars (black dots) with a periodicity of 1μm at exposure times: (a) 16 min, (b) 17 min.

Magnetic thin film deposition and detachment

The magnetic thin film was deposited on the resist pattern by thermal evaporation with base pressure of over 10^{-7} mbar (Figure 3.2. (d)). Then, the magnetic disks deposited on the top of the resist pillars were released into solution by removing the resist in a lift off process using 1-methyl-2-pyrrolidonine (NMP) at 125 °C for a few minutes followed by ultrasonic bath. (Figure 3.2. (e), (g).

In order to illustrate the process, a SEM image was taken on the substrate

when the lift-off was not fully completed (Figure 3.4.). The white dots correspond to the disks that were still on top of the resist pillars and the dark dots correspond to the holes on the substrate that the resist pillars left

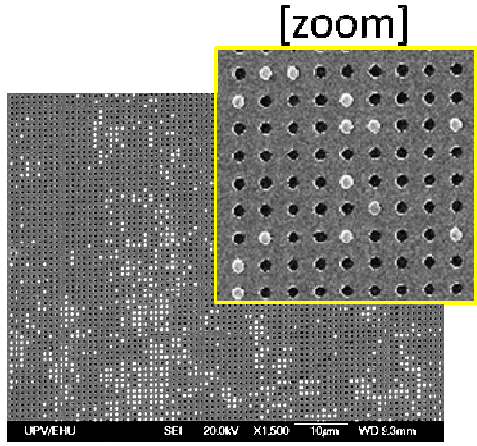

Figure. 3.4. Array after lift-off not fully completed

after being removed by the solvent. By increasing the time of the lift-off process the majority of disks were released into solution and an array of antitdots of magnetic material remained on the substrate.

An AFM image of the remaining array of antidots on the substrate is shown in Figure 3.5. (a). The problem of the resist veil discussed in the previous section lied on the possibility of lifting-off the magnetic material deposited on top, which would be released into solution along with the magnetic disks. The AFM image revealed that the lift-off process worked successfully as the only areas that have been detached from the wafer are the disks.

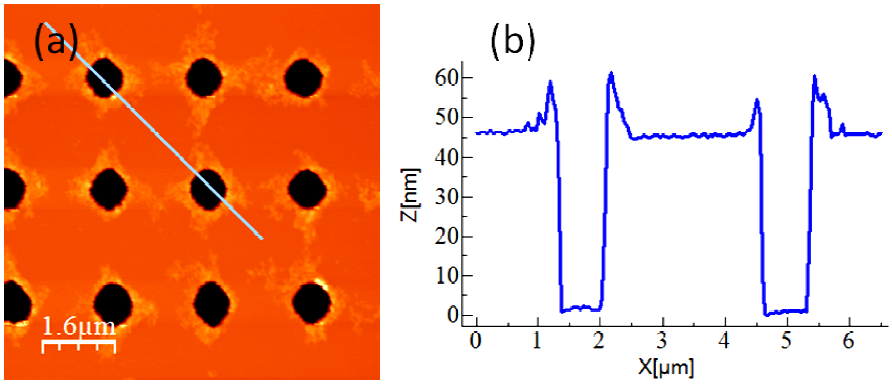

Figure 3.5. (a) AFM image of the remaining array of Py antidots with a periodicity of 2 µm on the substrate, (b) depth profile of the array along the blue line.

3.3. Negative Resist fabrication route

In the positive resist route that we explained above, the magnetic disks grow on top of the resist pillars and are released into solution directly from the lift-off process. By contrast, when using a negative resist, we fabricate arrays of resist antidots (holes) so the magnetic disks grow on the substrate and remain attached to it after the lift-off process. Therefore, to be able to detach the magnetic nanostructures from the wafer, a sacrificial layer must be placed between the Si wafer and the resist coating.

The sacrificial layer must be insoluble to the resist stripper used in the lift-off process. Otherwise the magnetic material grown on top of the resist would be released into solution and mixed with the magnetic disks grown on the sacrificial layer. We considered the possibility of using a second resist as a release layer but this option was rejected since most of the resists are solved in NMP (our resist stripper). Moreover, a translucent etchant for the sacrificial layer is desirable for further manipulation of the magnetic disks. For that purpose, we explored the use of Germanium and Aluminum thin films as release layers, which are etched with Hydrogen Peroxide and Potassium Hydroxide aqueous solutions, respectively.

3.3.1. Fabrication process using a Germanium release layer

We designed a fabrication process using a negative resist for Interference Lithography and a Germanium film as sacrificial layer, which can be etched by the use of an aqueous solution of Hydrogen Peroxide (H_2O_2). The fabrication process includes several steps that are explained below.

Ge layer deposition

A germanium thin film 23 nm thick was deposited by thermal evaporation onto the Si(100) wafer 360 μm thick covered by a SiO. (Figure 3.6. (a))

Spin coating

The antireflective coating WIDE-8B (from Brewer Science) was spin coated onto the Si/Ge wafer at 5000 rpm for 60 seconds and baked on a hotplate in two steps: 40 seconds at 100 ºC and 60 seconds at 180 ºC. Later, the negative resist tone TSMR-IN027 (from Ohka) was spin coated on the ARC coating at 4000 rpm for 60 seconds followed by a baking step at 90 ºC for 90 seconds leading to a 280 nm resist stack. (Figure 3.6. (b))

Exposure and development

A double exposure by the 90 ° rotation of the sample after the first exposure was carried out using the Interference Lithography system described above. The exposed resist was post- backed at 110 ºC for 90 seconds and developed in AZ 736 MIF leading to a resist antidot array (Figure 3.6. (c), (g)). The whole resist stack (ARC + Resist) behaves in the same way in the development. In this way, the holes are drilled through both the resist and the ARC. The periodicity of the array is set by adjusting the angle of interference θ, which was described in equation (2.1).

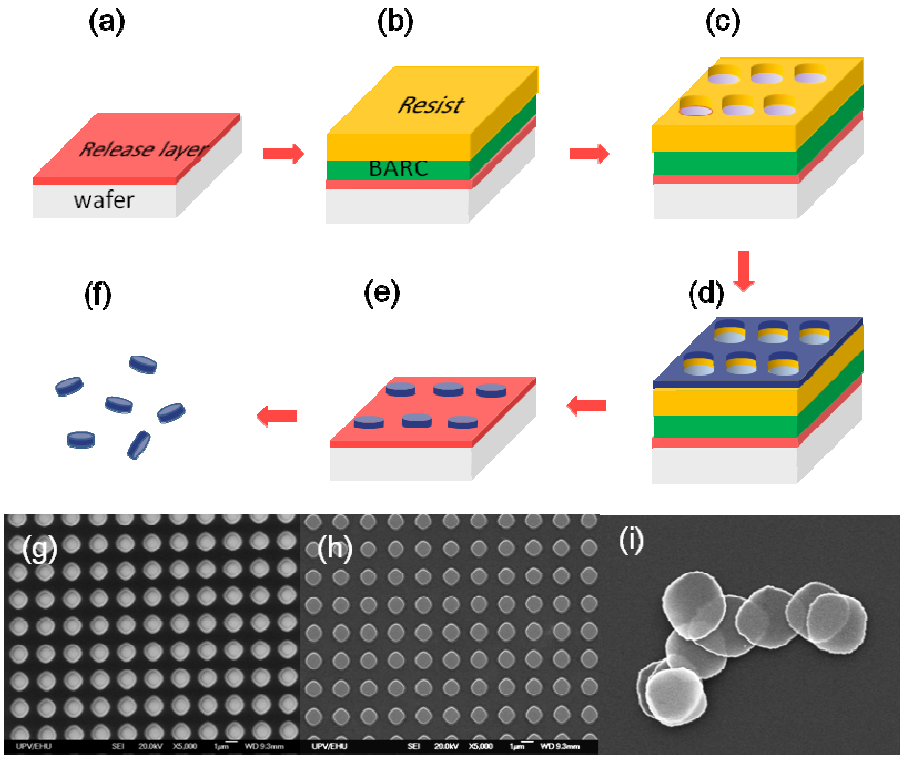

Figure 3.6. Nanodisk fabrication process using negative resist. (a) Thermal deposition of a Ge layer 23 nm thick on a Si wafer, (b) Spin coating of ARC and negative resist-tone onto the wafer, (c) Development of the negative-tone resist, (d) Thermal evaporation of the magnetic material, (e) Lift-off process, (f) Chemical etching with Hydrogen Peroxide and release of the disks. SEM images of (g) array of resist antidots, (h) array of magnetic material dots after lift-off, (i) released disks dried on a Si substrate.

Magnetic film deposition and lift-off

A magnetic layer was deposited on the antidot pattern by thermal evaporation (Figure 3.6. (d)). Then, the resist was removed in a lift-off process with NMP at 125 °C for a few minutes followed by ultrasonic bath yielding an array of magnetic disks on the Ge layer (Figure 3.6. (e), (h)).

The lift-off process was repeated as many times as necessary until all the resist was removed. The Figure 3.7. (a) shows a magnetic material dot array after lift-off, in which there was still resist left surrounding the dots. By repeating the lift-off process we succeeded in removing all the resist (Figure 3.7 (b))

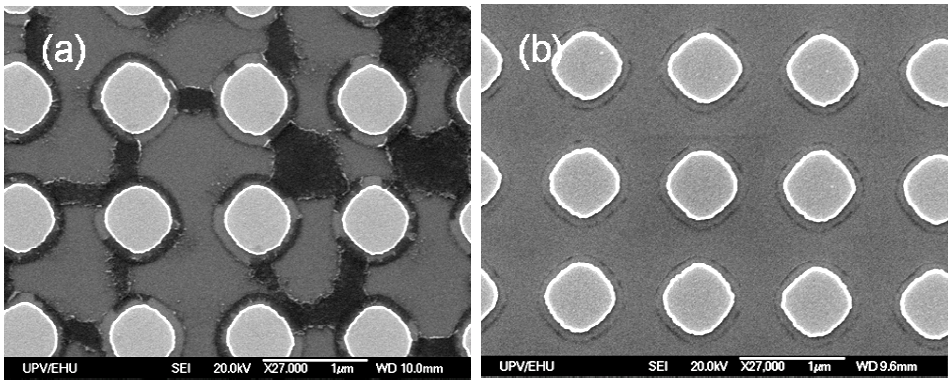

Figure 3.7. Permalloy ($Ni_{80}Fe_{20}$) dot patterns after lift-off: (a) The lift-off process was not long enough to remove all the resist. (b) The lift-off process was performed successfully.

Detachment

Finally, the magnetic disks were released into solution (Figure 3.6. (f), (i)) by etching the Ge layer with an aqueous hydrogen peroxide solution. The mechanism by which the aqueous hydrogen peroxide solution etches the Ge has to do with the fact that aqueous solution oxidizes the Ge layer and the oxide of Ge is soluble in water[94]. Since the fabrication strategy includes the use of a metal etchant (Hydrogen Peroxide), the magnetic layer must be protected. For that purpose a Ti layer was deposited prior and after the magnetic layer. Consequently, both sides of the disks were covered by Ti preventing to a certain extent from oxidation. The concentration conditions of the etching process were chosen to minimize the oxidation of the magnetic disks as it will be discussed in the next chapter.

3.3.2. Fabrication process using Aluminum as release layer

We developed a fabrication strategy including the use of Aluminum as release layer, which can be etched by immersing the sample in an aqueous solution of potassium hydroxide (KOH)[95]. We also explored the possibility of growing the release layer after the development of the resist so the pattern is also transferred to the deposit of the release layer. The steps of the fabrication process are explained below.

Spin coating

In this case, the antireflective coating WIDE-8B (from Brewer Science) and the negative resist tone TSMR-IN027 (from Ohka) were spin coated directly onto the Si wafer (Fig 3.8. (a), (b)) following the coating recipe explained before for the alternative negative resist fabrication process that used Ge as release layer.

Exposure and development

The BARC/resist stack was exposed by the 90 ° rotation of the sample after the first exposure using the Interference Lithography system. After exposure, the sample was post- backed at 110 °C for 90 seconds and developed in AZ 736 MIF giving rise to a resist antidot array on a Si wafer (Figure 3.8. (c), (g)).

Al release layer, magnetic film deposition and lift-off

An Aluminum layer 23 nm thick was deposited on the samples by thermal evaporation. Then, the magnetic material was deposited on top of the Al layer using the same evaporation technique (Figure 3.8. (d)). After that, the resist was removed in a lift-off process with NMP at 125 °C for a few minutes followed by ultrasonic bath. In this way, the sacrificial layer made of Aluminum is also patterned in form of a sacrificial disk placed

underneath the magnetic disks (Figure 3.8. (e), (h)).

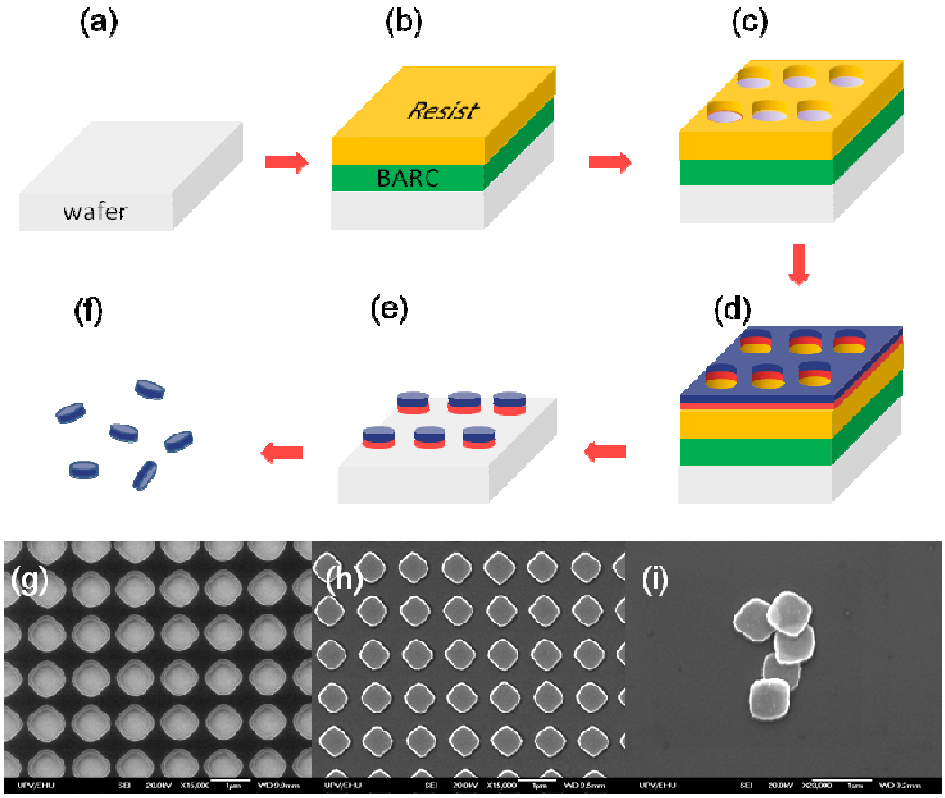

Figure 3.8. Nanodisk fabrication process using negative resist and Al as release layer. (a) Start from a Si waver, (b) Spin coating of ARC and negative resist-tone onto the wafer, (c) Development of the resist, (d) Thermal evaporation of the Al layer 23 nm thick and the magnetic material, (e) Lift-off process, (f) Chemical etching with KOH(15%) and release of the disks, SEM images of (g) array of resist antidots, (h) array of magnetic material dots after lift-off, (i) released disks dried on a Si substrate.

Detachment

The magnetic disks were released from the wafer by immersing the samples in an aqueous KOH (15%) solution in an ultrasonic bath (Figure 3.8. (f), (i)).

Since KOH is also a silicon oxide etchant[95], the naked silicon surrounding the disks was also chemically attacked in this process. This is shown in a SEM image that was taken of the substrate after the KOH etching (Figure 3.9.). We can differentiate three parts in the image: the bright dots, which are three magnetic disks detached from its position in the array but after drying the sample they remained on the substrate, the array of dark dots corresponding to the original position of the magnetic disks before being released into solution and finally the grey part surrounding the dark dots, which is the naked Silicon that was also attacked in the detachment process.

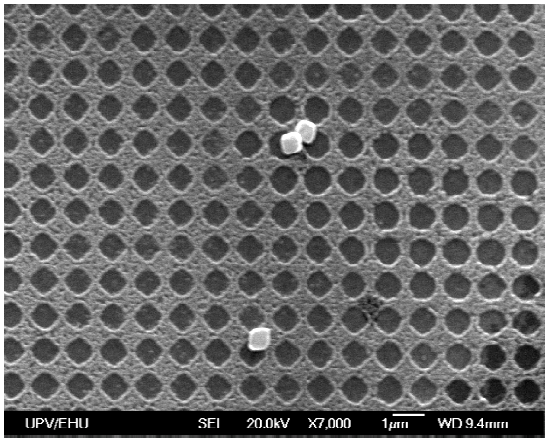

Figure 3.9. Substrate of Silicon after the detachment process using a KOH aqueous solution (15%).

3.4. Comparison of the two fabrication routes

The alternative fabrication routes of magnetic nanostructures presented above consisted of a series of additive steps, some of which displayed different characteristics. In this section, a comparative study of the designed fabrication strategies was carried out to clarify the strengths and limitations of each route.

Regarding the duration of the process, the fabrication route using the positive resist comprises fewer steps than the route based on the negative resist as no sacrificial layer is needed for the detachment of the disks. Anyhow, the number of steps is not the only difference between our fabrication strategies. Actually, the discrepancies in some of the additive steps have an effect on the properties of the nanostructures.

Figure 3.10. shows microscopy images at different stages of the two fabrication routes. In case of positive resist, 25 nm of the magnetic material were grown on resist pillars (Figure 3.10. (a)). The AFM scan reveals a curved profile of the top side of the pillars (Figure 3.10. (b)). This profile yields concave nanodisks when released, as observed by SEM on dried MNS (Figure 3.10. (c)). Bended nanostructures are the result of a Permalloy deposit on a top-curved positive resist pillars. However, the MNS thickness seems quite uniform on the lateral dimensions of the nanostructure.

By contrast, no curvature was observed on the disks fabricated by the negative resist route. Figure 3.10. (d) shows the AFM image of Permalloy disks attached to the substrate, fabricated from the negative resist route. Figure 3.10. (e) shows the AFM profile of a single Permalloy disk with 50 nm of height coated by around 10 nm of Ti on both sides. Released MNS from the negative resist route present a much flatter surface than those from the positive resist (Figure 3.10. (f)). The lack of curvature following this route is reasonable since in this case the Permalloy layer was grown onto a flat Si/Ge wafer.

Flat disks are desirable for having a better control of the magnetic properties, which strongly depend on the nanostructure geometry. Consequently, the negative resist route is more suitable for the fabrication of nanodisks with more complex magnetic configurations such as synthetic antiferromagnetic nanostructures (SAF) in which the role of the interfaces is crucial [14], [84].

Another advantage of the negative resist route is that it enables to

magnetically characterize the square array of magnetic disks before being released into solution. This is due to the fact that the array of magnetic disks is placed on a non-magnetic layer (Ge or Al) and represents the only magnetic contribution to the total signal. By contrast, the disks obtained from the positive resist route can be only characterized once they are released into solution. Before detachment, the array of magnetic dots deposited on top of the resist pillars coexist with the magnetic layer deposited onto the Si/Ti wafer giving rise to an additional contribution to the total signal.

Further discussion of the magnetic measurements and the comparison of the magnetic properties of the nanostructures obtained from the different routes will be discussed in the next chapter.

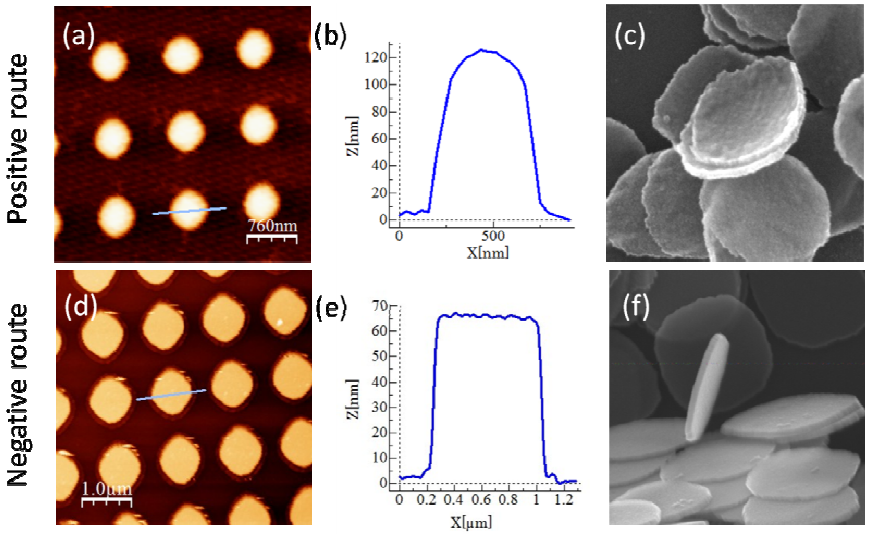

Figure 3.10. Morphological characterization of Permalloy disks obtained from the positive and negative resist route. Disks from the positive resist route: (a) AFM image after thermal evaporation of Permalloy on top of resist pillars, (b) AFM profile along the blue line in (a), (c) SEM image of nanodisks after lift-off of the resist. Disks from negative resist route: (d) AFM image after Permalloy deposition and lift-off of the resist, (e) AFM profile along the blue line in (d), (f) SEM image of nanodisks after etching of the sacrificial layer.

3.5. Conclusions

We presented two different routes to fabricate biocompatible magnetic nanostructures in solution. Both routes provide a cost-effective, versatile and high throughput method to design functional magnetic elements at the sub-micrometer scale. Interference lithography with positive resist requires fewer steps but has the disadvantages of poor adhesion to Si wafers and production of curved nanostructures. On the contrary, a negative resist route allows a complete magnetic characterization and flat nanostructures.

Flat disks are desirable for having a better control of the magnetic properties, which strongly depend on the nanostructure geometry. Consequently, the negative resist route is more suitable for the fabrication of nanodisks with more complex magnetic configurations such as synthetic antiferromagnetic nanostructures (SAF) in which the role of the interfaces is crucial.

References

[1] S. F Hasany, N. H Abdurahman, A. R Sunarti, and R. Jose, "Magnetic iron oxide nanoparticles: chemical synthesis and applications review," *Curr. Nanosci.*, vol. 9, no. 5, pp. 561–575, 2013.

[2] C. Grüttner, K. Müller, J. Teller, and F. Westphal, "Synthesis and functionalisation of magnetic nanoparticles for hyperthermia applications," *Int. J. Hyperth.*, vol. 29, no. 8, pp. 777–789, 2013.

[3] N. Poudyal, "Fabrication of superparamagnetic and ferromagnetic nanoparticles," The University of Texas at Arlington, 2008.

[4] D.-H. Kim, E. A. Rozhkova, I. V Ulasov, S. D. Bader, T. Rajh, M. S. Lesniak, and V. Novosad, "Biofunctionalized magnetic-vortex microdiscs for targeted cancer-cell destruction," *Nat. Mater.*, vol. 9, no. 2, pp. 165–171, 2010.

[5] S. Leulmi, X. Chauchet, M. Morcrette, G. Ortiz, H. Joisten, P. Sabon, T. Livache, Y. Hou, M. Carrière, and S. Lequien, "Triggering the apoptosis of targeted human renal cancer cells by the vibration of anisotropic magnetic particles attached to the cell membrane," *Nanoscale*, vol. 7, no. 38, pp. 15904–15914, 2015.

[6] Y. Chen, "Nanofabrication by electron beam lithography and its applications: A review," *Microelectron. Eng.*, vol. 135, pp. 57–72, 2015.

[7] A. O. Adeyeye and N. Singh, "Large area patterned magnetic nanostructures," *J. Phys. D. Appl. Phys.*, vol. 41, no. 15, p. 153001, 2008.

[8] C. A. Ross, M. Hwang, M. Shima, J. Y. Cheng, M. Farhoud, T. A. Savas, H. I. Smith, W. Schwarzacher, F. M. Ross, and M. Redjdal, "Micromagnetic behavior of electrodeposited cylinder arrays," *Phys. Rev. B*, vol. 65, no. 14, p. 144417, 2002.

[9] W. Hu, M. Zhang, R. J. Wilson, A. L. Koh, J.-S. Wi, M. Tang, R. Sinclair, and S. X. Wang, "Fabrication of planar, layered nanoparticles

using tri-layer resist templates," *Nanotechnology*, vol. 22, no. 18, p. 185302, 2011.

[10] Y. Luo and V. Misra, "Large-area long-range ordered anisotropic magnetic nanostructure fabrication by photolithography," *Nanotechnology*, vol. 17, no. 19, p. 4909, 2006.

[11] L. J. Guo, "Nanoimprint lithography: methods and material requirements," *Adv. Mater.*, vol. 19, no. 4, pp. 495–513, 2007.

[12] W. Hu, R. J. Wilson, A. Koh, A. Fu, A. Z. Faranesh, C. M. Earhart, S. J. Osterfeld, S. Han, L. Xu, and S. Guccione, "High-Moment Antiferromagnetic Nanoparticles with Tunable Magnetic Properties," *Adv. Mater.*, vol. 20, no. 8, pp. 1479–1483, 2008.

[13] C. L. Cheung, R. J. Nikolić, C. E. Reinhardt, and T. F. Wang, "Fabrication of nanopillars by nanosphere lithography," *Nanotechnology*, vol. 17, no. 5, p. 1339, 2006.

[14] P. Tiberto, G. Barrera, F. Celegato, G. Conta, M. Coïsson, F. Vinai, and F. Albertini, "Ni80Fe20 nanodisks by nanosphere lithography for biomedical applications," *J. Appl. Phys.*, vol. 117, no. 17, p. 17B304, 2015.

[15] M. Goiriena-Goikoetxea, A. García-Arribas, M. Rouco, A. V Svalov, and J. M. Barandiaran, "High-yield fabrication of 60 nm Permalloy nanodiscs in well-defined magnetic vortex state for biomedical applications," *Nanotechnology*, vol. 27, no. 17, p. 175302, 2016.

[16] C. A. et al Ross, S. Haratani, F. J. Castano, Y. Hao, M. Hwang, M. Shima, J. Y. Cheng, B. Vögeli, M. Farhoud, and M. Walsh, "Magnetic behavior of lithographically patterned particle arrays," *J. Appl. Phys.*, vol. 91, no. 10, pp. 6848–6853, 2002.

[17] M. Thielen, S. Kirsch, H. Weinforth, A. Carl, and E. F. Wassermann, "Magnetization reversal in nanostructured Co/Pt multilayer dots and films," *IEEE Trans. Magn.*, vol. 34, no. 4, pp. 1009–1011, 1998.

[18] Y. Hao, M. Walsh, M. Farhoud, C. A. Ross, H. I. Smith, J. Q. Wang,

and L. Malkinski, “In-plane anisotropy in arrays of magnetic ellipses,” *IEEE Trans. Magn.*, vol. 36, no. 5, pp. 2996–2998, 2000.

[19] A. G. Flores, V. Raposo, J. Iñiguez, M. Zazo, C. Redondo, and D. Navas, “Anisotropy Field in Ni Nanostripe Arrays,” *IEEE Trans. Magn.*, vol. 49, no. 1, pp. 15–17, 2013.

[20] M. J. Madou, *Fundamentals of microfabrication: the science of miniaturization*. CRC press, 2002.

[21] J. H. J. Chai, “Combining Zinc Oxide and Silver for Potential Optoelectronic Applications,” University of Canterbury. Electrical and Computer Engineering, 2010.

[22] R. Murillo, H. A. Van Wolferen, L. Abelmann, and J. C. Lodder, “Fabrication of patterned magnetic nanodots by laser interference lithography,” *Microelectron. Eng.*, vol. 78, pp. 260–265, 2005.

[23] K. R. Williams, K. Gupta, and M. Wasilik, “Etch rates for micromachining processing-Part II,” *J. microelectromechanical Syst.*, vol. 12, no. 6, pp. 761–778, 2003.

[24] K. Biswas and S. Kal, “Etch characteristics of KOH, TMAH and dual doped TMAH for bulk micromachining of silicon,” *Microelectronics J.*, vol. 37, no. 6, pp. 519–525, 2006.

[25] T. Vemulkar, R. Mansell, D. Petit, R. P. Cowburn, and M. S. Lesniak, “Highly tunable perpendicularly magnetized synthetic antiferromagnets for biotechnology applications,” *Appl. Phys. Lett.*, vol. 107, no. 1, p. 12403, 2015.

Chapter 4

Permalloy nanodisks: vortex-state

4.1. Introduction

Although ferromagnetic materials generally form domains to reduce their magnetostatic energy, in submicrometric ferromagnetic systems the formation of domain walls is not energetically favorable. Specifically, in submicrometric disk-shaped ferromagnetic structures with weak magnetocristaline anisotropy the remanent spin distribution is determined by the disk aspect ratio (thickness/diameter) and the magnetic exchange length $l_x = \sqrt{C/M_S}^2$ that corresponds to the disk magnetic material, where C is the magnetic exchange stiffness constant and M_S the saturation magnetization[41].

Three types of magnetic configurations are generally favored for soft submicrometric disks instead of domains (Figure 4.1.): a single domain in-plane state, a single domain out-of-plane state and a curling spin

configuration –the vortex state-[43]. Small disks (sub-100nm) with a low aspect ratio generally form single-domain in-plane states while nanodisks with a high aspect ratio form single-domain out-of-plane states. Larger disks with an intermediate aspect ratio and diameters several times larger than the magnetic exchange length form spin vortex states[42].

The vortex state can be a ground state down to the sub-100 range as we can see in the phase diagram of figure 4.1. and its presence extends to larger disks with diameters in the submicrometric range and thicknesses of ten's of nanometers.

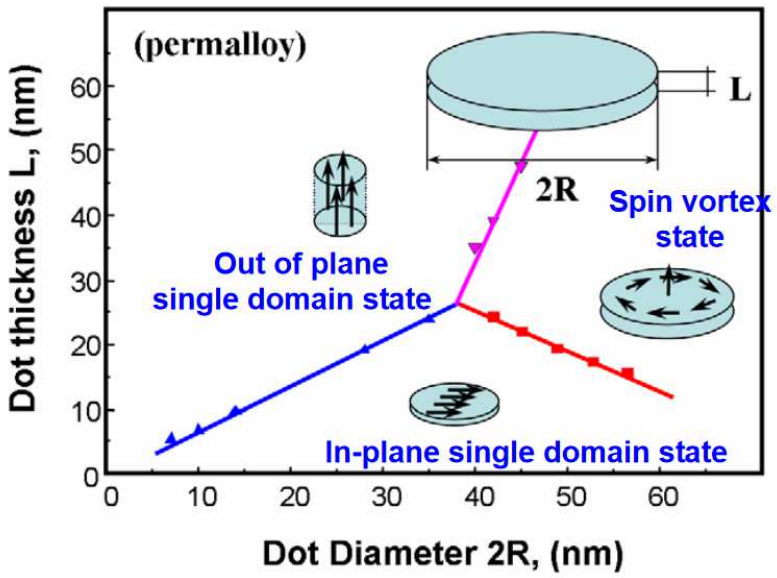

Figure 4.1. Phase diagram for Permalloy disks showing the boundaries between three ground states: out of plane single domain state, in-plane single domain state and spin vortex state. Adapted from [23].

The vortex state consists essentially on an in-plane spin flux-closure arrangement at remanence, i.e. in the absence of external magnetic field. When the disk thickness becomes much smaller than the disk diameter, the spins tend to align in the plane of the disk. In the remanent state of the

vortex-state configuration, the spin directions change gradually in the plane of the disk following the disk geometry so as not to lose too much exchange energy, but to cancel the total dipole energy[96]. Therefore, the spins basically cancel each other resulting in a zero net magnetization in absence of external magnetic field.

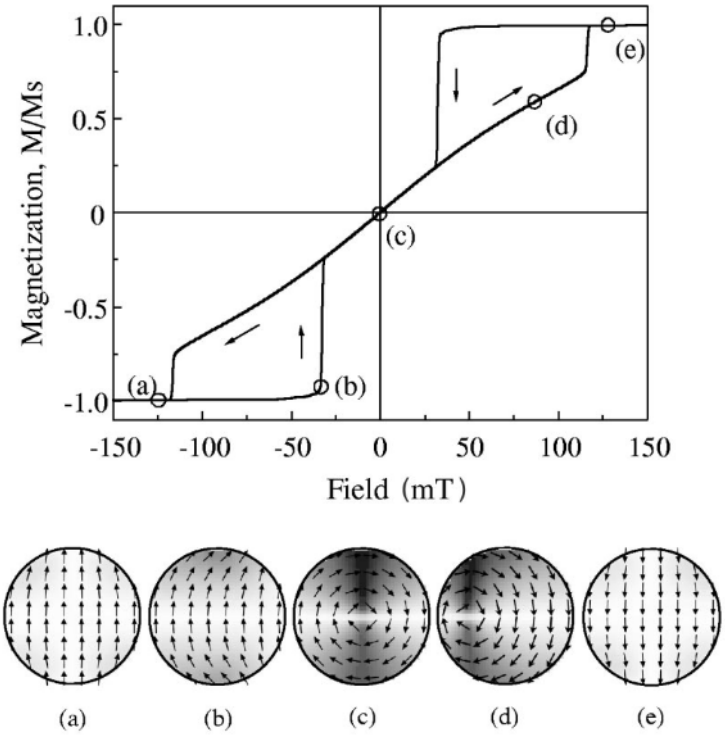

Figure 4.2. Typical hysteresis loop of a vortex state disk. When the magnetic field is reduced from saturation (a), the vortex nucleates at the nucleation field H_n (b), then displaces perpendicular to the applied magnetic field (c) and (d), and finally vanishes at the annihilation field H_{ann}. A single domain structure is present in the disk at saturation (e). Adapted from [41].

The typical hysteresis loop and the magnetization reversal process that characterize the vortex state configuration is shown in figure. 4.2.[41]. When the magnetic field is decreased from saturation (Figure 4.2. (a)), the

magnetization experiments an abrupt decrease at the nucleation field (H_n) that corresponds to the nucleation of the vortex, (Figure 4.2. (b)). At zero magnetic field, the vortex is located at the center of the disk (Figure 4.2. (c)). The linear part of the hysteresis loop corresponds to the vortex core movement from center of the disk perpendicular to the applied magnetic field (Figure 4.2. (d)). In the increasing branch of the loop, the magnetization increases with the magnetic field until saturation accompanied by a jump in the magnetization at the annihilation field (H_{ann}) in which the vortex vanishes completely. At saturation, a single domain structure is realized in the disk (Figure 4.2. (e)).

Spin vortex configuration has been obtained even when the geometric shape is different from circular, i.e., in the case of square[97]–[99] or elliptical elements[49], [100]–[102]. The presence of a magnetic vortex is either deduced from the shape of the hysteresis loops[40], [48] or is directly observed by magnetic imaging techniques such as magnetic force microscopy MFM[54], [96], [103] and Lorentz transmission electron microscopy LTEM[104], [105].

The first observation of a magnetic vortex core was reported by T. Shinjo et al on circular dots of Permalloy ($Ni_{80}Fe_{20}$) 0.3 to 1 micrometer in diameter and 50 nanometers thick[106]. A tiny "white" or "dark" spot was observed at the center of the disk, being the signature of the vortex configuration. At the core of the vortex structure, the magnetization within a small spot turns out-of- plane and parallel to the plane normal due to the increasing angle of the spins when approaching to the center of the disk. The polarity of the vortex evidenced as a "white" or "dark" spot by MFM describes the magnetization direction at the center of the vortex, either into or out of the surface plane.

Although the vortex-state configuration has been widely investigated for potential data storage by switching the core polarity, a novel application of vortex state microdisks was proposed by Kim et.al for the destruction of cancer cells opening up a new scenario for the development of promising

cancer therapies[23]. These vortex state nanostructures are interesting in biological applications as they exhibit zero magnetization in absence of external magnetic field and rotate when an alternating magnetic field is applied. Therefore, they show a great potential as magneto-mechanical actuators for cancer cell destruction and mechano-transduction stimulants.

In this chapter we present the magnetic characterization of vortex-state nanodisks of Permalloy fabricated by interference lithography (IL) through the two alternative strategies described in chapter 3: the positive and negative resist routes. The magnetic properties of the disks attached to the substrate and then released into solution are discussed below.

4.2. Preparation

Resist patterns with periodicities of 1 μm and 2 μm were fabricated by either positive or negative fabrication routes by adjusting the interference angle in our IL system. A Permalloy layer was deposited on the resist templates by thermal evaporation at a deposition rate of 4 nm/min in a vacuum chamber with base pressure of 10^{-7} mbar. A Ti layer 5 nm thick was thermally evaporated at a rate of 1 nm/min prior and after the Py layer to prevent disks from oxidation. The remaining steps including the lift-off and release process were performed as described in chapter 3 for the positive and negative resist fabrication routes. The dimensions and diameters of the disks obtained from each route are summarized in table 4.1.

As we can notice, there is significant difference in size between the Py disks fabricated by the positive and the negative resist route with analogous periodicities of 1 and 2 μm. This is due to the fact that the positive resist required high exposure doses (supra-exposures)[93] in the lithographic step for a good performance of the resist patterns. The higher the dose the smaller the resist dot size for certain periodicity of the pattern.

	Array periodicity (μm)	Disk diameter (nm)	Disk thickness (nm)
Positive-resist route	1	450	25
	2	750	50
Negative-resist route	1	650	50
	2	1180	50

Table 4.1. Dimension parameters of disks obtained from the positive and negative resist routes.

4.3. Magnetic characterization of the Py disks

4.3.1. Disks obtained from the negative resist route

One of the main advantages of the negative resist route is that it enables to magnetically characterize the disk patterns before being released into solution. After removing the resist in the lift-off process, the Permalloy disks remain on a non magnetic material (the release layer) so the disk pattern represents the only magnetic contribution of the sample.

The magnetic characterization of the Permalloy disk patterns grown on the release layer was carried out by Magneto-Optical Kerr Effect (MOKE) at room temperature. The two samples fabricated by the negative route, whose dimensions appear in table 4.1., were measured by MOKE with the applied field parallel to the sample. The shape of the measured hysteresis loops correspond to the spin-vortex configuration for the two disk sizes (Figure 4.3. (a) and 4.3. (c)).

When comparing the hysteresis loops in figures 4.3. (a) and 4.3. (c) we observed that the nucleation field, the annihilation field and the initial susceptibility are different for the dot arrays of different diameters. In the sample of disks of 650 nm in diameter the nucleation and annihilation occur

at -225 and 700 Oe, respectively. Lower nucleation and annihilation fields appear for the sample of disks with 1180 nm of diameter: -150 and 310 Oe, respectively. Another characteristic that varies with the size of the nanostructures is the initial susceptibility, which is the linear part of the hysteresis loop at low magnetic fields.

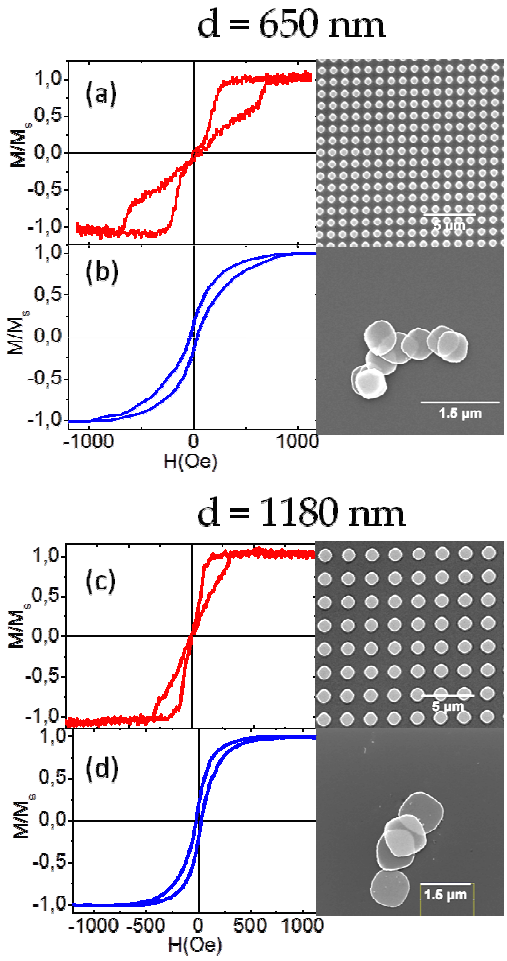

Figure 4.3. (a), (c) Magnetic characterization and SEM images of arrays of disks obtained from the negative resist route with periodicities of 1 µm and 2 µm and diameters of 650 nm and 1180 nm, respectively and (b), (d) magnetic response and SEM images of the released disks with the same dimensions, which were subsequently dried on a silicon substrate.

As we can observe in figures 4.3. (a) and 4.3. (c), the initial susceptibility is higher for the array of disks with diameter of 1180 nm. This is in good agreement with the size dependent annihilation and nucleation fields and the initial susceptibility tendency that was experimentally and theoretically reported in previous studies[45]. Guslienko et al demonstrated that by increasing dot diameter of Permalloy disks the nucleation and annihilation fields decrease, whereas the initial susceptibility increases[44]. Initial susceptibility is an indicator of the sensitivity of magnetization to changes in the external magnetic field in the linear regime of vortex-state hysteresis loops. Regarding the application of vortex-state disks in magneto-mechanic cell destruction, high initial susceptibility would be advantageous as it allows the exertion of higher torques at moderate external fields.

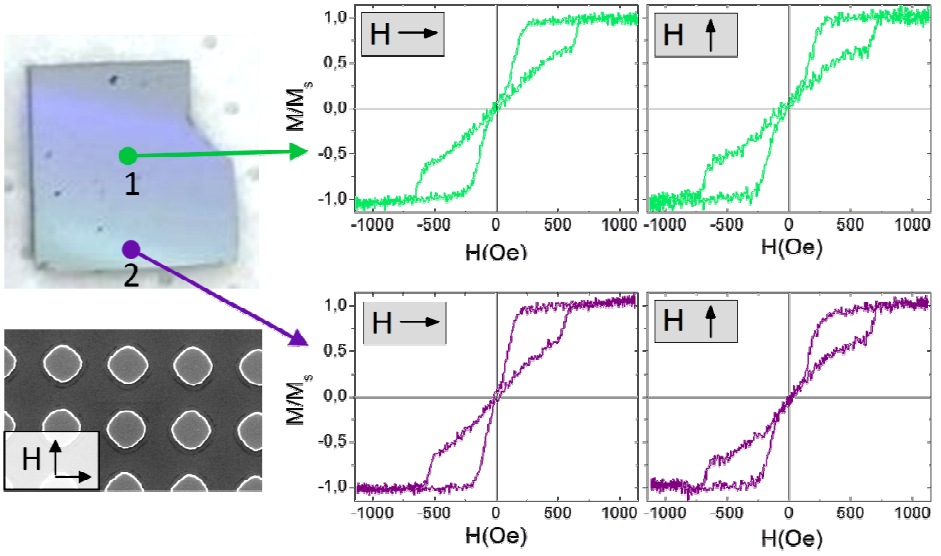

Figure 4.4. Magnetic characterization by MOKE at the center of the sample (1) and at the border (2), which are separated by 0.5 cm. The magnetic field H was applied parallel to the surface of the sample at orthogonal directions.

The characterization by MOKE not only allowed us to obtain hysteresis loops at short times but also enables to move the spot over the surface sample to obtain hysteresis loops at different locations and even rotate the sample for setting the direction of the applied magnetic field. This made it possible to check the homogeneity of the magnetic behavior over the different parts of the sample. Figure 4.4. shows the hysteresis loops obtained at two points of the sample separated by 0.5 cm: the center of the sample (point 1) and at the border (point 2), in which the magnetic field H was applied in the plane of the sample at orthogonal directions as it is indicated in the figure. The measured hysteresis loops have substantially the same shape in all conditions corresponding to the spin vortex configuration. The small discrepancies in the nucleation and annihilation fields in point 2 are related to little distortion of the shape of the Py disks in the border of the sample originated from the lithographic step. The point 2 corresponds to the part of the sample that was located farthest from the mirror, according to our IL system described in chapter 2. We have observed that at distances from the mirror close to the limit of the IL exposure area, there might be distortion on the shape of the dots showing certain elongation in one axis and constriction in the orthogonal axis. We minimized these undesirable effects by adapting the size of the sample areas quite lower than the limit of the exposure area.

The magnetic characterization of released magnetic disks was carried out by SQUID at room temperature. After the release process, the disks were washed and dispersed in deionized water. The preparation of the sample consisted on drying a droplet of the disks water suspension on a Si wafer. The magnetic response and corresponding SEM image of dried disks with 650 nm and 1180 nm in diameter are shown in figures 4.3. (b) and 4.3. (d), respectively. The disks do not exhibit the same hysteresis loops when they are attached to a substrate as when they are released and dried. These differences in magnetic behavior might be due to the little aggregation originated during the drying process[107]. It is interesting to note that

despite the little aggregation, which is noticeable in the SEM images, the hysteresis loop of dried disks maintains a remanence close to zero.

4.3.2. Disks obtained from the positive resist route

Unlike the nanostructures obtained from the negative route, the disks obtained from the positive resist route were only magnetically characterized once they were released into solution. This was due to the fact that before detachment, the array of magnetic dots deposited on top of the resist pillars coexisted with the magnetic layer deposited onto the Si/Ti wafer giving rise to an additional contribution to the total magnetic signal.

In the same way that the released disks obtained from the negative resist route, the magnetic characterization of the disks obtained from the positive resist route was carried out by SQUID at room temperature. After the lift-off process, in which the disks were released from the top of the resist pillars into solution, they were washed and dispersed in deionized water. Then the disks were dried on a Si wafer for the SQUID measurements.

The SQUID magnetization curve of dried disks fabricated from the positive resist route with dimensions specified in table 4.1. are shown in figure 4.5.

Hysteresis loops of the released disks fabricated from positive route appear to be equivalent to those obtained for released disks fabricated from the negative resist route (Figure 4.3. (b) and 4.3. (d)). Therefore, we assumed that the Permalloy disks fabricated by the positive resist route also presented spin-vortex configuration. In fact, this spin configuration was expected for the diameter and thickness of these disk-shape nanostructures according to the phase diagram of Permalloy nanostructures[40].

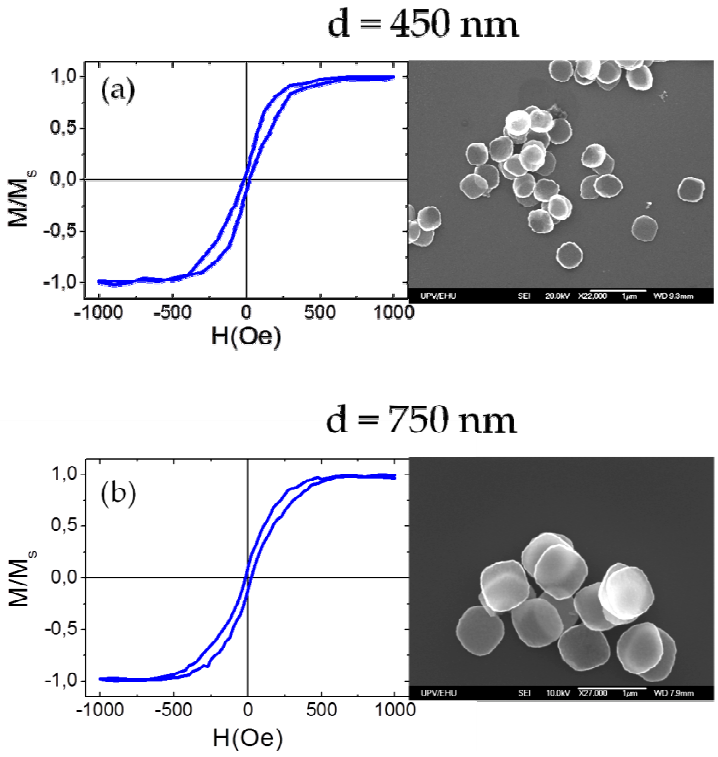

Figure 4.5. Magnetic characterization of released disks (fabricated by the positive resist route) dried on a Si wafer with diameters of (a) 450 nm and (b) 750 nm and Permalloy thicknesses of 25 and 50 nm, respectively.

4.3.3. Magnetic and chemical stability of the vortex-state Permalloy disks

At this point the negative resist route seems to be the most preferable strategy against the positive resist route for the fabrication of MNS since it enables a more thorough magnetic characterization of the magnetic disks before being released into solution, and provides flatter nanostructures (see section 3.3. of chapter 3). However, we should consider the fact that the negative route we propose includes a step of wet etching of the sacrificial layer by two alternative etchants, as was described in sections 3.2.1. and 3.2.2. of chapter 3; a potent oxidizer (H_2O_2) or a strong etchant (KOH), which

could also affect the magnetic layer. To avoid this undesirable effect, a Ti layer was deposited prior and after the Py layer to protect the sides of the Py disk but with this approach the sidewalls of the disk remain unprotected.

Considering that the wet etching step of the negative resist route could damage the magnetic disks, we studied firstly the effects of the H_2O_2 by immersing arrays of Ti/Py/Ti disks deposited on Si wafers in aqueous solutions of H_2O_2. Figure 4.6. shows the magnetization reduction that the arrays of Ti/Py/Ti disks experiment after their immersion in aqueous solutions of H_2O_2 at different concentrations of H_2O_2 and immersion times. The percentage of magnetization reduction was calculated from the saturation magnetization of SQUID hysteresis loops before and after the immersion in the chemical solution. This reduction in the net magnetization corresponds to the proportion of Py that was laterally oxidized in the nanodisks. Three conditions were tested: a) 30% H_2O_2 during 2.5 hours, b) 30% H_2O_2 during 1 hour and c) 15% H_2O_2 during 1 hour. Decreasing the duration of the experiment from 2.5 hours to 1 hour reduces the oxidation from 27% to 16%. The dilution of peroxide has also an important effect. For the same period of time (1 hour) the magnetization reduction can be decreased down to 8% for concentration of 15% H_2O_2.. Immersion times below 1 hour were not tried in this experiment as 1 hour was the time that we took for the chemical etching of the samples with the aqueous solution of H_2O_2 plus subsequent washing process with water until H_2O_2 was completely removed.

The hysteresis loops measured by SQUID prior and after the immersion in H_2O_2 for each condition are shown in the bottom part of figure 4.6. The loops revealed that for any condition the stability of the vortex was not altered. However, slight variation in the shape of the hysteresis loops obtained before and after the immersion was observed for condition (a) (the one which led to the highest magnetization reduction of 27%). This is likely to be due to a little change in the dimensions of the magnetic part of each disk

occasioned by the oxidation. As we explained before, the shape and dimensions of the magnetic nanostructures play a crucial role in determining their magnetic properties. Therefore any variation in these morphological properties is translated into a change in their magnetic behavior. Anyway, this little discrepancy in the shape of the hysteresis loops before and after the immersion was minimized by reducing the concentration of H_2O_2 and the duration of the experiment as we can observe from the hysteresis loops for conditions (b) and (c).

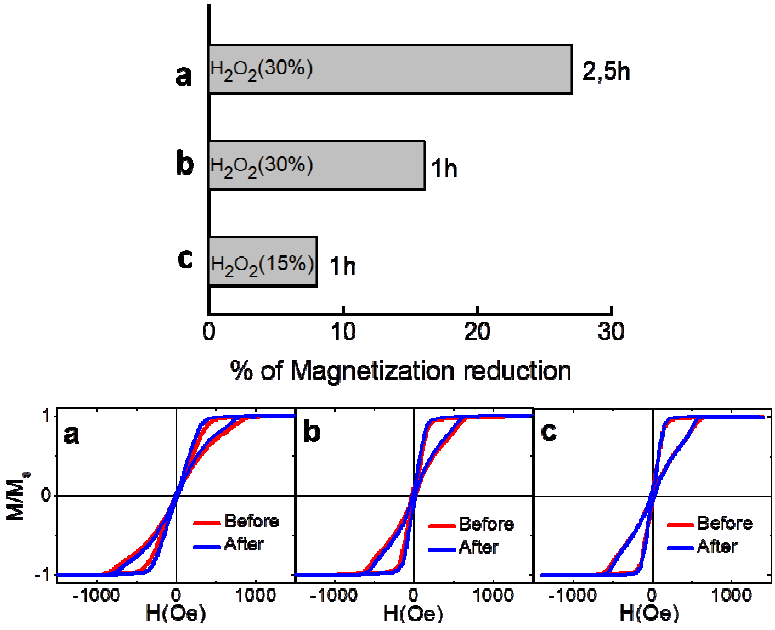

Figure 4.6. Stability test of Py disks (protected by Ti) immersed in aqueous solutions of H_2O_2 at three conditions: a) 30% H_2O_2 during 2.5 hours, b) 30% H_2O_2 during 1 hour and c) 15% H_2O_2 during 1 hour. The corresponding normalized hysteresis loops for the three conditions a), b), c) in which the loop represented by the red and the blue lines correspond to magnetic behavior of the samples before and after the immersion in aqueous solutions of H_2O_2.

Anyway, this little discrepancy in the shape of the hysteresis loops before and after the immersion was minimized by reducing the concentration of H_2O_2 and the duration of the experiment as we can observe from the hysteresis loops for conditions (b) and (c).

At this point we have proved that the oxidative effects from the wet etching step for the release of the nanostructures can be reduced by adapting the conditions of concentration and duration of the experiment. However, another issue we were concerned was the chemical stability in water since the nanostructures were intended to be washed and resuspended in water for the further biological assays. For that reason, an array of Py disks, which had been previously immersed an aqueous solution of H_2O_2 (30%) and oxidized about 39%, was exposed to deionized water for several hours. As it is shown in figure 4.7., the measured magnetization experiments did not experimented a decrease even at long times. That means that the oxidative reaction does not continue when the disks are immersed in water.

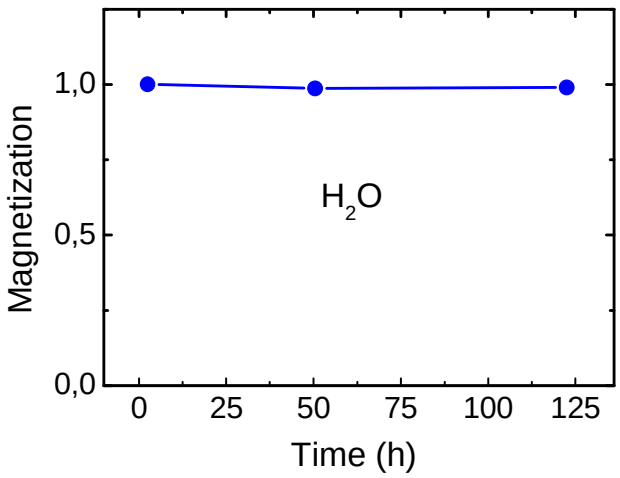

Figure 4.7. Stability test of Py disks (protected by Ti) in deionized water that had been previously undergone an immersion in H_2O_2 (30%) and oxidized the 39%.

Similarly to the oxidation study with H_2O_2 we tested whether the KOH affected the Permalloy layer in the wet etching step. In this case we did not use Ti/Py/Ti disks grown onto Si wafers because KOH also etches Si and detaches a number of disks from the substrate. In that case, an eventual magnetization reduction would be mainly due to the loss of magnetic disks attached to the substrate and not to the etching of the disks sidewalls. An easy solution was to test whether aqueous solutions of KOH etched unprotected Py continuous films.

As seeing in figure 4.8, despite the Py thin film being completely unprotected, little reduction of the magnetization was observed at the first hours of the experiment. The saturation magnetization decreases only (6.7%) for immersions longer than 3 h and less than 2% for almost 1 h. We optimized the wet etching step to last less than1 h. Therefore, we considered that if the magnetization reduction is a 2% for 1 h on a bared continuous Permalloy films, it will be practically negligible on Py disks protected with Ti. Consequently, the etching process of the sacrificial layer in the negative resist route can be significantly optimized using an Al buffer layer and a KOH solution as etchant as long as the magnetic material is not attacked by KOH, as we proved for Permalloy.

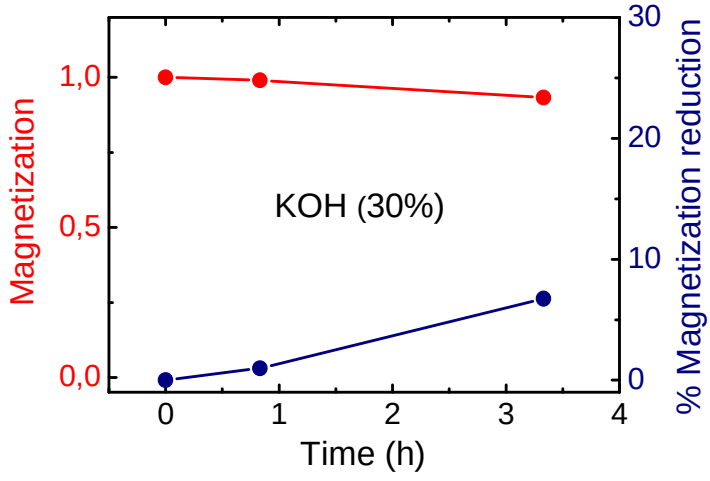

Figure 4.8. Stability test of Permalloy layer in an aqueous solution of 30% KOH.

4.4. Conclusions

Permalloy nanostructures with vortex-state configuration were achieved from two different routes preserving their high-magnetic moment. The negative resist route allowed a complete magnetic characterization thanks to the possibility of characterize the magnetic properties of the nanostructures attached to the substrate revealing a homogeneous magnetic behavior of the over the whole patterned area. Moreover, low remanence was observed for either the disks attached to the substrate or released into solution.

The side effects of the chemical etching of the sacrificial layers were mitigated to preserve the full performance of the MNS. In particular, the etching process of the sacrificial layer in the negative resist route was optimized using an Al buffer layer and a KOH solution as etchant providing an excellent approach to fabricate and preserve high-moment MNS suitable for biotechnical applications, with unique magnetic properties and submicrometric dimensions.

References

[1] K. Y. Guslienko, V. Novosad, Y. Otani, H. Shima, and K. Fukamichi, "Magnetization reversal due to vortex nucleation, displacement, and annihilation in submicron ferromagnetic dot arrays," *Phys. Rev. B*, vol. 65, no. 2, p. 24414, 2001.

[2] S.-H. Chung, R. D. McMichael, D. T. Pierce, and J. Unguris, "Phase diagram of magnetic nanodisks measured by scanning electron microscopy with polarization analysis," *Phys. Rev. B*, vol. 81, no. 2, p. 24410, 2010.

[3] K. Y. Guslienko, "Magnetic vortex state stability, reversal and dynamics in restricted geometries," *J. Nanosci. Nanotechnol.*, vol. 8, no. 6, pp. 2745–2760, 2008.

[4] D.-H. Kim, E. A. Rozhkova, I. V Ulasov, S. D. Bader, T. Rajh, M. S. Lesniak, and V. Novosad, "Biofunctionalized magnetic-vortex microdiscs for targeted cancer-cell destruction," *Nat. Mater.*, vol. 9, no. 2, pp. 165–171, 2010.

[5] T. Okuno, K. Shigeto, T. Ono, K. Mibu, and T. Shinjo, "MFM study of magnetic vortex cores in circular permalloy dots: behavior in external field," *J. Magn. Magn. Mater.*, vol. 240, no. 1, pp. 1–6, 2002.

[6] V. Novosad, M. Grimsditch, J. Darrouzet, J. Pearson, S. D. Bader, V. Metlushko, K. Guslienko, Y. Otani, H. Shima, and K. Fukamichi, "Shape effect on magnetization reversal in chains of interacting ferromagnetic elements," *Appl. Phys. Lett.*, vol. 82, no. 21, pp. 3716–3718, 2003.

[7] A. Vogel, T. Kamionka, M. Martens, A. Drews, K. W. Chou, T. Tyliszczak, H. Stoll, B. Van Waeyenberge, and G. Meier, "Coupled vortex oscillations in spatially separated permalloy squares," *Phys. Rev. Lett.*, vol. 106, no. 13, p. 137201, 2011.

[8] K. Perzlmaier, M. Buess, C. H. Back, V. E. Demidov, B. Hillebrands,

and S. O. Demokritov, “Spin-wave eigenmodes of permalloy squares with a closure domain structure,” *Phys. Rev. Lett.*, vol. 94, no. 5, p. 57202, 2005.

[9] A. Fernandez and C. J. Cerjan, “Nucleation and annihilation of magnetic vortices in submicron-scale Co dots,” *J. Appl. Phys.*, vol. 87, no. 3, pp. 1395–1401, 2000.

[10] M. Schneider, J. Liszkowski, M. Rahm, W. Wegscheider, D. Weiss, H. Hoffmann, and J. Zweck, “Magnetization configurations and hysteresis loops of small permalloy ellipses,” *J. Phys. D. Appl. Phys.*, vol. 36, no. 18, p. 2239, 2003.

[11] K. S. Buchanan, P. E. Roy, F. Y. Fradin, K. Y. Guslienko, M. Grimsditch, S. D. Bader, and V. Novosad, “Vortex dynamics in patterned ferromagnetic ellipses,” *J. Appl. Phys.*, vol. 99, no. 8, p. 08C707, 2006.

[12] K. S. Buchanan, P. E. Roy, M. Grimsditch, F. Y. Fradin, K. Y. Guslienko, S. D. Bader, and V. Novosad, “Magnetic-field tunability of the vortex translational mode in micron-sized permalloy ellipses: Experiment and micromagnetic modeling,” *Phys. Rev. B*, vol. 74, no. 6, p. 64404, 2006.

[13] R. P. Cowburn, D. K. Koltsov, A. O. Adeyeye, M. E. Welland, and D. M. Tricker, “Single-domain circular nanomagnets,” *Phys. Rev. Lett.*, vol. 83, no. 5, p. 1042, 1999.

[14] R. P. Cowburn, “Property variation with shape in magnetic nanoelements,” *J. Phys. D. Appl. Phys.*, vol. 33, no. 1, p. R1, 2000.

[15] X. Zhu, P. Grütter, V. Metlushko, and B. Ilic, “Magnetic force microscopy study of electron-beam-patterned soft permalloy particles: Technique and magnetization behavior,” *Phys. Rev. B*, vol. 66, no. 2, p. 24423, 2002.

[16] M. Natali, I. L. Prejbeanu, A. Lebib, L. D. Buda, K. Ounadjela, and Y. Chen, “Correlated magnetic vortex chains in mesoscopic cobalt dot arrays,” *Phys. Rev. Lett.*, vol. 88, no. 15, p. 157203, 2002.

[17] M. Schneider, H. Hoffmann, S. Otto, T. Haug, and J. Zweck, "Stability of magnetic vortices in flat submicron permalloy cylinders," *J. Appl. Phys.*, vol. 92, no. 3, pp. 1466–1472, 2002.

[18] M. Schneider, H. Hoffmann, and J. Zweck, "Lorentz microscopy of circular ferromagnetic permalloy nanodisks," *Appl. Phys. Lett.*, vol. 77, no. 18, pp. 2909–2911, 2000.

[19] T. Shinjo, T. Okuno, R. Hassdorf, K. Shigeto, and T. Ono, "Magnetic vortex core observation in circular dots of permalloy," *Science (80-.).*, vol. 289, no. 5481, pp. 930–932, 2000.

[20] R. Murillo, H. A. Van Wolferen, L. Abelmann, and J. C. Lodder, "Fabrication of patterned magnetic nanodots by laser interference lithography," *Microelectron. Eng.*, vol. 78, pp. 260–265, 2005.

[21] V. Novosad, K. Y. Guslienko, H. Shima, Y. Otani, K. Fukamichi, N. Kikuchi, O. Kitakami, and Y. Shimada, "Nucleation and annihilation of magnetic vortices in sub-micron permalloy dots," *IEEE Trans. Magn.*, vol. 37, no. 4, pp. 2088–2090, 2001.

[22] K. Y. Guslienko, V. Novosad, Y. Otani, H. Shima, and K. Fukamichi, "Field evolution of magnetic vortex state in ferromagnetic disks," *Appl. Phys. Lett.*, vol. 78, no. 24, pp. 3848–3850, 2001.

[23] D. Mahl, J. Diendorf, W. Meyer-Zaika, and M. Epple, "Possibilities and limitations of different analytical methods for the size determination of a bimodal dispersion of metallic nanoparticles," *Colloids Surfaces A Physicochem. Eng. Asp.*, vol. 377, no. 1, pp. 386–392, 2011.

Chapter 5

Fe nanostructures: Vortex-state and synthetic antiferromagnets

5.1. Introduction

The interest of using magnetic nanostructures (MNS) composed of metallic Fe for biomedical applications lies in its higher saturation magnetization and reduced toxicity compared to other magnetic elements such as Co and Ni (or alloys like NiFe). In this chapter, the fabrication and magnetic characterization of Fe nanostructures for biomedical applications with two magnetic configurations: spin vortex-state and synthetic antiferromagnets (SAF) are presented. These Fe nanostructures were prepared with the collaboration of Professor Ivan K. Schuller from the University of California San Diego (UCSD) during a research stay in his laboratory.

Fe vortex-state nanostructures. The vortex state is characterized by an in-plane flux-closure spin distribution resulting in a net zero magnetization in

the absence of external magnetic field. This configuration is the spin remanent state for single layers of soft submicrometric disks with certain dimensions as explained in detail in the previous chapter.

The magnetization reversal of vortex-state nanostructures characterized by the nucleation, vortex displacement and annihilation have been extensively investigated over a wide range of dimensions (from a few tens of nanometers to one micron) in Permalloy[41], [44]–[47], Superpermalloy[40], [43], [48], and Co[49]–[54] submicrometric elements.

Spin vortex state has also been found experimentally and theoretically in sub-100nm Fe dots[55]–[58]. However, little investigation has been carried out by now on bigger Fe dots (in the submicrometric range).

In this chapter we investigate the stability and evolution of the vortex state in Fe disks fabricated by IL with a diameter of 650 nm over several disk thicknesses that range from 10 to 100 nm. Moreover, the fabrication strategy for the detachment of the disks from the substrate was used to obtain Fe disks in solution for biomedical applications. The fabrication details and magnetic characterization are shown in section 5.2.

Synthetic Antiferromagnetic nanostructures (SAF). Besides the vortex state MNS, a different class of disk-shaped MNS with a more complex magnetic configuration based on multilayer structures was studied in this chapter. These MNS consist basically on two ferromagnetic layers of the same thickness separated by a thin non-magnetic spacer layer. By tuning the thickness of the spacer, an antiparallel alignment of the magnetizations of the ferromagnetic layers can be obtained leading to a zero net magnetization in absence of external field[59]. Thus, these MNS are called synthetic antiferromagnetic nanostructures (SAF).

The magnetic properties of a trilayer systems composed of two ferromagnetic disks separated by a nonmagnetic spacer are different from those of isolated dots due to the magnetostatic and interlayer exchange

coupling across the spacer. Depending on the thickness of the spacer, the coupling between the ferromagnetic layers can be mainly mediated by magnetostatic or interlayer exchange interactions.

When the spacer is relatively thick (above a few nm), the ferromagnetic layers can become weakly coupled and interact mainly through magnetostatic interactions like poles repealing[108]. Thus, the magnetizations of the ferromagnetic layers are antiparallel at low fields, cancelling each other. In this case, the strength of magnetostatic interactions depends strongly on the aspect ratio of the magnetic layers[59].

The interlayer exchange coupling can also play an important role depending on the composition and the thickness of the spacer. Particularly, very thin special spacers, as chromium or ruthenium layers (over 1 nm) can lead to a strong interlayer exchange coupling[84] resulting from the Ruderman–Kittel–Kasuya–Yosida (RKKY) interaction across the nonmagnetic spacer layer[109]–[111]. The RKKY interaction decays oscillatory with the distance, which means that that the relative alignments of the two layers oscillate between ferromagnetic (parallel) and antiferromagnetic (antiparallel) with the thickness of the spacer layer[112]–[114]. This effect depends roughly on the spacer material, its thickness and the number of interfaces. Moreover, it requires very low interfacial roughness[115].

In order to fabricate MNS for biomedical applications we chose Fe as ferromagnetic layer due to its high saturation magnetization and reduced toxicity and Ti as the spacer layer for its well known biocompatibility. The fabrication process and the magnetic characterization of the SAF's we developed are presented in section 5.3. of this chapter.

5.2. Fe nanostructures: vortex state

In order to establish the conditions for the appearance of vortex states in submicrometric Fe disks and its size dependent magnetic properties, we fabricated and magnetically characterized a set of Fe disk patterns of 650 nm in diameter and thicknesses between 10 and 100 nm.

Antidot resist templates on Si wafers were fabricated by IL using the negative resist tone. Fe layers of different thicknesses were deposited by e-beam evaporation at a work pressure of 10^{-8} Torr and at a rate of 0.5 Å/s. Ti layers 5 nm thick were deposited before and after the Fe layers to protect Fe from oxidation. After the lift-off with NMP the arrays of Fe disks (covered by Ti) were obtained and prepared to be characterized.

The magnetic characterization was performed by SQUID at room temperature with the applied magnetic field in the disk plane. The Figure 5.1. shows the measured hysteresis loops of the arrays of Fe disks as a function of the disk thickness.

The thinnest disks (10 nm) present a nearly squared hysteresis loop with high remanence (77%). By increasing the disk thickness to 20 nm, we observed a reduction in the remanence to 60% and a narrowing of the hysteresis loop in the middle, at low magnetic fields.

In thicker disks (from 30 to 100 nm), the remanence completely vanishes and the magnetization reversal process is governed by the nucleation, displacement and annihilation of magnetic vortices.

While comparing the vortex state loops that appear for disks with thicknesses from 30 to 100 nm, we observed that the slope of the linear part of the loop decrease progressively with the disk thickness. Indeed, this linear and reversible part of the hysteresis loop called initial susceptibility, corresponds to vortex core movement perpendicular to the applied

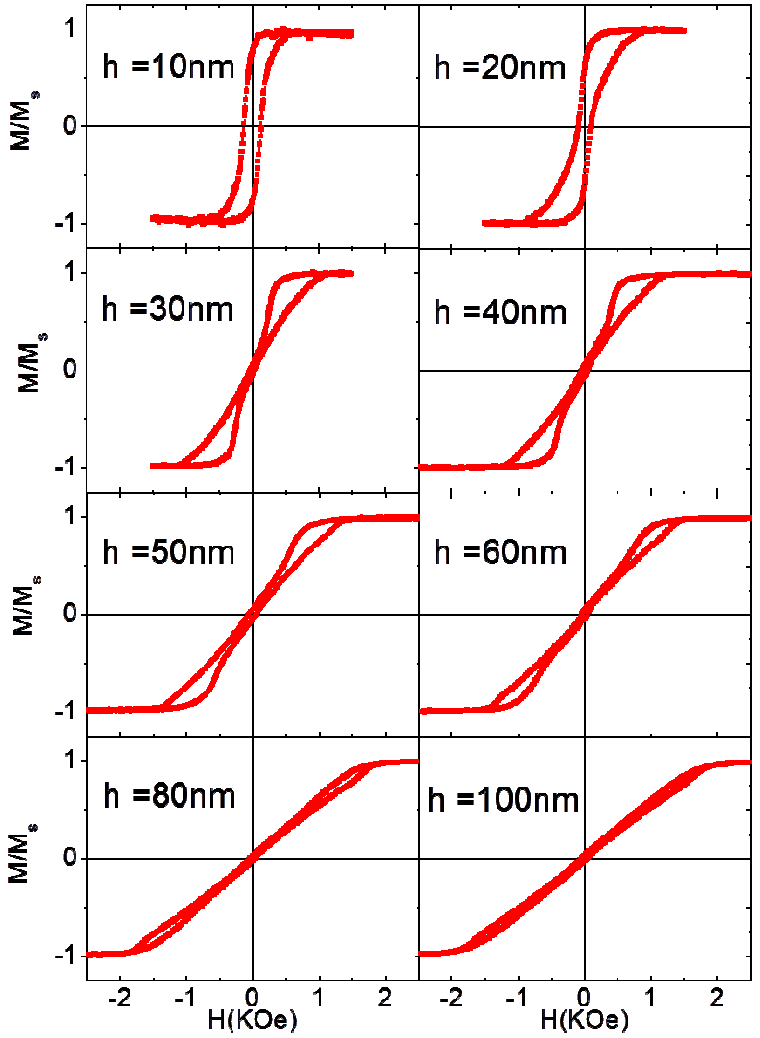

Figure 5.1. Hysteresis loops of arrays of Fe disks with diameter of 650 nm and thicknesses between 10 and 100 nm.

magnetic field, and is strongly thickness dependent. Moreover, there is also a thickness dependent effect for the magnetization fields at which the nucleation and annihilation of the vortices occur.

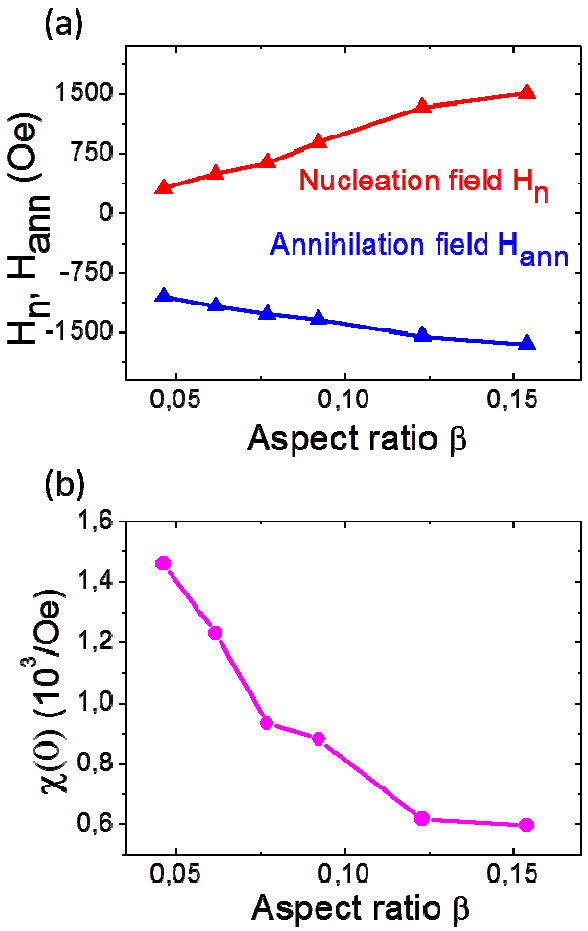

Figure 5.2. (a) The experimental vortex nucleation and annihilation fields and (b) the initial susceptibility relative to Fe as a function of the aspect ratio obtained in arrays of Fe disks.

In figure 5.2. (a) the evolution of the nucleation and annihilation fields as a function of the disk aspect ratio β = (thickness/diameter) is shown. In the same way, in figure 5.2. (b) we show the evolution the initial susceptibility relative to Fe as a function of the aspect ratio. Here, the initial susceptibility is referred to the rate of increase of the magnetic moment of a Fe vortex-state disk as a function of the magnetic field in the linear part of the magnetization curve. This magnitude was obtained for the disks of different

aspect ratios by linear fitting of the linear part of the normalized hysteresis loops appearing in figure 5.1.

The nucleation and annihilation fields increase, whereas the initial susceptibility relative to Fe decreases with increasing the disk aspect ratio. This is the same tendency as the one found experimentally and theoretically for vortex state Permalloy disks[41].

5.3. Fe nanostructures: SAFs

5.3.1. Unpatterned SAFs

Unpatterned Fe/spacer/Fe systems were developed aiming to study the conditions of the non-magnetic spacer for the appearance of interlayer exchange coupling (RKKY) between the Fe layers. This study was carried out on unpatterned systems for the simplicity of the fabrication process. Once the conditions of the spacer for the RKKY interaction are found, they are intended to apply also for patterned ferromagnetic structures. For this purpose, multilayer systems composed of two ferromagnetic layers separated by a wedge shaped spacer, schematized in Figure 5.3, were prepared by e-beam evaporation. The wedge-shaped layers enable an accurate variation of the spacer layer thickness to study the effect of the spacer thickness on the interlayer coupling between the ferromagnetic layers.

The multilayer structure Ti/Fe/Ti-wedge/Fe/Ti was fabricated by e-beam evaporation at a base pressure of 10^{-8} Torr as follows. Two Ti layers were deposited before and after the sandwich structure (Fe/Ti/Fe) as cap layers with a thickness of 5 nm at a deposition rate of 0.5 Å/s. The Fe layers 10 nm thick were deposited at a rate of 0.5 Å/s. The Ti wedge with the thickness

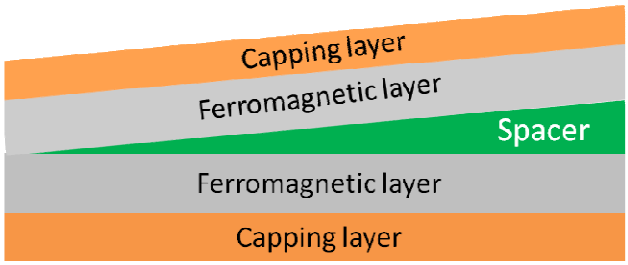

Figure 5.3. Schematic of the multilayer structure with a wedge-shaped spacer grown between two ferromagnetic layers.

ranging from 0 to 5 nm (grown at a deposition rate of 0.3 Å/s) was obtained by moving a linear-motion shutter at a constant speed. After the deposition process, the sample with multilayer structure was cut into pieces so that each piece had a spacer thickness variation of 2.3 Å. The set of sample pieces was magnetically characterized by SQUID at room temperature with applied magnetic field in the plane of the samples.

A study of the magnetic response of the Fe/Ti/Fe structures was carried out as a function of the spacer thickness. We obtained nearly squared hysteresis loops for the whole range of the Ti thicknesses (0 – 5 nm), figure 5.4. (a,b), presenting variations in the coercive field when varying the thickness of the spacer layer as showed in figure 5.4. (c). However, no antiparallel coupling was achieved between the ferromagnetic layers as we did not observed the drastic remanence reduction expected when antiparallel coupling dominates the magnetization reversal process.

The use of special non magnetic materials such as Ruthenium spacers has shown excellent results in the fabrication of antiparallel coupled structures through RKKY interaction as it has been reported in the literature[14], [61], [116]. However, in this study we aimed to use more biocompatible spacer materials such as Ti for the application of the designed nanostructures in biomedicine. Since no RKKY coupling was found with our Fe/Ti/Fe structures, we investigated the other interaction that has been shown to

originate antiparallel alignment between ferromagnetic layers: the magnetostatic coupling.

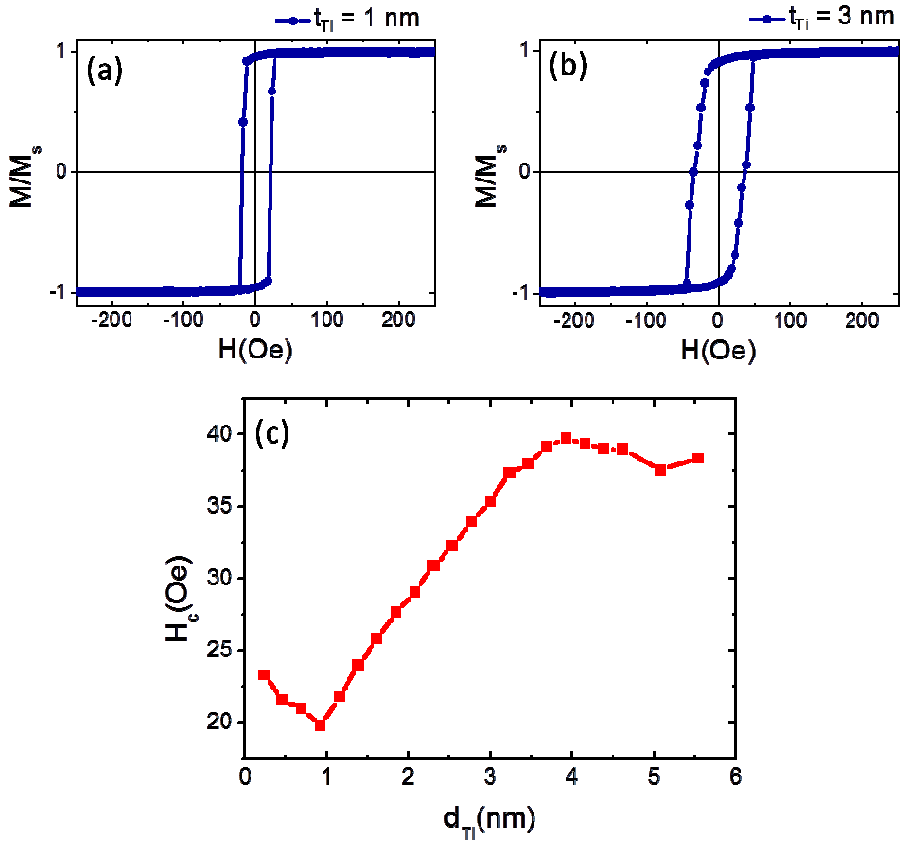

Figure 5.4. (a), (b) Magnetic curves of Fe(10nm)/Ti(t_{Ti})/Fe(10nm) multilayers with a Ti spacer thickness t_{Ti} of 0.92 and 3 nm, respectively. (c) Variation of the coercive field as a function of t_{Ti}.

Since the magnetostatic coupling in SAF's originate from the stray fields, the study of this interaction in Fe/Ti/Fe structures was not performed on unpatterned multilayer structures but directly on patterned disks. The reason for this is that ideal continuous films are considered to have infinite lateral dimensions so that the stray fields (responsible for the magnetostatic coupling between layers) are zero when the sample is magnetized in the

film plane. The fabrication and magnetic characterization of Fe/Ti/Fe patterned structures is presented in the following section.

5.3.2. Patterned SAFs

For the development of the SAFs we employed resist antidot templates fabricated on Si wafers using our IL system. On the resist templates, the Fe/Ti/Fe stack that constitutes this type of MNS was deposited by e-beam evaporation. Additional Ti layers 5 nm thick were deposited on top and below the magnetic stack to prevent from oxidation. After lift-off with NMP, arrays of disk-shaped MNS of 650 nm in diameter with the structure Ti(5nm)/Fe(t_{Fe})/Ti(t_{Ti})/Fe(t_{Fe})/Ti(5nm) were obtained, in which t_{Fe} and t_{Ti} are the Fe and Ti layer thicknesses, respectively.

The magnetic characterization was carried out by SQUID at room temperature with the magnetic field applied in the plane of wafers.

The study of the origin of the interaction between the ferromagnetic layers in the SAF's and the effect of different parameters on the magnetic interlayer interaction such as the spacer thickness, the number of repetitions and the thickness of the ferromagnetic layers is presented below.

Interaction between the ferromagnetic layers

In order to determine the origin of the magnetic properties of trilayer Fe/Ti/Fe disks, we compared its magnetization reversal process with single-layer Fe disks and Fe/Ti/Fe unpatterned systems.

Single layer Fe disks 10 nm thick presented nearly squared magnetic curves (Figure 5.5. (a)) and isotropic magnetic behavior in all in-plane directions. The magnetic characterization of unpatterned trilayer structures (10nm)/Ti (3nm)/Fe (10nm) (Figure 5.5. b)) also revealed high remanence and nearly squared histerisis loops. By contrast, the measured hysteresis loop for the

trilayer disks with structure Fe (10nm)/Ti (3nm)/Fe (10nm) showed drastically reduced remanence with respect to the hysteresis loop for single-layer Fe disks 10 nm thick of the same dimensions (Figure 5.5. (a)) indicating that magnetic interactions were involved between the two Fe layers. Moreover, the magnetization reversal process of the trilayer disks showed in Figure 5.5. (a) is clearly different from that corresponding to the unpatterned films (Fig 5.5. (b)) with identical trilayer structure

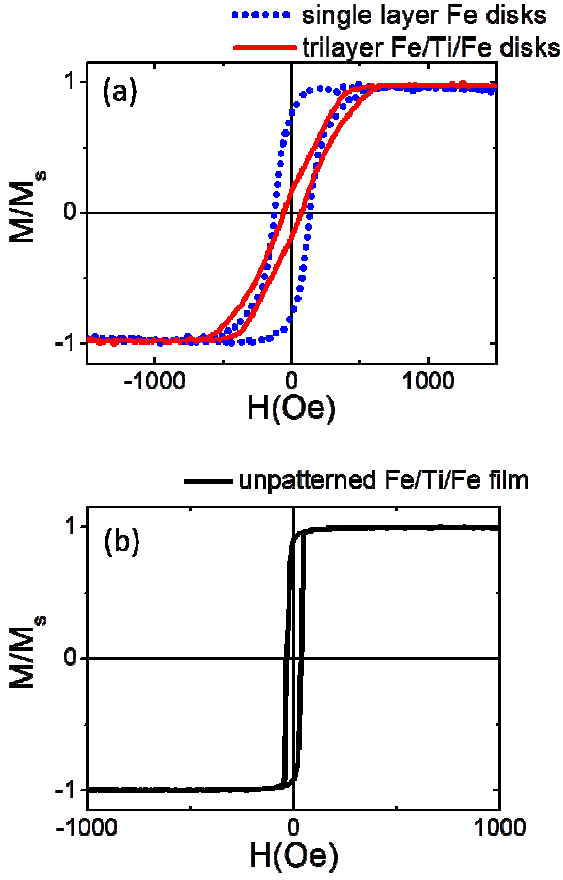

Figure 5.5. (a) Hysteresis loops of an array of single layer Fe disks 10nm thick (blue dotted line) and an array of Fe(10 nm)/Ti(3 nm)/Fe(10 nm) disks (red solid line) (b) Hysteresis loop of an unpatterned trilayer Fe(10 nm)/Ti(3 nm)/Fe(10 nm) film.

Fe(10nm)/Ti(3nm)/Fe(10nm). This suggests that the magnetic coupling between layers is related to the dimensions and geometry of the trilayer nanodisks and not exclusively to the trilayer structure also present in unpatterned films.

For those reasons and since the spacer of the trilayer is thick enough (3 nm) to ignore the interlayer exchange coupling, magnetostatic coupling appears to dominate the magnetization reversal process of trilayer disks.

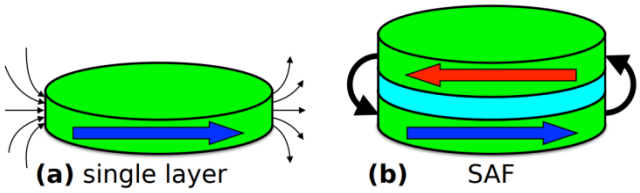

Figure 5.6. A schematic of the field profiles of (a) magnetic single layer and (b) SAF. The coloured arrows correspond to the magnetization in the respective layer.

Generally, the magnetostatic coupling in SAFs originates from the "magnetic charges" at the edges of the magnetic disk layers, which are a source of external demagnetizing field or stray-field. The second layer that is involved in the coupling experiences the stray field from the first layer as an external field opposite to the magnetization of the first layer. This results in a dipole coupling (Figure 5.6.). Ideal non patterned thin films are considerate to have infinite lateral dimensions so the stray fields are zero when the sample is magnetized in the film plane. For this reason we did not find any magnetostatic coupling in our non patterned trilayer films.

Effect of the spacer thickness

The spacer thickness was varied to study the extent of the dipolar interaction across the non magnetic spacer. For that purpose we fabricated a set of samples with structure: Ti (5 nm)/Fe (10nm)/Ti (t_{Ti})/Fe (10nm)/Ti (5nm), in which the thickness of the Fe layers is constant for all the samples while the spacer thickness is varied. Since SAF's with Ti spacer thickness of 3 nm showed dipolar interaction of the ferromagnetic layers across the spacer, as presented before in Figure 5.5. (a), we carried out a first study with small variations of the Ti spacer around 3 nm (specifically 2.6, 2.9, 3.2, 3.5 nm) to figure out whether the spacer thickness was critical. We found that all the hysteresis loops of the SAF's with spacer thickness in that range were equivalent. Therefore, we decided to carried out a second study with spacer thickness in a wider range (from 1.8 nm to 20 nm).

Figure 5.7. shows the magnetization curves measured with SQUID at room temperature of the trilayer disks with a Ti spacer thickness of 1.8, 8 and 20 nm. Similar magnetic behavior was observed for all the spacer thicknesses. Thus, the coupling between layers does not critically depend on the spacer thickness and it extends even to thick Ti spacers. However, we observed that as the spacer thickness increased the hysteresis loops broadened, especially close to saturation, deviating from the reversible response that is expected for ideal SAF's magnetic behavior.

Effect of the number of repetitions (n)

In this part of the study, Ti (5nm)/$[Fe/Ti]_n$ /Fe/Ti (5 nm) multilayers were prepared, in which the number of repetitions n was varied while the thicknesses of the Fe layer and the Ti spacer were kept constant to 10 nm and 3 nm, respectively.

The objective of increasing the number of repetitions was to enhance the magnetostatic interactions as each internal Fe layer in the Fe/Ti multilayer

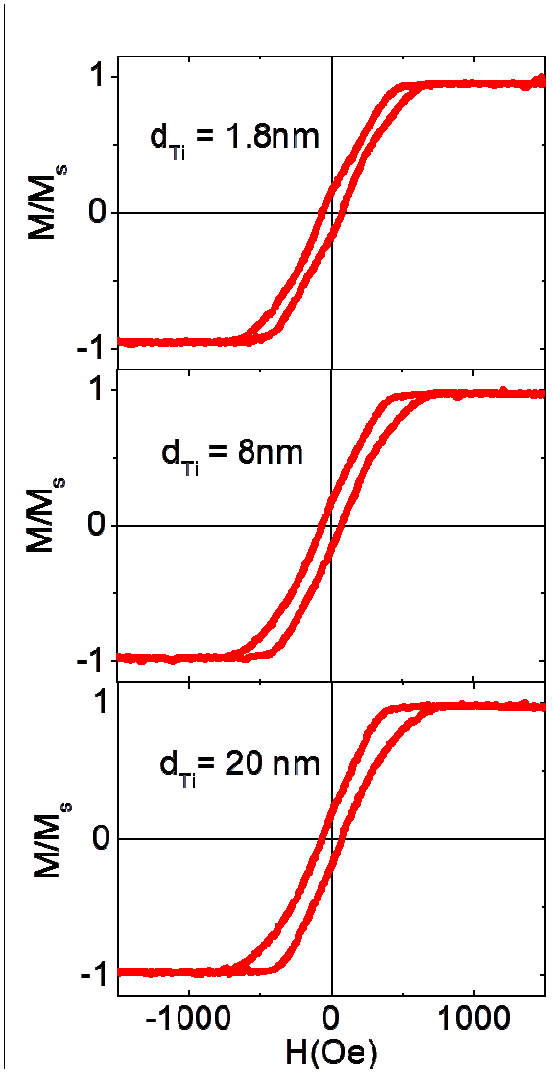

Figure 5.7. Hysteresis loops of arrays of disks with structure Ti(5nm)/Fe(10 nm)/Ti(t_{Ti})/Fe(10 nm)/Ti(5nm), in which the thickness of the Ti spacer is set to 1.8, 8 and 20 nm.

structure would be coupled not only to a single Fe layer (as it was the case of n = 1) but to one Fe layer underneath and to another on top. This was intended to strengthen the magnetostatic interactions.

The structures with n = 1, which correspond to the trilayer disks in Figure 5.5. (a), present dipolar coupling between the Fe layers as we discussed above. By increasing an odd number of repetitions and due to the dipolar coupling, the magnetization in successive Fe layers should also be spontaneously oriented antiparallel to each other.

Figure 5.8. shows the magnetic characterization by SQUID at room temperature of Ti (5nm)/[Fe/Ti]$_n$/Fe/Ti (5 nm) multilayers, in which the number of repetitions n was set to 1 (red solid line), 3 (black dot line), and 5 (blue dashed line).

As we can observe from the hysteresis loops, by increasing the number of repetitions, the saturation field increases. Moreover, the remanence is significantly reduced from the 17% for n = 1 to the 10% for n = 3 and 5, which accounts for the enhancement of the magnetostatic interactions. Even with this enhancement, we did not achieve null renanence.

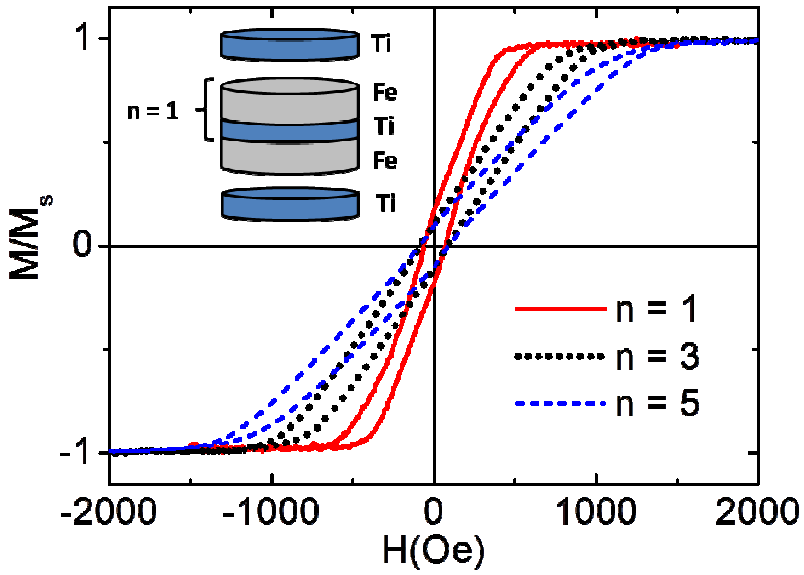

Figure 5.8. Magnetic characterization of Ti(5nm)/[Fe/Ti]$_n$ /Fe/Ti(5 nm) multilayers with n = 1, 3 and 5.

Effect of the ferromagnetic layer thickness

The variation of the ferromagnetic layers thickness while keeping the spacer thickness constant has a dramatic effect on the magnetization reversal process of SAF's.

Figure 5.9. shows the hysteresis loops of arrays of disks with structure Ti (5 nm)/Fe (t_{Fe})/Ti (3nm)/Fe (t_{Fe})/Ti (5nm), in which the Ti spacer thickness was set to 3 nm and the Fe thickness (t_{Fe}) was varied from 3 to 50 nm.

We clearly see from the evolution of the magnetization reversal process by varying t_{Fe} that the saturation field increases and the remanence decreases with increasing the Fe thickness in Fe/Ti/Fe disks. However, we have to take into consideration the magnetization reversal process of the single Fe layers with the different thicknesses so that we do not wrongly attribute the differences in magnetic behavior for different Fe thicknesses exclusively to the magnetic coupling.

As we demonstrated in the section 5.2. of this chapter, single layer Fe disks with thicknesses above 30 nm present vortex state configuration. Therefore, the Fe/Ti/Fe disks we fabricated with t_{Fe} = 30 and 50 nm consist in two vortex-state disks separated by a non magnetic layer. Thus, the low remanence that these Fe/Ti/Fe disks present is due to the spin flux closure [117], characteristic of the spin vortex sate arrangement instead of the antiparallel magnetization alignment that occur in SAFs.

The single layer Fe disks with t_{Fe} below 20 nm do not present vortex state configuration (Figure 5.1.). In general, in cylindrical dots, when the aspect ratio is below a critical value, the magnetic configuration changes from vortex-state to single domain state[40]. We assume that this is the transition that Fe disks experimented below 20nm. In this case, the drastic reduction in remanence when separating two Fe disks with thicknesses below 20 nm by a Ti spacer is not due to the spin flux closure in the Fe layers but to the magnetic coupling between the Fe layers. As we discussed in section 5.2, the

remanences for single layer Fe disks with thicknesses of 10 nm and 20 nm were the 77% and the 60%, respectively. In Figure 5.9, we see that the effect of coupling two Fe disks produce the reduction of the magnetization to the 17.8% and 7.7% for disks with thicknesses of 10 and 20 nm, respectively.

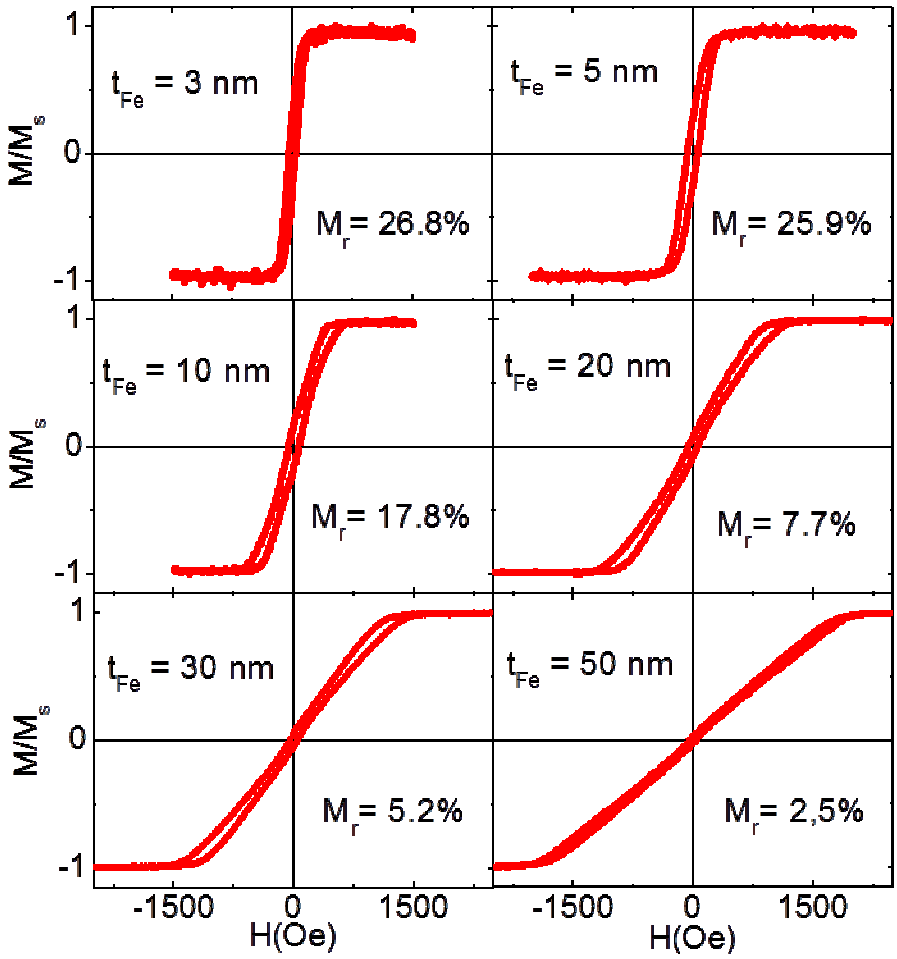

Figure 5.9. The dependence of the magnetic properties of disks with structure Ti(5nm)/Fe(t_{Fe})/Ti(3 nm$_i$)/Fe(t_{Fe})/Ti(5nm), in which the Fe thickness (t_{Fe}) is varied from 3 to 50 nm. The magnetization remanence (M_r) is also displayed for each trilayer.

In summary, the trilayers with t_{Fe} above 30 nm present the lowest remanences (5% for t_{Fe} = 30 nm and 2.5% for t_{Fe} = 50 nm) due to the presence of two vortex-state Fe layers instead of the interlayer coupling that takes place in SAFs. By contrast, the trilayers with t_{Fe} below 20 nm present remanence reduction compared to the single layers due to the presence of magnetic coupling of the Fe layers across the spacer. Among this group, the trilayer with t_{Fe} = 20 nm present the lowest remanence and therefore the most desirable results.

5.4. Fe disks for biomedical applications

The SAFs that we prepared only present advantages for their application in biomedicine with respect to single-layer Fe disks for Fe thicknesses under 20 nm, at which they exhibit a reduced remanence.

For thicker Fe layers, (in a wide range between 30 and 100 nm) single-layer Fe disks present spin vortex configuration accompanied by a nearly zero remanence highly desirable for biomedical applications. Moreover, they are much easier to prepare since they consist of only one thick layer.

Due to the simplicity of the fabrication and the excellent magnetic properties, single layer Fe disks with spin vortex configuration were chosen for their fabrication in solution for biomedical applications.

Fabrication and characterization of vortex-state Fe disks in solution

In section 5.2. the arrays of single-layer Fe disks were deposited on Si wafers since the objective was to characterize the samples and determine the morphological properties that lead to vortex-state configuration. Once those conditions were obtained, the aim in this section is to fabricate vortex state disks on a release layer, which enables to detach them into solution.

By using the negative resist fabrication route (explained in chapter 3), the Fe layers deposited by e-beam evaporation were patterned in the shape of disks, followed by its liberation into solution through the removal of a Ge release layer by an aqueous solution of H_2O_2.

The Fe disks 650 nm in diameter grown on the Ge release layer consisted on a Fe layer 50 nm thick coated on both sides by Ti layers 5 nm thick to prevent Fe disks from oxidation. The deposition parameters for Fe and Ti were the same as the ones used and explained in section 5.3.1.

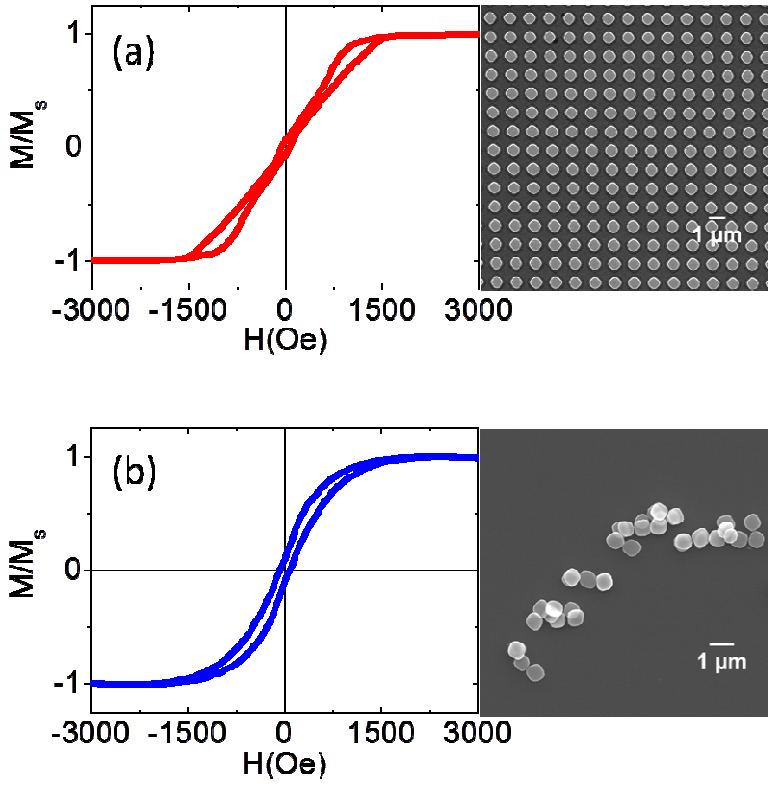

Figure 5.10. Magnetic characterization by SQUID at room temperature and SEM images of: (a) an array of Fe disks 50 nm thick grown on a Ge release layer, (b) released disks dried on a Si wafer.

The magnetic characterization of the array of Fe disks grown on the Ge layer was carried out by SQUID at room temperature with the magnetic field applied parallel to the disks plane. The measured hysteresis loop (showed in Figure 5.10. (a)) is similar to the hysteresis loop obtained for the array of Fe disks of the same dimensions grown directly on the Si wafer, which was showed in Figure 5.1. Therefore, the fact of including a Ge release layer does not alter the magnetic properties of the Fe nanostructures.

The magnetic characterization of the released Fe disks is shown in Figure 5.10. (b). The disks were detached from the wafer by the immersion of the sample in an aqueous solution of 15% H_2O_2 placed in an ultrasonic bath. Then, they were washed and resuspended in deionized water. The preparation of the sample for the magnetic measurements consisted in drying a droplet of Fe disks dispersed in deionized water on a Si wafer. The dried disks were magnetically characterized by SQUID at room temperature.

The hysteresis loop of the release and dried disks (Figure 5.10. (b)) does no coincide with the hysteresis loop of the array of Fe disks attached to the substrate (Figure 5.10. (a)). In fact, the hysteresis loop of the dried disks does not present neither a linear reversible part at low fields nor a defined nucleation and annihilation fields of the vortex state. This might be due to the little aggregation during the drying process so the nanostructures do not behave as isolated Fe disks. However, low remanence and low coercivity are achieved in both cases.

Magnetic and chemical stability of the Fe disks

The fabrication of the Fe disks in solution with the strategy we developed included the release step, in which the disks were immersed in an aqueous solution of 15% H_2O_2 that etched the release layer of Ge and releases the disks into solution.

As explained before, a Ti layer was deposited prior and after the Fe layer to protect the top and bottom disk sides from oxidation. In this way, for the Fe disks we used (650 nm in diameter), the 82% of the total area in contact with the Ge etchant was protected by Ti. However, the sidewalls of the disk representing the 18% of the disk area in contact with the liquid medium remained unprotected.

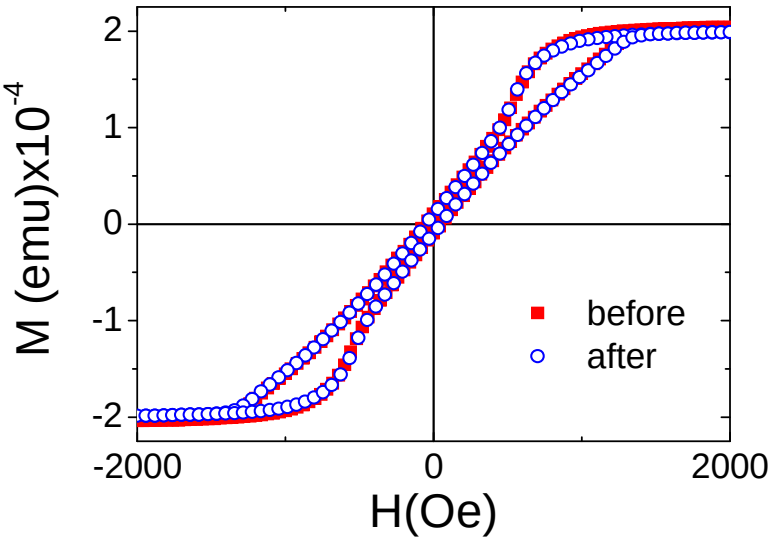

Figure 5.11. Hysteresis loops measured by SQUID before (filled red squares) and after (blue open circles) the immersion of the array of Fe disks into an aqueous solution of 15% H_2O_2 for 1 hour.

In order to study whether the release step affected negatively the Fe disks, we immersed an array of Fe disks of the same structure and dimensions in the aqueous solution of H_2O_2 used in the released step. In this case, the array of disks was grown on a Si wafer so they are not detached from the wafer in the H_2O_2 immersion. Thus, we were able to study the magnetic behavior and calculate the total magnetic signal of the sample prior and after the immersion in H_2O_2.

Figure 5.11. shows the hysteresis loops of an array of Fe disks with 650 nm of diameter and 50 nm of thickness measured by SQUID before and after the immersion in an aqueous solution of 15% H_2O_2 for 1 hour.

As we can observe, the shape of the hysteresis loop remain intact after the immersion in the aqueous solution of H_2O_2. Therefore, the magnetic behavior is not altered by Ge etchant used in the release process of the Fe disks. In addition to this, the total magnetic signal was reduced by only a 2.5%.

5.5. Conclusions

We revealed the presence of magnetic vortex state configuration in Fe disks 650 nm in diameter within a wide range of disk thicknesses between 30 and 100 nm.

The study of the interlayer interactions in trilayered structures revealed that RKKY coupling was not present on our Fe/Ti/Fe unpatterned multilayers. By contrast, we acheived antiparallel alignment on patterned Fe/Ti/Fe structures by means of magnetostatic interactions. However, the alignment was not perfect as the SAF's displayed small but not null remanence.

The residual remanence in our SAF's was reduced by increasing the number of repetitions of the sandwiched structure. The same tendency was also observed when increasing the Fe thickness (until 20 nm). However, even with these enhancements the remanence was not completely vanished.

The Fe/Ti/Fe structures with Fe thickness above 30 nm did present nearly zero remanence. However, these structures were composed of two vortex-state layers separated by a non magnetic layer. For these thicknesses we cannot talk about SAF's since the antiparallel alignment was not the

responsible for the zero remanence but the vortex-state structure of the single layers.

Single layer Fe disks with spin vortex configuration were chosen for their fabrication in solution for biomedical applications due to the simplicity of the fabrication process and the improved magnetic properties with respect to the Fe/Ti/Fe structures that were developed.

We succeeded in fabricating vortex state Fe disks in solution. Moreover, we proved that the etchant responsible for the release of the disks from the substrate into solution did not affect their magnetic properties.

References

[1] K. Y. Guslienko, V. Novosad, Y. Otani, H. Shima, and K. Fukamichi, "Field evolution of magnetic vortex state in ferromagnetic disks," *Appl. Phys. Lett.*, vol. 78, no. 24, pp. 3848–3850, 2001.

[2] V. Novosad, K. Y. Guslienko, H. Shima, Y. Otani, K. Fukamichi, N. Kikuchi, O. Kitakami, and Y. Shimada, "Nucleation and annihilation of magnetic vortices in sub-micron permalloy dots," *IEEE Trans. Magn.*, vol. 37, no. 4, pp. 2088–2090, 2001.

[3] K. Y. Guslienko, V. Novosad, Y. Otani, H. Shima, and K. Fukamichi, "Magnetization reversal due to vortex nucleation, displacement, and annihilation in submicron ferromagnetic dot arrays," *Phys. Rev. B*, vol. 65, no. 2, p. 24414, 2001.

[4] T. Pokhil, D. Song, and J. Nowak, "Spin vortex states and hysteretic properties of submicron size NiFe elements," *J. Appl. Phys.*, vol. 87, no. 9, pp. 6319–6321, 2000.

[5] J. K. Ha, R. Hertel, and J. Kirschner, "Micromagnetic study of magnetic configurations in submicron permalloy disks," *Phys. Rev. B*, vol. 67, no. 22, p. 224432, 2003.

[6] R. P. Cowburn, D. K. Koltsov, A. O. Adeyeye, M. E. Welland, and D. M. Tricker, "Single-domain circular nanomagnets," *Phys. Rev. Lett.*, vol. 83, no. 5, p. 1042, 1999.

[7] R. P. Cowburn, "Property variation with shape in magnetic nanoelements," *J. Phys. D. Appl. Phys.*, vol. 33, no. 1, p. R1, 2000.

[8] S.-H. Chung, R. D. McMichael, D. T. Pierce, and J. Unguris, "Phase diagram of magnetic nanodisks measured by scanning electron microscopy with polarization analysis," *Phys. Rev. B*, vol. 81, no. 2, p. 24410, 2010.

[9] A. Fernandez and C. J. Cerjan, "Nucleation and annihilation of magnetic vortices in submicron-scale Co dots," *J. Appl. Phys.*, vol. 87,

no. 3, pp. 1395–1401, 2000.

[10] E. Girgis, J. Schelten, J. Shi, J. Janesky, S. Tehrani, and H. Goronkin, "Switching characteristics and magnetization vortices of thin-film cobalt in nanometer-scale patterned arrays," *Appl. Phys. Lett.*, vol. 76, no. 25, pp. 3780–3782, 2000.

[11] L. D. Buda, I. L. Prejbeanu, U. Ebels, and K. Ounadjela, "Micromagnetic simulations of magnetisation in circular cobalt dots," *Comput. Mater. Sci.*, vol. 24, no. 1–2, pp. 181–185, 2002.

[12] A. Lebib, S. P. Li, M. Natali, and Y. Chen, "Size and thickness dependencies of magnetization reversal in Co dot arrays," *J. Appl. Phys.*, vol. 89, no. 7, pp. 3892–3896, 2001.

[13] M. Natali, A. Lebib, Y. Chen, I. L. Prejbeanu, and K. Ounadjela, "Configurational anisotropy in square lattices of interacting cobalt dots," *J. Appl. Phys.*, vol. 91, no. 10, pp. 7041–7043, 2002.

[14] M. Natali, I. L. Prejbeanu, A. Lebib, L. D. Buda, K. Ounadjela, and Y. Chen, "Correlated magnetic vortex chains in mesoscopic cobalt dot arrays," *Phys. Rev. Lett.*, vol. 88, no. 15, p. 157203, 2002.

[15] R. K. Dumas, C.-P. Li, I. V Roshchin, I. K. Schuller, and K. Liu, "Magnetic fingerprints of sub-100 nm Fe dots," *Phys. Rev. B*, vol. 75, no. 13, p. 134405, 2007.

[16] J. Mejía-López, D. Altbir, A. H. Romero, X. Batlle, I. V Roshchin, C.-P. Li, and I. K. Schuller, "Vortex state and effect of anisotropy in sub-100-nm magnetic nanodots," *J. Appl. Phys.*, vol. 100, no. 10, p. 104319, 2006.

[17] I. V Roshchin, C.-P. Li, H. Suhl, X. Batlle, S. Roy, S. K. Sinha, S. Park, R. Pynn, M. R. Fitzsimmons, and J. Mejía-López, "Measurement of the vortex core in sub-100 nm Fe dots using polarized neutron scattering," *EPL (Europhysics Lett.*, vol. 86, no. 6, p. 67008, 2009.

[18] J. Mejía-López, D. Altbir, P. Landeros, J. Escrig, A. H. Romero, I. V Roshchin, C.-P. Li, M. R. Fitzsimmons, X. Batlle, and I. K. Schuller,

"Development of vortex state in circular magnetic nanodots: Theory and experiment," *Phys. Rev. B*, vol. 81, no. 18, p. 184417, 2010.

[19] W. Hu, R. J. Wilson, C. M. Earhart, A. L. Koh, R. Sinclair, and S. X. Wang, "Synthetic antiferromagnetic nanoparticles with tunable susceptibilities," *J. Appl. Phys.*, vol. 105, no. 7, p. 07B508, 2009.

[20] B. Koop, "Static and dynamic properties of uniform-and vortex-states in synthetic nanomagnets." KTH Royal Institute of Technology, 2016.

[21] W. Hu, R. J. Wilson, A. Koh, A. Fu, A. Z. Faranesh, C. M. Earhart, S. J. Osterfeld, S. Han, L. Xu, and S. Guccione, "High-Moment Antiferromagnetic Nanoparticles with Tunable Magnetic Properties," *Adv. Mater.*, vol. 20, no. 8, pp. 1479–1483, 2008.

[22] A. Barthelemy, A. Fert, M. N. Baibich, S. Hadjoudj, F. Petroff, P. Etienne, R. Cabanel, S. Lequien, F. Nguyen Van Dau, and G. Creuzet, "Magnetic and transport properties of Fe/Cr superlattices," *J. Appl. Phys.*, vol. 67, no. 9, pp. 5908–5913, 1990.

[23] Y. Wang, P. M. Levy, and J. L. Fry, "Interlayer magnetic coupling in Fe/Cr multilayered structures," *Phys. Rev. Lett.*, vol. 65, no. 21, p. 2732, 1990.

[24] S. S. P. Parkin, N. More, and K. P. Roche, "Oscillations in exchange coupling and magnetoresistance in metallic superlattice structures: Co/Ru, Co/Cr, and Fe/Cr," *Phys. Rev. Lett.*, vol. 64, no. 19, p. 2304, 1990.

[25] P. Bruno, "Theory of interlayer exchange interactions in magnetic multilayers," *J. Phys. Condens. Matter*, vol. 11, no. 48, p. 9403, 1999.

[26] S. S. P. Parkin, "Systematic variation of the strength and oscillation period of indirect magnetic exchange coupling through the 3d, 4d, and 5d transition metals," *Phys. Rev. Lett.*, vol. 67, no. 25, p. 3598, 1991.

[27] P. Bruno and C. Chappert, "Oscillatory coupling between ferromagnetic layers separated by a nonmagnetic metal spacer,"

Phys. Rev. Lett., vol. 67, no. 12, p. 1602, 1991.

[28] G. Reiss, L. Van Loyen, T. Lucinski, D. Elefant, H. Brückl, N. Mattern, R. Rennekamp, and W. Ernst, "Presence and absence of antiferromagnetic coupling and giant magnetoresistance in sputtered and evaporated permalloy/copper multilayers," *J. Magn. Magn. Mater.*, vol. 184, no. 3, pp. 281–288, 1998.

[29] H. Joisten, T. Courcier, P. Balint, P. Sabon, J. Faure-Vincent, S. Auffret, and B. Dieny, "Self-polarization phenomenon and control of dispersion of synthetic antiferromagnetic nanoparticles for biological applications," *Appl. Phys. Lett.*, vol. 97, no. 25, p. 253112, 2010.

[30] T. Vemulkar, R. Mansell, D. Petit, R. P. Cowburn, and M. S. Lesniak, "Highly tunable perpendicularly magnetized synthetic antiferromagnets for biotechnology applications," *Appl. Phys. Lett.*, vol. 107, no. 1, p. 12403, 2015.

[31] A. L. Koh, W. Hu, R. J. Wilson, C. M. Earhart, S. X. Wang, and R. Sinclair, "Structural and magnetic characterizations of high moment synthetic antiferromagnetic nanoparticles fabricated using self-assembled stamps," *J. Appl. Phys.*, vol. 107, no. 9, p. 09B522, 2010.

[32] K. S. Buchanan, K. Y. Guslienko, A. Doran, A. Scholl, S. D. Bader, and V. Novosad, "Magnetic remanent states and magnetization reversal in patterned trilayer nanodots," *Phys. Rev. B*, vol. 72, no. 13, p. 134415, 2005.

Chapter 6

Dynamic behavior of Magnetic Nanostructures

6.1. Introduction

The biomedical applications that we propose for magnetic nanostructures (MNSs) take advantage of their ability to mechanically actuate on biological systems by means of the torque or mechanical force that MNSs exert under the application of alternating magnetic fields.

When subjected to an external magnetic field, the MNSs will tend to rotate to align their magnetization along the magnetic field direction. When an external magnetic field (H) is applied to vortex-state disks, which have its easy axis in plane, the vortex core displaces developing a magnetic moment (**m**) parallel to the projection of the magnetic field in the plane of the disk. Therefore, the vortex-state disks will experience a driving torque $\boldsymbol{\tau} = \mathbf{m} \times \mathbf{H}$, where the magnetic moment **m** is proportional to the magnetic

susceptibility and the magnetization saturation of the disk. This torque rotates the disk, aligning the plane of the disk along the field direction (Figure 6.1.).

Under the application of an alternating magnetic field the disks oscillate transmitting a mechanical force that can be used to manipulate the cell response even to trigger cell apoptosis[23], [38], [39].

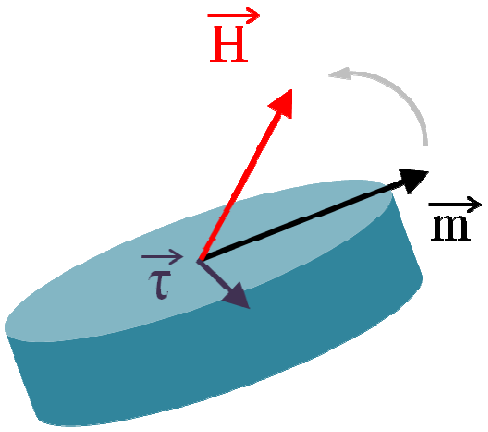

Figure 6.1. A disk-shaped MNS in an external magnetic field subjected to the magnetic torque.

The strength of the magnetic forces depends on the size and composition of the disk, the amplitude of the external magnetic field and the mechanic properties of the cell. Forces of different strengths and dynamic conditions can regulate several cell responses[62]. Therefore, by controlling the dynamics of the disks, the efficiency of the magneto-mechanic actuation for different biological applications can be increased.

The dynamic behavior of micron-sized Permalloy disks with vortex state configuration has been investigated in previous work to increase the efficiency of the magneto-mechanic treatment for the induction of cell

apoptosis[23]. For that purpose, the intensity of a laser beam passing through the aqueous solution of disks was monitored as a function of the alternating magnetic field oriented parallel to the beam. The light transmission was modulated by the disks orientation as a response to the external magnetic field. When the magnetic field was turned on, the plane of the disks was aligned with the field direction and thus the transmitted intensity reached its maximum value. However, when the magnetic field was turned off, the disks gradually randomized their orientation due to the Brownian relaxation and, as a result, the transmission fell to its minimum value.

The modulation of the intensity was therefore governed by the variation of the scattering cross-section in response to the external magnetic field. When the field is on, the light have the minimum scattering cross section as the light encounters only the lateral section of the disks (Figure 6.2. (a)). When the magnetic field is off, the disks can assume an arbitrary orientation leading to a higher scattering cross section (Figure 6.2. (b))[118].

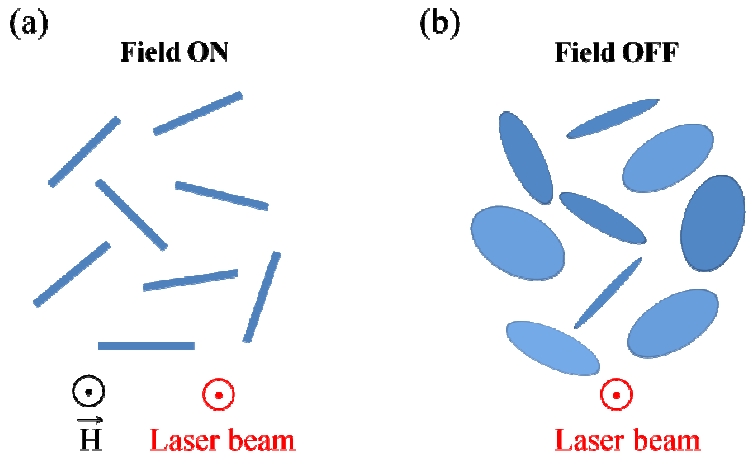

Figure 6.2. Disk-shaped MNS in solution: (a) The magnetic field is turned on and thus the plane of the disks is oriented parallel to the magnetic field direction resulting in a maximum transmission of the light, (b) the field is turned off, the

disks are random leading to a higher scattering cross-section and a lower transmission of the light.

We used this phenomenon to study the dynamic behavior of disk-shaped nanostructures fabricated by IL (and dispersed in solution) as a function of the amplitude and frequency of the alternating magnetic field as well as the duration of the experiment. We also investigated the effect of the disk size and disk material on their response to the applied magnetic field.

6.2. Preparation of the experiment

Inspired by the experiment proposed by Kim et al. for the study of the dynamical behavior of vortex-state microdisks, the experimental arrangement consisted on a laser beam traveling through an aqueous solution of disks. The magnetic field parallel to the laser beam was generated by a coil and the transmitted light was detected by a photodiode (Figure 6.3.).

Before each experiment, the eppendorf containing the suspension of disks was sonicated for 1 minute to ensure a good dispersion of the disks in the aqueous solution.

In order to study the effects of the size and disk material, all the experiments were carried out on three sets of vortex-state disks: Permalloy disks with two different diameters (1200 and 650 nm) and Fe disks of 630 nm in diameter.

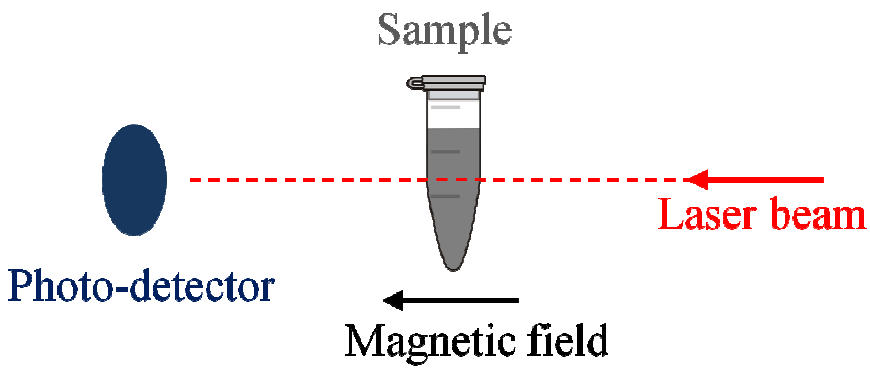

Figure 6.3. Schematics of the experimental set-up to measure the modulation of the light after passing through an eppendorf containing an aqueous solution of vortex-state disks subjected to an alternating magnetic field.

6.3. Dynamic response with the frequency of the magnetic field

The application of a square-wave magnetic field alternating between 0 (field off) and a certain amplitude (field on) resulted in the modulation of the light intensity of a laser beam traveling through an aqueous suspension of vortex-state disks. The experimental light transmission under a magnetic field with amplitude of 160 Oe and frequency f = 1 Hz applied on a suspension of vortex-state disks is shown in figure 6.4. When the field was on, the plane of the disks became parallel to the magnetic field direction and the transmitted intensity increased abruptly to I_{max}. On the other hand, when the field was off, the disks oriented randomly resulting in a minimum transmitted intensity (I_{min}).

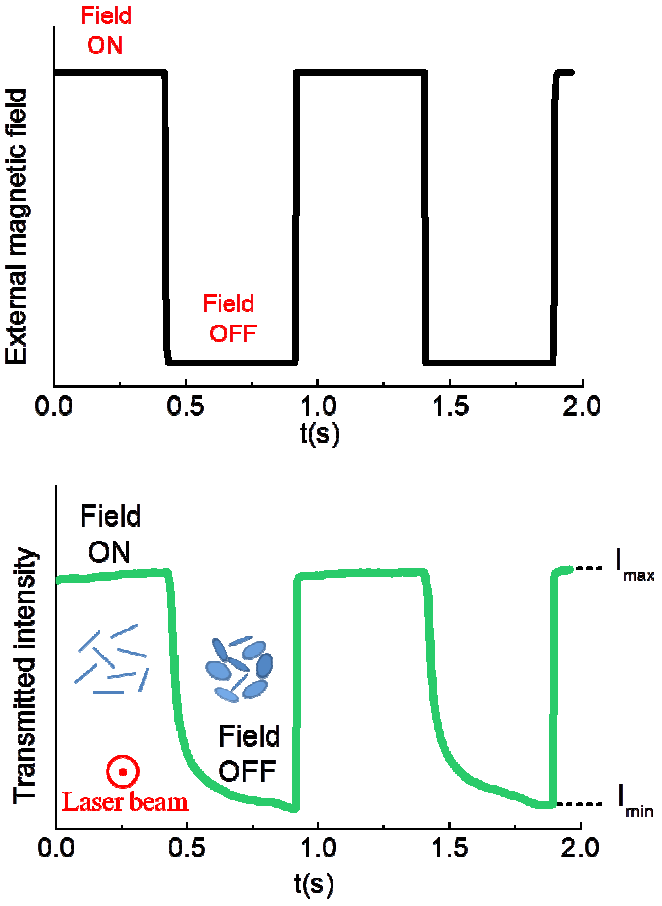

Figure 6.4. Intensity of the transmitted laser beam through an aqueous solution of Fe disks modulated by the application of an alternating magnetic field of 160 Oe of amplitude and 1 Hz of frequency.

The amplitude of the intensity modulation $\Delta I = I_{max} - I_{min}$ was found to be strongly dependent on the frequency of the alternating magnetic field. Figure 6.5. shows the intensity modulation as a function of the frequency normalized to the intensity modulation at low frequency, $\Delta I_f = \Delta I(f) / \Delta I(f_{min})$, for the three sets of vortex-state disks. For all cases, ΔI_f decrease with increasing frequency of the field. This indicates that when the frequency of the external magnetic field increases, the angle of the disk rotation

decreases. We found that the decrease of ΔI_f is mainly due to the increase of the $I_{min,}$ revealing that as the frequency increases, the disks find it more difficult to relax.

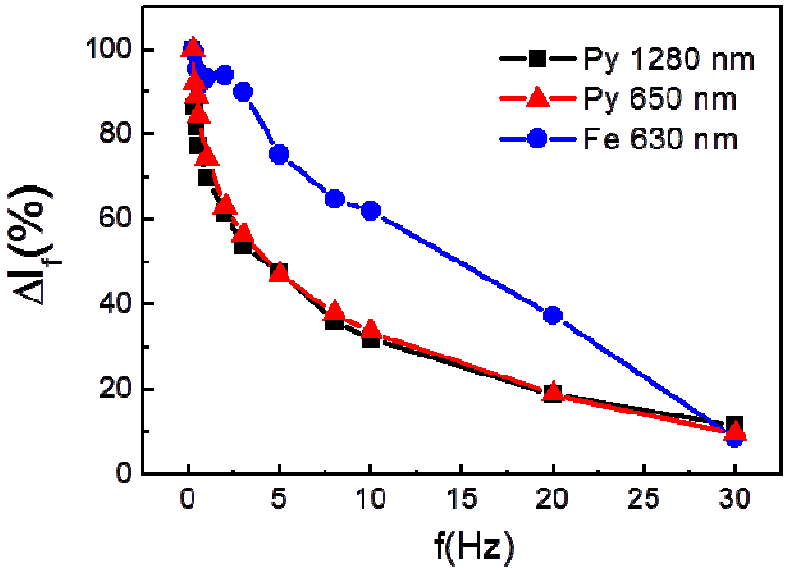

Figure 6.5. Dependence of the light intensity modulation with the frequency of the alternating magnetic field with amplitude 160 Oe, as obtained for Py disks with d = 1200 nm (black squares), Py disks with d = 650 nm (red triangles) and Fe disks with d = 630 nm (blue circles).

As we can observe in figure 6.5, the dependence of ΔI in terms of frequency for Permalloy disks is essentially the same regardless of the disk diameter. A similar tendency has been obtained experimentally[23] and reproduced analytically[119] in previous studies for Permalloy disks of diameter 1μm. However, we found that the dependence of Fe disks differs considerably with respect to that obtained for Permalloy disks. Specifically, for Fe disks, ΔI decrease more slowly at low frequencies (for f < 10 Hz) resulting in higher amplitude of the modulation until 30 Hz.

6.4. Dynamic response with the amplitude of the magnetic field

We carried out a study of the dynamics of the disks when varying the amplitude of the applied magnetic field. For that purpose we designed a experiment consisting on a square-wave magnetic field, which first alternates between 0 and 300 Oe and then, between 0 and a certain amplitude H in the range 5-160 Oe. This particular shape (shown in figure 6.6. (a)) enabled to normalize the obtained ΔI for each H in the range 5-160 Oe to the ΔI obtained at a high enough magnetic field (300 Oe), at which we assume all the disks are perfectly aligned parallel to the applied field, $\Delta I_H = \Delta I(H) / \Delta I(300\ Oe)$. Figure 6.6. (b) shows the response of Fe disks to the square-wave magnetic field for the case of a field of H = 5 Oe. We can observe a reduced intensity modulation ΔI for H = 5 Oe with respect to the intensity modulation at H = 300 Oe.

The dependence of the normalized light modulation as a function of the amplitude of the applied magnetic field is shown in figure 6.7. In all the experiments the frequency of the magnetic field was set to 1 Hz since at this low frequency, the disks were proved to be able to rotate significantly (Figure 6.5.).

The dependence of the dynamic response with H revealed that there is a reduction in the normalized light modulation with decreasing H for the three types of nanostructures, which is more significant at H < 40 Oe.

Figure 6.7. also reveals that in general, quite low amplitude magnetic fields are required to rotate the disks. As we can observe, a field amplitude as low as 40 Oe is sufficient to produce more than the 90% of the maximum intensity modulation for the three types of nanostructures. This result suggests that it is not necessary to saturate the disks to enable disk rotation, since both Py and Fe disks required field amplitudes of hundreds of Oe to

saturate (sections 4.2. and 5.4.) which intuitively would enable faster disk response to the applied magnetic fields.

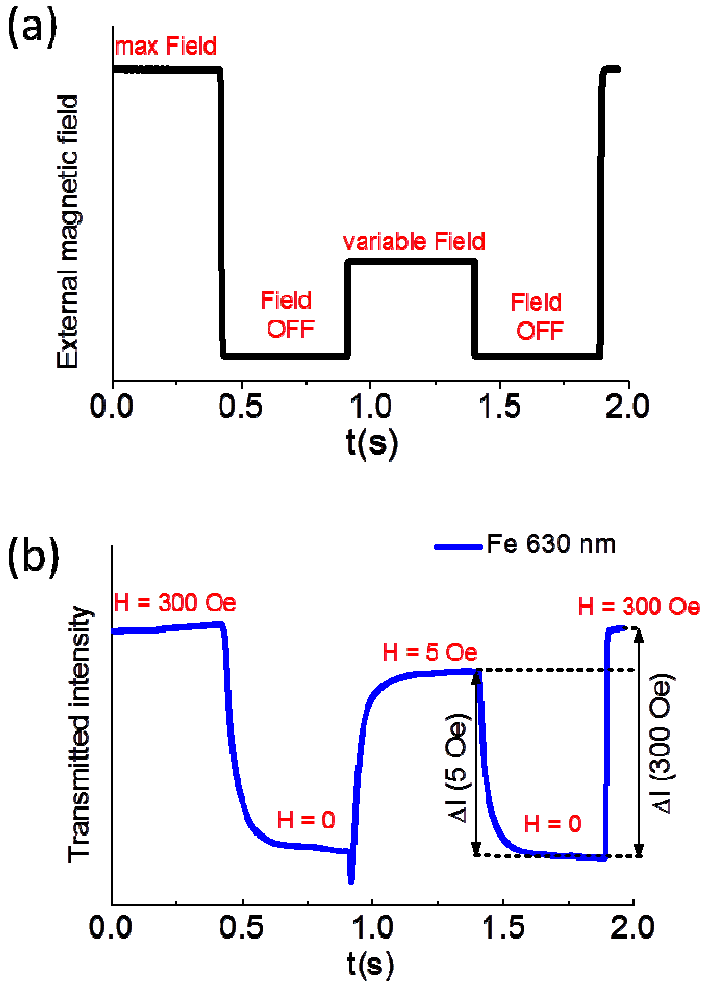

Figure 6.6. (a) Shape of the applied square-wave magnetic field. (b) Intensity transmission through a suspension of Fe disks applying a square-wave field oscillating between 300 Oe and 0, then between 5 Oe and 0.

In order to have a better understanding of the behavior of the disks when changing the amplitude of the field, we compared the shape of the intensity modulation for the different values of H. For that purpose, the intensity of

the transmitted light obtained for the field amplitudes in the range (5 – 160 Oe) was normalized to their corresponding value of ΔI and plotted in figure 6.8. When the field is turned on, the light transmission increases until reaching a certain value (the saturation point) above which the transmitted intensity remains constant. When the field is turned off, the transmitted intensity drops according to the Brownian relaxation of the MNS.

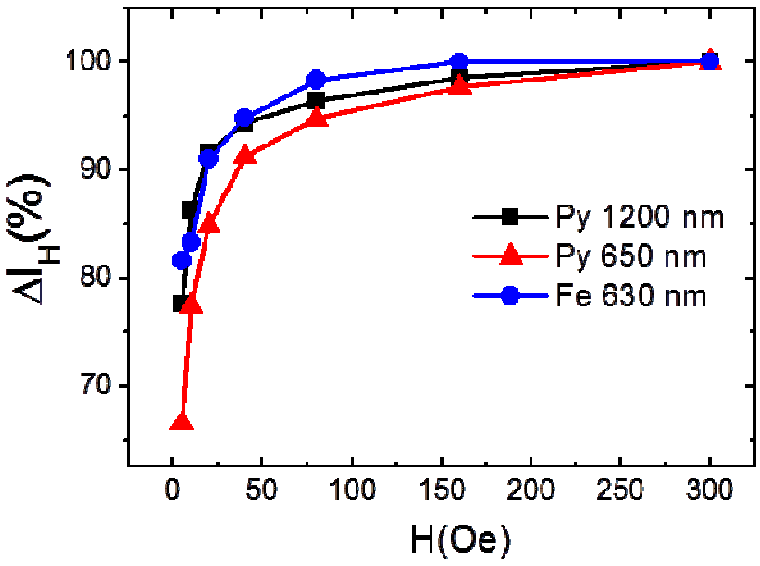

Figure 6.7. Dependence of the light intensity modulation on the amplitude of the applied magnetic field for Py and Fe disks.

The fact that for all amplitudes the transmitted intensity reaches saturation means that during every field pulse the disks in solution completely align with the magnetic field even for amplitude field as low as 5 Oe. However, for such low amplitude the disks align to a different state as revealed in figure 6.6. (b) in which the amplitude of the modulation is shown to decrease for the pulse of amplitude 5 Oe with respect to the pulse of 300 Oe. This reduction in the modulation of the intensity was shown to be quite

significant in the range of amplitudes from 5 to 40 Oe. We believe that the decrease in the light modulation at low amplitudes has to do with the fluctuation of the disks in solution. When a magnetic field is applied, the disks tend to align parallel to the field direction but the liquid fluctuations tend to misalign them. If the field amplitude is very low, (5-40 Oe) the liquid fluctuations have an effect on the orientation of the disks. Actually, the fluctuations increase the average angle of the disks with the field direction, resulting in a higher cross-section and thus, in a lower transmission of the light. For field amplitudes >40 Oe, the magnetic forces are strong enough to keep the disks fixed and not susceptible to the liquid fluctuations, minimizing the cross section and enabling higher light transmission.

We also observed that for field amplitudes > 80 Oe the transmitted intensity increases abruptly reaching saturation almost immediately. However, for lower field amplitudes, the transmitted intensity takes increasing time to reach saturation. This behavior might be due to the fact that for fields of low amplitude, the exerted torque would be lower and the Brownian fluctuations would tend to misalign the disks delaying their orientation. This explanation is also in agreement with the relaxation curves, which can be observed in the right part of the figure (when the field is switched off). For fields of low amplitude, (5 and 10 Oe), the transmitted intensity drops more abruptly due to the fact that the disk were not completely oriented along the field direction so that it takes less time for them to reach a random orientation.

6.5. Dynamic response at low fields

Due to the results obtained from the experiments at fields of low amplitude, a more comprehensive study was carried out to provide insight into the behavior of disk suspensions at low fields.

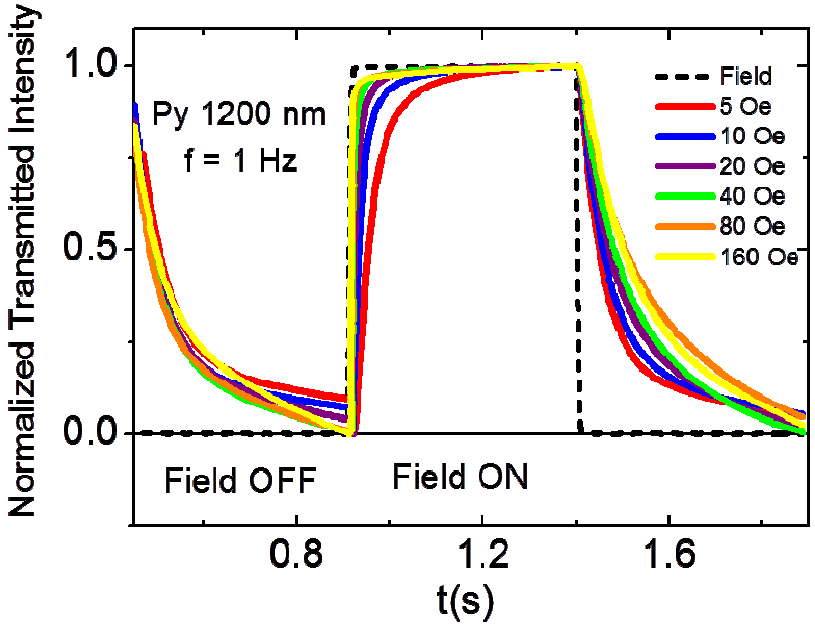

Figure 6.8. Normalized light intensity modulation to analyze the shape of the intensity modulation when alternating magnetic fields of different amplitude are applied.

As discussed in section 6.4, an alignment of the disks when applying field pulses of 500 ms and amplitude as low as 5 Oe occurred since the intensity of the transmitted light saturated during field pulse (Figure 6.6. (b)). However, at low fields the MNSs follow a slow approach to saturation. To investigate this regime, we applied pulses of different duration (between 25 – 100 ms) of the same amplitude and compared it to the pulse of 500 ms in figure 6.9. As we can observe in the figure, the saturation of the transmitted intensity was not achieved for field pulses between 25 and 100 ms indicating that for those short pulses the disks did not have time to align completely parallel to the applied field (Figure 6.9.).

The light intensity transmission for applied fields of low amplitude presents a peculiarity in the precise point in which the field is turned on. In figure 6.6. (b) we can observe a dip just when the intensity starts to increase as a response to a 5 Oe 1applied field. An identical dip was present when applying shorter 5 Oe field pulses as we can observe in figure 6.9. All the dips take place at the same point appearing overlapped in the figure.

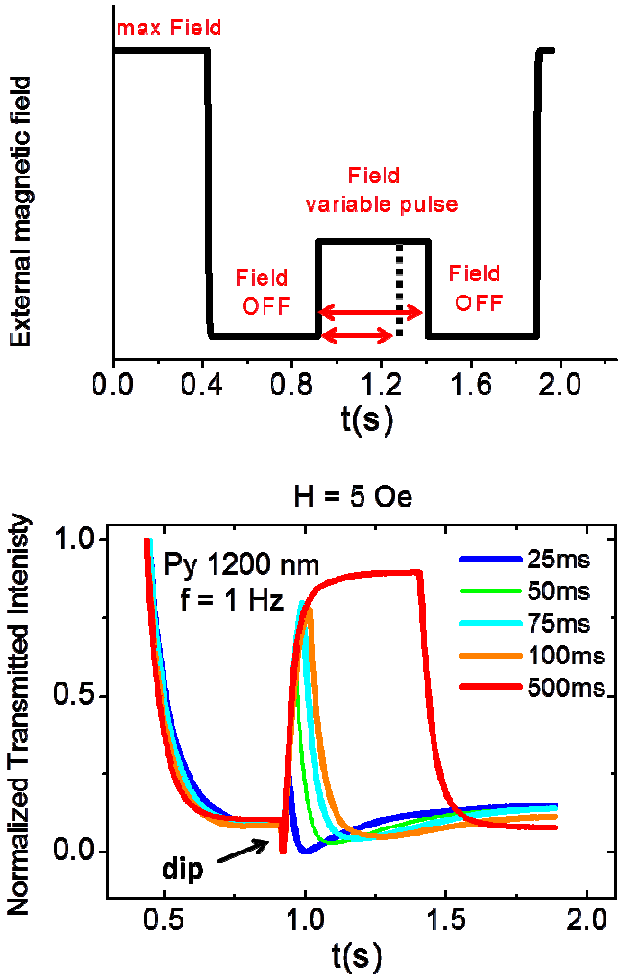

Figure 6.9. Light intensity modulation at field pulses of 5 Oe and different duration.

We found this behavior for both Py and Fe disk-shaped nanostructures. The origin of this dip is likely to be related to the small remanence and coercivity of the nanostructures. Figure 6.10. (a) shows a hysteresis loop of an array of Py disks 650 nm in diameter accompanied by a zoom in the central part of the loop. At zero magnetic field, the remanent magnetization can adopt a positive or a negative value, m(+) or m(-), respectively pointing at opposite directions (Figure 6.10. (b)). In a random distribution of disks in a liquid, at zero external magnetic field, there will coexist disks with a positive and a negative remanent magnetization.

If a positive magnetic field with amplitude 5 Oe is applied, the disks with positive remanence increase the magnetization with a positive projection along the field direction. Therefore, the disks rotate to align the magnetization parallel to the magnetic field through the smallest rotation angle between the magnetization axes and the field direction. During rotation, the cross section of the disks decreases progressively and thus, the transmitted intensity increases (Figure 6.11. (a)). The same magnetic field applied to disks with negative remanence will reduce the magnetization and due to the coercivity, the disks still have a negative projection along the field axis. In this case, the disks rotate to align the magnetization parallel to the field direction through a rotation angle > 90º. Therefore, during the first part of the rotation the disks increase the cross section, even maximizing it at 90º in which the disks plane is perpendicular to the light axis, which decreases the transmitted light. This contribution from the rotation of disks with negative remanence is likely to be the responsible for this abrupt decrease in the transmitted light just after turning on the field. This behavior is no longer present when magnetic fields of higher amplitude are applied. This is due to the fact that fields with higher amplitudes than the coercive field would give rise to positive projection along the field axis of the disk for disks with either positive or negative remanence. Therefore, all the disks would rotate with the same rotation direction through the smallest rotation angle, decreasing the cross section and increasing the transmitted intensity.

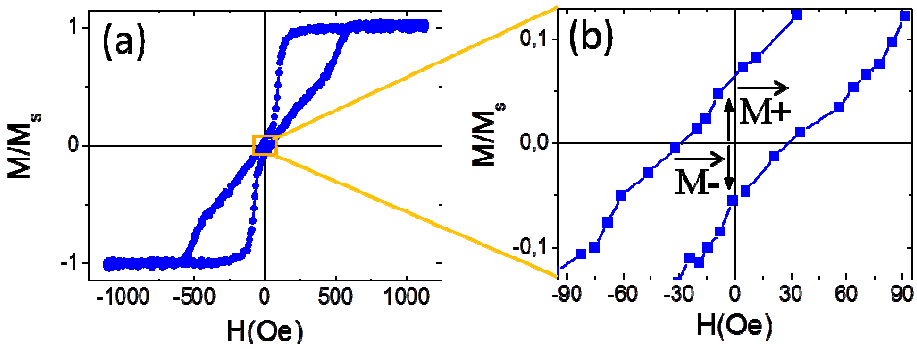

Figure 6.10. (a) Hysteresis loop of disk-shaped Permalloy disks with diameter 650 nm, (b) zoom.

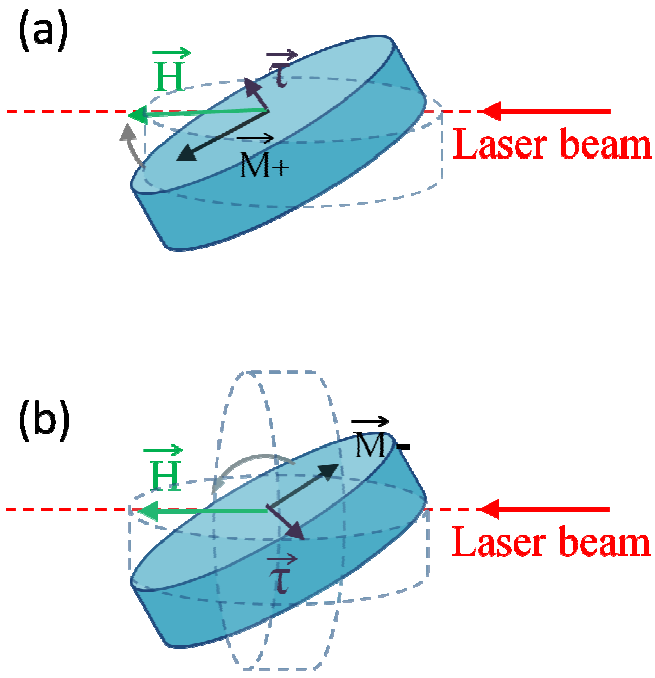

Figure 6.11. Disk rotation when a 5 Oe magnetic field is applied on (a) disks with positive remanence, (b) disks with negative remanence.

6.6. Dynamic response with time

The effects of applying an alternating magnetic field on the disks suspensions over time are discussed in this section. We aimed to study how the disks suspensions respond as a whole when a magnetic field is applied during a quite long period of time and investigate the agglomeration or precipitation effects that can arise during the experiments. To that end, the disks suspensions were dispersed in an ultrasonic bath and then, subjected to an alternating field of 160 Oe with frequency 1 Hz for several minutes. The intensity modulation ΔI was recorded every 30 seconds. In figure 6.12. the intensity modulation as a function of the time of the experiment nomalized by the intensity modulation at time zero, $\Delta I_t = \Delta I(t_{exp}) / \Delta I(0)$, was plotted. The intensity modulation was found to be heavily dependent on time. ΔI_t decreases at increasing time for the three types of disk-shaped nanostructures. This dependence is closely linked to the magnetization that is induced in the disks from the application of an external magnetic field. As we can see in the figure, if a magnetic field is applied for 8 minutes on a Py disk suspension of diameter 1200 nm, ΔI_t (represented by filled black squares) decrease dramatically to the 30%. The same disks were redispersed in an ultrasound bath, then we waited for 8 minutes without applied magnetic field and after those 8 minutes we applied an external field of 160 Oe and frequency 1Hz. The obtained value of ΔI_t (represented by a semifilled black square) did barely reduced from the original value at time zero. This reveals that the configuration of disks suspensions does not change after several minutes unless an alternating magnetic field is present during that time. This also indicates that there is an effect of disks agglomeration only when an external magnetic field is applied due to the dipolar interactions that arise when the disks get magnetized.

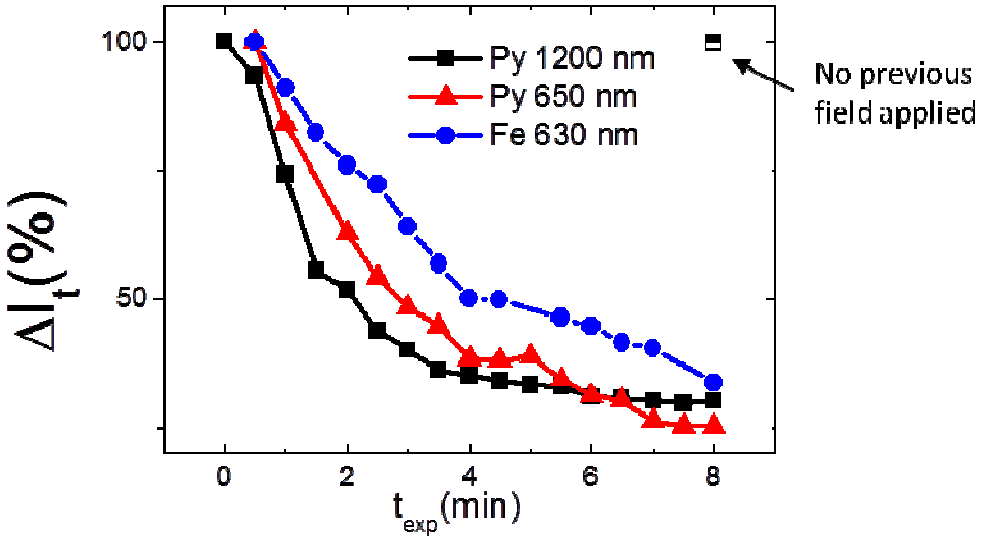

Figure 6.12. Dependence of the intensity modulation with time at an applied field of 160 Oe with frequency 1 Hz, as obtained for Py disks with d = 1200 nm (black squares), Py disks with d = 650 nm (red triangles) and Fe disks with d = 630 nm (blue circles). The semi-filled black square corresponds to the light modulation by an applied field of the same amplitude and frequency after 8 minutes without any applied field.

As we explained before, when the field drops to zero in a square wave magnetic field, the disks gradually adopt a random orientation so the transmitted intensity decreases according to the Brownian relaxation. Figure 6.13. shows the disks relaxation of the disks with no previous applied magnetic field, which corresponds to t_{exp} = 0 in figure 6.12, and the relaxation when the alternating field has been on for 1 minute (t_{exp} = 1 min in figure 6.12.). The transmitted intensity evolution through the disks suspension (blue line) was fitted by an exponential decay with the form $I(t) = const \times \exp(1/\tau)\, t$ (dashed red line), where τ is a time constant, revealing a higher τ when increasing the time that the field has been on (t_{exp}). This indicates that the disks relaxation occurs more slowly at

increasing t_{exp}. The hydrodynamic volume and the viscosity are expected to increase the time constant[120]. Since the viscosity of the medium did not change, the higher time constant might be explained by an increase of the hydrodynamic volume of the nanostructures related to the formation of disk chains as t_{exp} increases[121]. The disk chain formation occurs as time goes by due to the magnetization that is induced on the vortex-state disks when an external magnetic field is applied[122]. This agglomeration effect might also be the responsible for the reduction of the intensity modulation with time shown in figure 6.12, as the cross section of the nanostructures would substantially change.

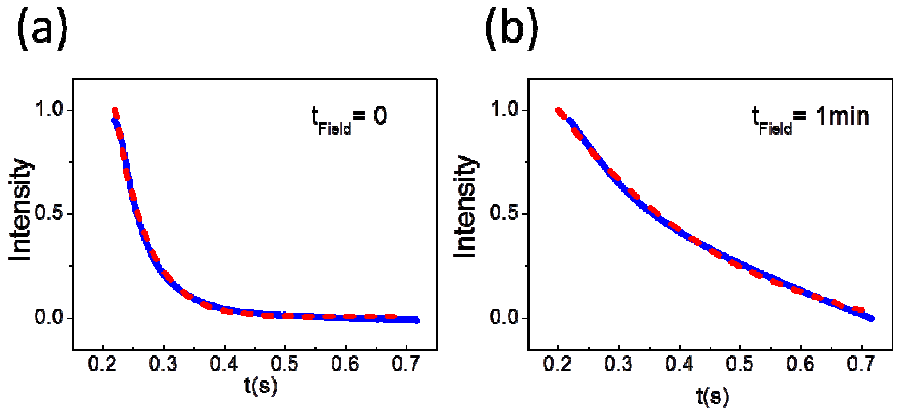

Figure 6.13. The transmitted intensity decay when the field is switched off for disks with diameter 1200 nm (blue line) and exponential fitting (dashed red line). (a) the alternating magnetic field has just turned on (t_{exp} = 0), (b) the alternating field has been on for one minute (t_{esp} = 1 min).

6.7. Conclusions

We experimentally studied the dynamic behavior of the disks suspensions when subjected to an external alternating magnetic field. To that end, we measured the modulation of the light across disks suspensions, which arises from the variation of the scattering cross-section due to the disks orientation/relaxation when an alternating field is applied along the incident beam direction. The effects of the variation of experimental parameters (i.e. the frequency and the amplitude of the magnetic field) on the dynamic response of the disks were investigated for disks of different materials and different sizes to be able to enhance the efficiency of the magneto-mechanic actuation and also provide insights into the limitations of the technique.

The dynamic response of the disks as a function of the frequency of the external magnetic field revealed that the amplitude of the rotation of the disks drastically decreases with increasing the frequency. In addition to this, Fe disks showed a smoother decrease in the light modulation at low frequencies, for $f < 10$ Hz, resulting in higher amplitude of the modulation until 30 Hz with respect to Py disks.

The dependence of the dynamic behavior of the disks with the amplitude of the magnetic field revealed that field amplitudes as low as 40 Oe are sufficient to lead to more than the 90% of the maximum intensity modulation for the three types of nanostructures, indicating that such low fields are sufficient to rotate the disks.

The intensity modulation was found to be strongly dependent on time. Through the study of variation of Brownian relaxation of the disks, we attributed this dependence to the formation of disk chains as the time interval, in which the magnetic field is applied, increases.

References

[1] D.-H. Kim, E. A. Rozhkova, I. V Ulasov, S. D. Bader, T. Rajh, M. S. Lesniak, and V. Novosad, "Biofunctionalized magnetic-vortex microdiscs for targeted cancer-cell destruction," *Nat. Mater.*, vol. 9, no. 2, pp. 165–171, 2010.

[2] S. Leulmi, X. Chauchet, M. Morcrette, G. Ortiz, H. Joisten, P. Sabon, T. Livache, Y. Hou, M. Carrière, and S. Lequien, "Triggering the apoptosis of targeted human renal cancer cells by the vibration of anisotropic magnetic particles attached to the cell membrane," *Nanoscale*, vol. 7, no. 38, pp. 15904–15914, 2015.

[3] E. A. Vitol, V. Novosad, and E. A. Rozhkova, "Multifunctional ferromagnetic disks for modulating cell function," *IEEE Trans. Magn.*, vol. 48, no. 11, pp. 3269–3274, 2012.

[4] B. D. Hoffman, C. Grashoff, and M. A. Schwartz, "Dynamic molecular processes mediate cellular mechanotransduction," *Nature*, vol. 475, no. 7356, pp. 316–323, 2011.

[5] E. A. Vitol, V. G. Yefremenko, S. Jain, J. Pearson, E. A. Rozhkova, S. D. Bader, and V. Novosad, "Optical transmission modulation by disk-shaped ferromagnetic particles," *J. Appl. Phys.*, vol. 111, no. 7, p. 07A945, 2012.

[6] N. Bazazzadeh, S. M. Mohseni, A. Khavasi, M. I. Zibaii, S. M. S. Movahed, and G. R. Jafari, "Dynamics of magnetic nano-flake vortices in Newtonian fluids," *J. Magn. Magn. Mater.*, vol. 419, pp. 547–552, 2016.

[7] T. Klein, A. Laptev, A. Günther, P. Bender, A. Tschöpe, and R. Birringer, "Magnetic-field-dependent optical transmission of nickel nanorod colloidal dispersions," *J. Appl. Phys.*, vol. 106, no. 11, p. 114301, 2009.

[8] R. Kötitz, W. Weitschies, L. Trahms, W. Brewer, and W. Semmler,

"Determination of the binding reaction between avidin and biotin by relaxation measurements of magnetic nanoparticles," *J. Magn. Magn. Mater.*, vol. 194, no. 1, pp. 62–68, 1999.

[9] J. E. Martin, K. M. Hill, and C. P. Tigges, "Magnetic-field-induced optical transmittance in colloidal suspensions," *Phys. Rev. E*, vol. 59, no. 5, p. 5676, 1999.

Chapter 7

In-vitro experiments with cancer cells

7.1. Introduction

Cancer is a major public health problem worldwide. The challenges that medical research against cancer is facing these days includes the early detection of the tumor and the improvement not only of the therapeutic outcome, but also of the methods of treatment, which often have undesirable side effects. As the conventional chemotherapy agents are distributed nonspecifically in the body affecting both cancer and healthy cells, they often cause considerable adverse reactions such as nausea, hair loss, and compromised immune system.

Magnetic nanoparticles have the potential to overcome the limitations in cancer treatment associated to the nonspecific systemic distribution of conventional chemotherapy agents and the inadequate drug concentration

reaching the tumor[123]. This is possible thanks among other reasons[124], to the ability to utilize external guidance by magnetic fields[125] and/or targeting strategies using ligands or antibodies directed to selected receptors in cancer cells[126], [127]. In this sense, magnetic nanoparticles offer attractive opportunities for directing the treatment specifically to a targeted tumor, for example by delivering a chemotherapy drug at the tumor site[125], [128], [129]. In addition to this, magnetic nanoparticles can act themselves as treatment agents since they can transform the energy of external alternating magnetic fields into local heating, which can be used to destroy cancer cells or to make them more susceptible to the chemotherapy agents –magnetic hyperthermia-[130]–[132].

Magnetic hyperthermia has been widely studied showing remarkable achievements as a promising cancer therapy. This technique uses superparamagnetic nanoparticles embedded on tumor tissue providing local heating (over 43^{o}C)[133] to destroy the tumor cells by the application of alternating magnetic fields with high frequencies of hundreds of kHz. Despite the promising achievements in cancer therapy, there are several challenges that need to be addressed before magnetic hyperthermia becomes a standard medical procedure[11]. One of the most important tasks is to improve the heating efficiency, which depends on the nanoparticle magnetic properties and the amplitude and frequency of the alternating magnetic fields. Since the superparamagnetic nanoparticles are typically iron oxides they have low magnetic moments, which limit their heating efficiency, and thus a great amount of nanoparticles are needed per therapy cycle. Regarding the external fields, the generation of strong alternating magnetic fields of high frequencies required for the magnetic hyperthermia represents a real technical challenge.

Due to their unique properties such as high magnetic moments and anisotropic shape, the magnetic structures obtained by lithographic methods (MNS) made it possible the development of alternative techniques for targeted cancer therapy[23], [134], [39]. In particular, the use of vortex-

state microdisks fabricated by photolithography was investigated for cancer cell destruction *in-vitro* assays[23]. Under the application of alternating magnetic fields, the vortex state disks oscillate transferring a mechanical stimulus to the cell membranes. Unprecedentedly weak magnetic fields of amplitude < 100 Oe and frequencies of ten's of Hertz were sufficient to trigger cancer cell apoptosis. This contrasts with the magnetic fields of frequencies of hundreds of KHz used for heating-induced cancer cell death with superparamagnetic nanoparticles in magnetic hyperthermia. Therefore, the required external power (proportional to $H \times f^2$) for magneto-mechanic cancer cell destruction using microdisks was reduced to approximately 10^6 times with respect to the hyperthermia treatments using superparamagnetic nanoparticles, opening up new low cost treatment opportunities with minimal invasiveness. Although this study held great promise for the translation of the magnetic targeting to clinical applications, two main issues were claimed to be addressed[24]. Firstly, the limitation of photolithography in the element size in the micrometer range, being crucial for clinical applications to scale down into the submicrometer scale. Secondly, the need of developing more biocompatible disks not containing Nickel. In order to address these challenges, in this thesis we developed a technique to fabricate disks in the submicrometer range and very importantly, we succeeded in fabricating disks of a more biocompatible material and higher magnetic moment: Fe, while preserving the vortex state configuration.

In this chapter, the viability of submicrometric disks of Permalloy (NiFe) and also of pure Fe with vortex-state configuration was assessed in primary melanoma cultures. All disks used in this study had been coated by Ti in the fabrication strategy to prevent from oxidation. We studied the citotoxicity effects at different disk sizes and compositions (Py vs Fe). This part of the thesis was performed in collaboration with Dr. María Dolores Boyano and Arantza Pérez from the Department of Cell Biology and Histology of the University of the Basque Country UPV/EHU.

7.2. Cell lines and culture conditions

Prior to the incubation with cells, MNS were sonicated for one minute and cleaned with sterile phosphate buffered saline (PBS), which is an aqueous and saline solution with osmolarity and ion concentration similar to the extracellular liquid of mammals. The cleaning process was repeated three times, and afterwards the MNS were sterilized in an autoclave (Matachana Serie 500) at 120 ºC for 1 h 30 min.

The A375 (CRL-1619) primary melanoma cell line was obtained from ATCC (American Type Culture Collection). They were routinely cultured as monolayers in 25 cm^2 flasks with the cell culture medium DMEM (Dulbecco´s Modified Eagle´s Medium, supplemented with 10% (v/v) heat-inactivated serum-supplement FBS (Fetal Bovine Serum), 2 mM L-Glutamine and antibiotics (100 µg/ml Streptomycin and 100 IU/ml Penicillin). All the experiments were carried out at ≥90% viability and the cells were cultured in an 80-90% of confluence.

L-Glutamine and PBS were obtained from MERCK Chemicals and Life Science S.A. DMEM and the Penicillin/Streptomycin antibiotic solutions were purchased from Thermo Fisher Scientific Inc. Fetal Bovine Serum (FBS) was acquired from GE Healthcare.

7.3. Cell viability

A375 cells were seeded in culture medium in flat bottom 96 well plates at the density of 10,000 cells per well. After allowing the cells to attach to the wells overnight, they were incubated with different concentrations of MNS.

XTT colorimetric assay was used to determine cell viability according to the manufacturer´s instructions. We used the XTT Cell Proliferation Kit II from

MERCK Chemicals. This assay is based on the cleavage of the tetrazolium salt XTT in the presence of an electron-coupling reagent, producing a soluble formazan salt. This conversion only occurs in viable cells. Cells grown in a 96-well tissue culture plate are incubated with the XTT labeling mixture for 2 - 20 hours. After this incubation period, the formazan dye formed is quantified using a scanning multi-well spectrophotometer. The measured absorbance directly correlates to the number of variable cells. Viability assays are of particular importance for routine applications in cell biology. XTT salts are particularly useful for this type of analysis. Tetrazolium salts are cleaved to formazan by the succinate-tetrazolium reductase system which belongs to the respiratory chain of the mitochondria, and is only active in metabolically intact cells.

After incubation, the absorbance was measured at 490 nm in a microplate reader (SynergyTM HT, BioTek). Untreated controls were also included and several replicate wells, as described later, were analyzed for each condition. The cell viability percentage was calculated relative to controls: experimental absorbance / untreated control absorbance x100.

7.4. Results: Citotoxicity

7.4.1. Size dependence study

The toxicity of Permalloy nanodisks of two different sizes: 650 nm in diameter (referred as nanodisks) and 1280 nm in diameter (referred as microdisks) and 50 nm in thickness, protected on both sides by a thin Ti layer, was assessed in primary melanoma cultures. A375 skin cancer cells were incubated for 24 hours with the disks. XTT assays were evaluated for different disk concentrations: 0 - 40 microdisks per cell and 0 – 140 nanodisks per cell. The maximum concentration of nanodisks (140 nanodisks/cell) was calculated to yield the same total volume of magnetic

material than the maximum concentration of microdisks (40 microdisks/cell). Five replicate wells were analyzed for each condition. The cell viability percentage relative to the controls (0 disks per cell) is shown in Figure 7.1. As we can observe, the viability of melanoma cells after 24 h was not altered by the introduction of disks, being close to the 100 % with independence of the disk concentration. Therefore, the Py disks that we developed with two different sizes: 650 and 1280 nm in diameter and 50 nm in thickness do not generate citotoxicity after 24 h.

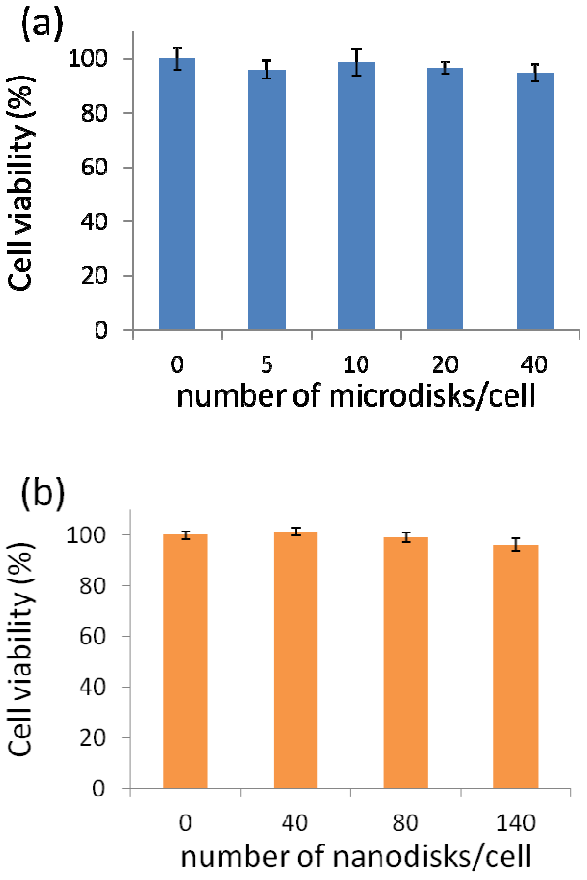

Figure 7.1. Viable cells percentage after 24 hours of incubation of different concentrations of the two sets of disks: (a) 0-40 microdisks/cell, (b) 0-140 nanodisks/cell with A375 cells. Data are present as Mean ± SD (standard deviation).

7.4.2. Material dependence study

A citotoxicity study was carried out by using vortex state nanodisks of two different materials: Py and pure Fe (in both cases coated by Ti), and the same size: 650 nm in diameter and 50 nm in thickness. A375 skin cancer cells were incubated for 48 hours with the two types of nanodisks. After incubation, XTT calorimetric assays were evaluated for different nanodisks concentrations: 0, 50, 100, 200 nanodisks per cell either for Py or Fe nanodisks. In this case, three replicate wells were used for each condition. Figure 7.2. shows the cell viability for the Fe and Py nanodisks after 48 h of incubation. No significant decrease in the viable cells percentage was obtained for the Py and Fe disks in the range of concentrations used in this study. This indicates that, in principle, neither the Py nor the Fe nanodisks that we developed present citotoxicity in these conditions.

7.4.3. Time-lapse experiment

Time - lapse microscopy consists essentially of capturing images of dynamic events at predetermined regular time intervals and then viewing them at a greater speed to give an accelerated view of the microscopic process. One of the applications of this technique is live cell imaging[135].

We used this time-lapse microscopy to observe how the melanoma cells behave in presence of the magnetic nanodisks. For that purpose we used the BioStation IMQ live cell time-lapse microscopy (Nikon Instruments B.V.), which offers a good controlled and monitored incubator/imaging environment to reduce disturbance to cells and preserve cell health.

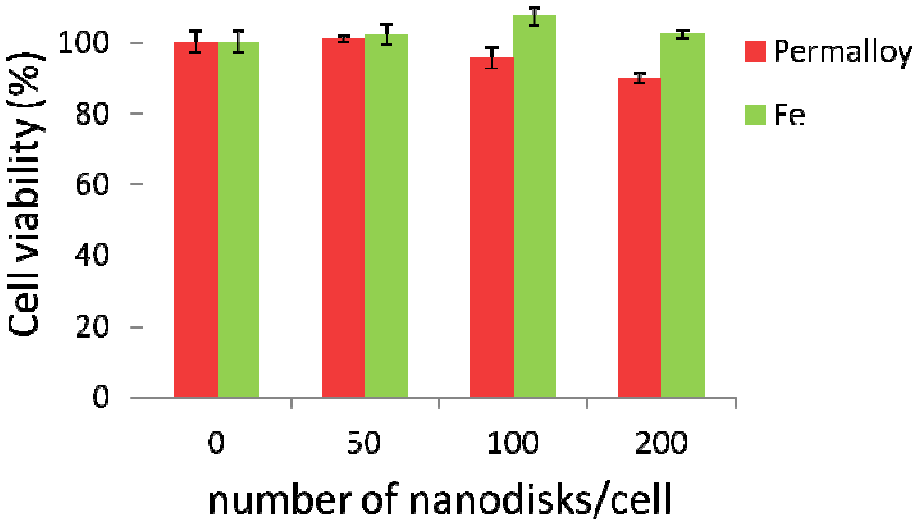

Figure 7.2. Viable A375 cells percentage after 48 hours of incubation with different concentrations of Py disks (red bars) and Fe disks (green bars): 0, 50, 100, 200 nanodisks/cell. Data are present as Mean ± SD (standard deviation).

For the experiment 200,000 A375 cells were seeded in culture medium in a 35 mm glass bottom dish and allowed to attach overnight. Cells were incubated with 140 nanodisks per cell. We used Permalloy nanodisks of 650 nm in diameter and 50 nm in thickness.

This culture was recorded by taking photos at a 20X magnification every 10 minutes during 24 h with the BioStation IMQ. Figure 7.3. displays two images at (a) 0 h and (c) 24 h for an initial concentration of 140 MNS/cell. Figure 7.3. (b) shows the zoom of figure 7.3. (a) making it possible to distinguish the presence of dispersed disks over the space between the cells. Optical microscope images taken every 10 min for 24 hours provide evidence that cells introduce the nanostructures present in the culture medium without suffering any negative effects; the cancer cells continue to replicate and move normally.

In the light of the citotoxicity and time-lapse results we conclude that the nanodisks are innocuous when no magnetic field is applied, which turns them into excellent candidates for studying new therapeutic options for cancer treatment.

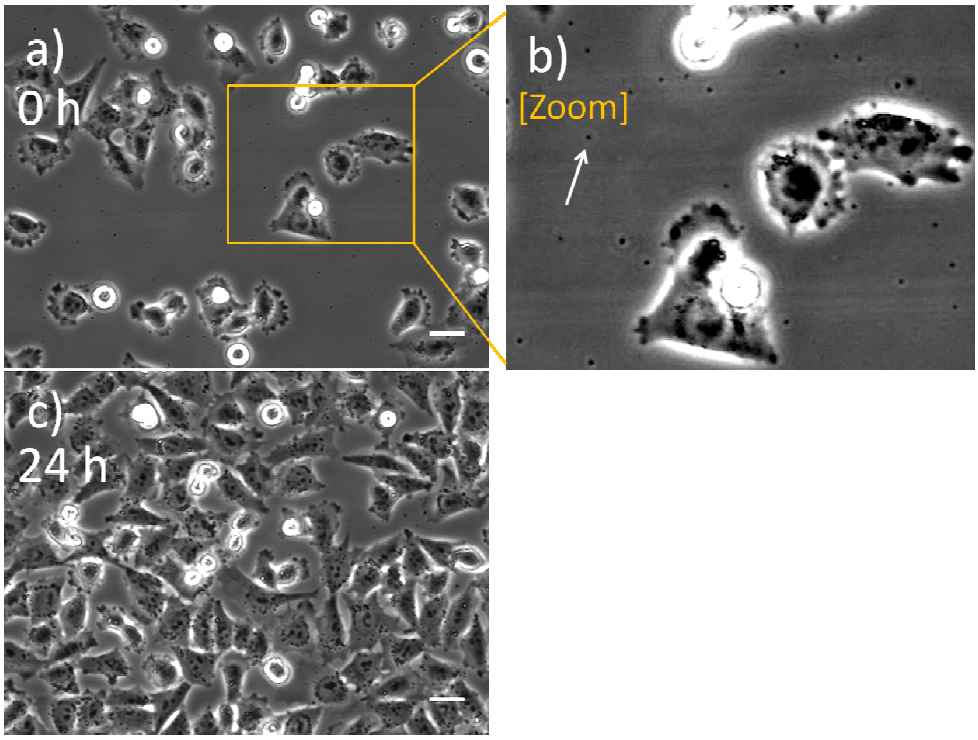

Figure 7.3. Evolution of the cell culture of A375 cells and MNS (140 MNS/Cell) over time: (a) 0 h, (b) zoom of (a) and (c) 24 h. Images were taken every 10 minutes for up to 24 hours. The scale bar is 30 μm.

7.5. Conclusions

The viability of magnetic submicrometric disks was assessed on primary melanoma cell cultures for different disk sizes and composition (Py and Fe).

The cytotoxicity assays revealed that the viability of melanoma cells after 24 h was not altered by the introduction of Py disks coated by Ti layers with independence of the disk concentration for the different disk sizes.

The comparative cytotoxicity study carried out on disks of different materials (Py and Fe) showed absence of toxicity after 48 h of incubation with melanoma cells for both magnetic materials.

The time elapse experiment provided evidence that the melanoma cells introduce the nanostructures with no visible signs of alteration of either cell replication or movement.

In the light of the citotoxicity and time-lapse results we conclude that the nanodisks are innocuous when no magnetic field is applied, which turns them into excellent candidates for studying new therapeutic options for cancer treatment.

References

[1] S. Dürr, C. Janko, S. Lyer, P. Tripal, M. Schwarz, J. Zaloga, R. Tietze, and C. Alexiou, "Magnetic nanoparticles for cancer therapy," *Nanotechnol. Rev.*, vol. 2, no. 4, pp. 395–409, 2013.

[2] J. H. Grossman and S. E. McNeil, "Nanotechnology in cancer medicine," *Phys. Today*, vol. 65, no. 8, p. 38, 2012.

[3] M. K. Yu, Y. Y. Jeong, J. Park, S. Park, J. W. Kim, J. J. Min, K. Kim, and S. Jon, "Drug-loaded superparamagnetic iron oxide nanoparticles for combined cancer imaging and therapy in vivo," *Angew. Chemie*, vol. 120, no. 29, pp. 5442–5445, 2008.

[4] C. C. Berry and A. S. G. Curtis, "Functionalisation of magnetic nanoparticles for applications in biomedicine," *J. Phys. D. Appl. Phys.*, vol. 36, no. 13, p. R198, 2003.

[5] M. Arruebo, R. Fernández-Pacheco, B. Velasco, C. Marquina, J. Arbiol, S. Irusta, M. R. Ibarra, and J. Santamaria, "Antibody-Functionalized Hybrid Superparamagnetic Nanoparticles," *Adv. Funct. Mater.*, vol. 17, no. 9, pp. 1473–1479, 2007.

[6] C. Sun, J. S. H. Lee, and M. Zhang, "Magnetic nanoparticles in MR imaging and drug delivery," *Adv. Drug Deliv. Rev.*, vol. 60, no. 11, pp. 1252–1265, 2008.

[7] T. Neuberger, B. Schöpf, H. Hofmann, M. Hofmann, and B. Von Rechenberg, "Superparamagnetic nanoparticles for biomedical applications: possibilities and limitations of a new drug delivery system," *J. Magn. Magn. Mater.*, vol. 293, no. 1, pp. 483–496, 2005.

[8] A. Jordan, R. Scholz, P. Wust, H. Fähling, and R. Felix, "Magnetic fluid hyperthermia (MFH): Cancer treatment with AC magnetic field induced excitation of biocompatible superparamagnetic nanoparticles," *J. Magn. Magn. Mater.*, vol. 201, no. 1, pp. 413–419, 1999.

[9] S. Laurent, S. Dutz, U. O. Häfeli, and M. Mahmoudi, "Magnetic fluid hyperthermia: focus on superparamagnetic iron oxide nanoparticles," *Adv. Colloid Interface Sci.*, vol. 166, no. 1, pp. 8–23, 2011.

[10] E. A. Perigo, G. Hemery, O. Sandre, D. Ortega, E. Garaio, F. Plazaola, and F. J. Teran, "Fundamentals and advances in magnetic hyperthermia," *Appl. Phys. Rev.*, vol. 2, no. 4, p. 41302, 2015.

[11] T. Kobayashi, "Cancer hyperthermia using magnetic nanoparticles," *Biotechnol. J.*, vol. 6, no. 11, pp. 1342–1347, 2011.

[12] S. Dutz and R. Hergt, "Magnetic particle hyperthermia—a promising tumour therapy?," *Nanotechnology*, vol. 25, no. 45, p. 452001, 2014.

[13] D.-H. Kim, E. A. Rozhkova, I. V Ulasov, S. D. Bader, T. Rajh, M. S. Lesniak, and V. Novosad, "Biofunctionalized magnetic-vortex microdiscs for targeted cancer-cell destruction," *Nat. Mater.*, vol. 9, no. 2, pp. 165–171, 2010.

[14] E. A. Rozhkova, V. Novosad, D.-H. Kim, J. Pearson, R. Divan, T. Rajh, and S. D. Bader, "Ferromagnetic microdisks as carriers for biomedical applications," *J. Appl. Phys.*, vol. 105, no. 7, p. 07B306, 2009.

[15] E. A. Vitol, V. Novosad, and E. A. Rozhkova, "Multifunctional ferromagnetic disks for modulating cell function," *IEEE Trans. Magn.*, vol. 48, no. 11, pp. 3269–3274, 2012.

[16] J. Dobson, "A twist on tumour targeting," *Nat Mater*, vol. 9, pp. 95–96, 2010.

[17] R. Andrade, L. Crisol, R. Prado, M. D. Boyano, J. Arluzea, and J. Aréchaga, "Plasma membrane and nuclear envelope integrity during the blebbing stage of apoptosis: a time-lapse study," *Biol. Cell*, vol. 102, no. 1, pp. 25–35, 2010.